

HARVARD UNIVERSITY
Graduate School of Arts and Sciences



DISSTERTATION ACCEPTANCE CERTIFICATE

The undersigned, appointed by the
Committee on Higher Degrees in Biophysics
have examined a dissertation entitled

**Coordination of individual and ensemble cytoskeletal
motors studied using tools from DNA nanotechnology**

presented by **Nathan Dickson Derr**

candidate for the degree of Doctor of Philosophy and hereby
certify that it is worthy of acceptance.

Signature Handwritten signature of Nathan Dickson Derr.

Typed name: Prof. Andres E. Leschziner

Signature Handwritten signature of Prof. Andres E. Leschziner.

Typed name: Prof. Jagesh V. Shah

Signature Handwritten signature of Prof. Jagesh V. Shah.

Typed name: Prof. Peng Yin

Signature Handwritten signature of Prof. Peng Yin.

Typed name: Prof. James M. Hogle

Signature Handwritten signature of Prof. James M. Hogle.

Date: April 29, 2013

**Coordination of individual and ensemble cytoskeletal motors
studied using tools from DNA nanotechnology**

A dissertation presented
by

Nathan Dickson Derr

to

The Committee on Higher Degrees in Biophysics

in partial fulfillment of the requirements
for the degree of

Doctor of Philosophy

in the subject of

Biophysics

Harvard University
Cambridge, Massachusetts

April 2013

UMI Number: 3566860

All rights reserved

INFORMATION TO ALL USERS

The quality of this reproduction is dependent upon the quality of the copy submitted.

In the unlikely event that the author did not send a complete manuscript and there are missing pages, these will be noted. Also, if material had to be removed, a note will indicate the deletion.



UMI 3566860

Published by ProQuest LLC (2013). Copyright in the Dissertation held by the Author.

Microform Edition © ProQuest LLC.

All rights reserved. This work is protected against unauthorized copying under Title 17, United States Code



ProQuest LLC.
789 East Eisenhower Parkway
P.O. Box 1346
Ann Arbor, MI 48106 - 1346

© 2013 by Nathan Dickson Derr

Coordination of individual and ensemble cytoskeletal motors studied using tools from DNA nanotechnology

Abstract

The cytoskeletal molecular motors kinesin-1 and cytoplasmic dynein drive many diverse functions within eukaryotic cells. They are responsible for numerous spatially and temporally dependent intracellular processes crucial for cellular activity, including cytokinesis, maintenance of sub-cellular organization and the transport of myriad cargos along microtubule tracks. Cytoplasmic dynein and kinesin-1 are processive, but opposite polarity, homodimeric motors; they each can take hundreds of thousands of consecutive steps, but do so in opposite directions along their microtubule tracks. These steps are fueled by the binding and hydrolysis of ATP within the homodimer's two identical protomers. Individual motors achieve their processivity by maintaining asynchrony between the stepping cycles of each protomer, insuring that at least one protomer always maintains contact with the track.

How dynein coordinates the asynchronous stepping activity of its protomers is unknown.

We developed a versatile method for assembling *Saccharomyces cerevisiae* dynein heterodimers, using complementary DNA oligonucleotides covalently linked to dynein monomers labeled with different organic fluorophores. Using two-color, single-molecule microscopy and high-precision, two-dimensional tracking, we found that dynein has a highly variable stepping pattern that is distinct from all other processive cytoskeletal motors, which use "hand-over-hand" mechanisms. Uniquely, dynein stepping is stochastic when its two motor domains are close together. However,

coordination emerges as the distance between motor domains increases, implying that a tension-based mechanism governs these steps.

Many cellular cargos demonstrate bidirectional movement due to the presence of ensembles of both cytoplasmic dynein and kinesin-1. To investigate the mechanisms that coordinate the interactions between motors within an ensemble, we constructed programmable synthetic cargos using three-dimensional DNA origami. This system enables varying numbers of DNA oligonucleotide-linked motors to be attached to the synthetic cargo, allowing for control of motor type, number, spacing, and orientation *in vitro*. In ensembles of one to seven identical-polarity motors, we found that motor number had minimal effect on directional velocity, whereas ensembles of opposite-polarity motors engaged in a tug-of-war resolvable by disengaging one motor species.

Table of Contents

Title Page	i
Copyright notice	ii
Abstract	iii
Table of Contents	v
List of Figures	vii
List of Tables	ix
Acknowledgments	x
Chapter 1: Introduction	1
Introduction to cytoskeletal molecular motors	2
How does dynein move processively?	11
How do motors within an ensemble coordinate their interactions to collectively haul cargo?	15
References	19
Chapter 2: Dynein achieves processive motion through both stochastic and coordinated stepping	23
Contributions	24
Abstract	25
Results	26
Methods	46
Acknowledgments	56
References	57
Chapter 3: Tug of war in motor protein ensembles revealed with a programmable DNA origami scaffold	61
Contributions	62
Abstract	63

Results	64
Methods	73
Acknowledgments	82
References	83
Chapter 4: Conclusions	86
Concluding remarks	87
References	92
Appendix 1: Supplementary Figures and Tables for: Dynein achieves processive motion through both stochastic and coordinated stepping	95
Contributions	96
References	107
Appendix 2: Supplementary Figures and Tables for: Tug of war in motor protein ensembles revealed with a programmable DNA origami scaffold	108
Contributions	109
Scaffold sequence	132
References	136

List of Figures

Figure 1.1	Schematic of a eukaryotic cell and its cytoskeletal filaments	2
Figure 1.2	Cytoskeletal motors and their tracks	3
Figure 1.3	Simulated position vs. time traces for motor stepping models	5
Figure 1.4	Examples of microtubule-based motor ensembles	8
Figure 1.5	Structure and domain architecture of the dynein motor	10
Figure 1.6	Methods of observing of dynein motility	12
Figure 1.7	Schematic diagram of DNA origami based synthetic cargo	17
Figure 2.1	Dynein structure and constructs used in this study	27
Figure 2.2	Two-dimensional stepping analysis of GST-dynein homodimers	31
Figure 2.3	DNA-based dynein heterodimers are functional and step similarly to protein-based dynein homodimers	34
Figure 2.4	Two-color tracking of dynein stepping	36
Figure 2.5	Spatial arrangement of dynein motor domains during the two- head-bound state	39
Figure 2.6	Dynein steps are stochastic at short head-to-head spacing and coordinated as head-to-head spacing increases	42
Figure 3.1	Design and validation of a three-dimensional DNA origami synthetic cargo	65
Figure 3.2	Single-molecule motile properties of chassis-motor complexes	67
Figure 3.3	Chassis attached to dynein and kinesin frequently engage in a stalled tug of war	69
Figure 3.4	Disengagement of one motor species resolves stalled tug of war	71
Figure 4.1	Synthetic motor assemblies for biophysics and nanoscale molecular shuttles	90
Figure A1.1	Single molecule localization precision	97
Figure A1.2	Stepping behavior of motor domain labeled kinesin-8/Kip3 and dynein	98
Figure A1.3	Two color, high-precision, single molecule co-localization of dual labeled dynein heterodimers	100
Figure A1.4	Distance between motor domains in the on- and off-axis directions	102
Figure A1.5	Effects of tension are not observed in the off-axis direction	104
Figure A2.1	Twelve-helix bundle DNA origami chassis design	110
Figure A2.2	Characterization of motor-chassis complex formation	111
Figure A2.3	DNA-PAINt analysis of handle incorporation in the chassis structure	112

Figure A2.4	Velocity, run length, and run time distributions of dynein-chassis complexes	113
Figure A2.5	Single-molecule motile properties of 4D and 7D chassis as a function of ion concentration	114
Figure A2.6	Velocity, run length, and run time distributions of kinesin-chassis complexes	115
Figure A2.7	Inactive motors decrease dynein-driven chassis velocity	116
Figure A2.8	Velocity and run times of mixed motor ensembles	117
Figure A2.9	Photocleavable handles can be used to detach motors from chassis	118
Figure A2.10	In rare cases, photocleavage induces chassis to switch directions	119

List of Tables

Table A1.1	Yeast strains used in this study	105
Table A1.2	Oligonucleotides used in this study	105
Table A1.3	Dimeric dynein motors used in this study	106
Table A2.1	Core staples to build the twelve-helix bundle	120
Table A2.2	Negative handle staples used to build the twelve-helix bundle	125
Table A2.3	Positive handle staples used to build the twelve-helix bundle	128
Table A2.4	Anti-handle oligonucleotide sequences	130
Table A2.5	Yeast strains used in this study	130
Table A2.6	Specifications for all chassis used in this study	131

Acknowledgements

As my undergraduate background was in physics, the prospect of initiating a biology-focused graduate research education was daunting. Without help and contributions from several people along the way, I would not have been able to make the transition to biophysics and cell biology. I am indebted to those people that have made this journey both possible and so enjoyable.

Dr. Andy Hoffman and Dr. Melissa Mazan at the Tufts Cummings School of Veterinary Medicine were the first to encourage and support my (then new-found) interest in biology. They trusted me with a set of pipettes (which were new instruments for me at the time!) and gave me the opportunity to join them in cell and physiological research projects. Working with them, and their colleagues, was a pivotal experience for me that helped shape and refine my interests and determination to pursue a Ph.D.

The Harvard Biophysics Program has been a perfect fit for me. Jim Hogle and Michele Jakoulov, extraordinary leaders of the program, have provided an ideal environment for multi- and inter-disciplinary exploration and research. Such is the freedom that this program offers its students that I often jokingly refer to it as the “choose your own adventure” program. And while this quip highlights the independence we are granted, it fails to properly acknowledge the support and leadership that Jim and Michele provide to the program. Not only were they always available to help, they also typically foresaw hurdles far in advance and worked tirelessly to diminish them. I also owe thanks to the Biophysics Program members who have served on my advisory and defense committees: Andres Leschziner, Joe Loparo, Jagesh Shah, and Peng Yin.

My colleagues in the Reck-Peterson and Shih laboratories have been generous, supportive and a delight with whom to work. I have learned so much from them, and this work is full of their contributions. In particular, I must acknowledge Julie Huang who taught me experimental design and trained me in biochemistry and bench techniques. She has led by both example and direct teaching, and many of my accomplishments are a result of her acumen. All of my major research projects were conducted in close collaborations. I would like to not only recognize, but also highlight, the contributions made by Weihong Qiu and Brian Goodman. The research presented here is equally theirs and I am both lucky and grateful to have worked with them on such challenging and exciting research. None of this would have been accomplished without their efforts. Andres Leschziner has also played a major role in my education. As well as being an exceptional scientist, he is a gifted speaker and teacher and I am greatly appreciative of his support and encouragement over the last 6 years.

I am incredibly fortunate to have worked under the guidance of Sam Reck-Peterson and William Shih. I could not ask for better or more genuine mentorship and support. In ways both subtle and direct they have made me a better scientist and a more critical thinker. I am grateful for their willingness to let me bring the expertise of their two labs together for my work and for their support and encouragement every step of the way. I've learned so much from them and this experience that I wish I were starting, rather than finishing, my projects with them.

Finally, thanks go out to my family for their energetic support and enthusiasm for my work. They always believed I could do this and I am grateful for their faith in me. My wife Katherine deserves particular thanks for her support and enthusiasm. It's been 8 (or is it 9?) years since I first quit my job to pursue an education and career in biological science. She has encouraged me and supported us tirelessly through that time. I never could have done this without her.

Chapter 1

Introduction

Nathan D. Derr

Introduction to cytoskeletal molecular motors

Eukaryotic cells face several logistical problems due to their size and complexity. One such obstacle is the need for sub-cellular spatial organization; many cellular structures have defined roles that require them to occupy specified locations within the cell. Many cellular processes are also time-sensitive and must occur not only in defined locations but also at precise times. The combination of these spatial and temporal requirements necessitates that cells have time-dependent spatial control over a wide variety of cellular moieties and processes. Additionally, the dramatic reorganization of the cytoplasm that occurs during cell division requires that these cells be able to exert forces over large intracellular distances. Impressively, cells achieve a high level of fidelity in spatial-temporal organization through the mechanisms of a robust and dynamic internal transport network (*I*).

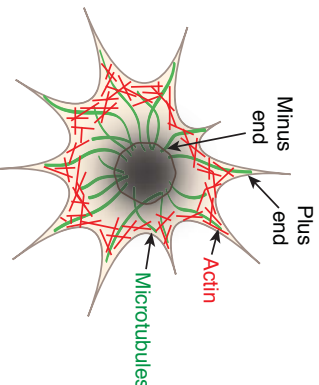


Figure 1.1 Schematic of a eukaryotic cell and its cytoskeletal filaments. Microtubules (green) and actin filaments (red) comprise the eukaryotic cytoskeleton. Microtubules are arranged radially within cells, with their slow-growing minus ends located near the cell center. Actin filaments are oriented transversely within the cell. Figure adapted from (60).

Comprised of cytoskeletal filaments

and motor proteins, this network enables eukaryotic cells to control the organization of their interiors (*I*). Two separate types of structures comprise the system's filamentous network: actin filaments and microtubules. In many eukaryotic cell types, microtubules are loosely oriented in a radial direction, stretching from the cell center and perinuclear region to the

cell periphery. Actin filaments, conversely, are

generally oriented in a transverse direction throughout the cell (Figure 1.1). Both of these filaments provide physical connections between distant intracellular regions, enabling them to transmit forces across the cell (2). Importantly, they also serve as roadways, or tracks, for motor proteins that “walk” along the filaments, hauling and distributing cargos as they move throughout the cell (1). This cargo distribution apparatus provides a robust means for cells to control spatial localization of many distinct cargos.

There are three families of motor proteins that interact with these cytoskeletal tracks.

Myosin motors move on actin filaments, while motors kinesin and dynein motors move on

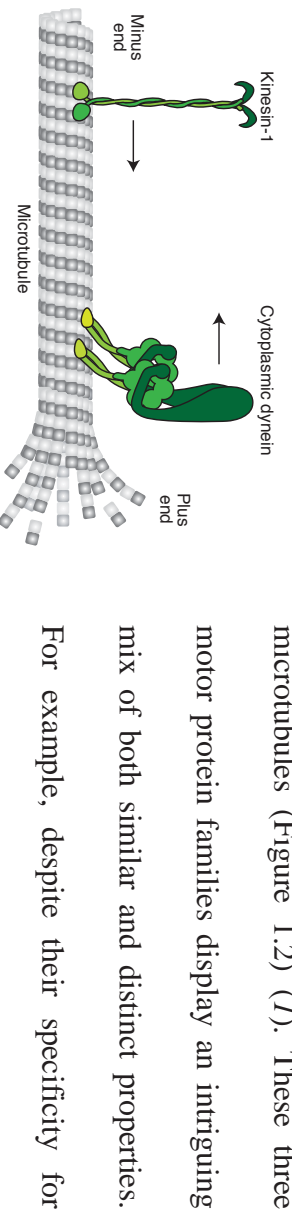


Figure 1.2 Cytoskeletal motors and their tracks. Microtubule-based motors (top) include kinesins and dyneins. Kinesin-1 moves along microtubules towards the microtubule’s fast-polymerizing plus end while cytoplasmic dynein moves towards the microtubule’s slow-polymerizing minus end. Myosin V comprises the actin-based motors (bottom). Myosin V moves along the actin filament towards the rapidly polymerizing plus end. Figure adapted from (60).

microtubules (Figure 1.2) (1). These three motor protein families display an intriguing mix of both similar and distinct properties. For example, despite their specificity for different tracks, myosin and kinesin are related to G proteins (3). There are more than 40 distinct isoforms of both myosins and kinesins that operate within the cell, with many of these isoforms having specialized

tasks (4, 5). (This introduction focuses on well-studied cargo hauling members of these motor families: myosin-V and kinesin-1 (hereafter, referred to as myosin and kinesin,

respectively.) Dynein, however, is structurally unrelated to myosin and kinesin; it is a member of the AAA+ ATPase family of proteins (6). Although dynein isoforms are found within flagella, cytoplasmic dynein is the only dynein family member found within the cytoplasm (hereafter referred to as dynein) (7). This fact does not, however, mean that dynein's cytoplasmic roles are limited; on the contrary, it has numerous roles within and beyond cargo hauling, including a primary role in cell division (7).

Motors must maintain at least one point of contact with their track, as otherwise thermal fluctuations within the cytoplasm will cause the cessation of their processive motility by forcing the rapid diffusion of the motors away from their tracks. As a mechanism to confront this issue, the cargo hauling members of these three motor families are all homodimeric (1). As each protomer within the homodimer contains a track binding domain, a consequence of being homodimers is the presence of two track binding sites within each motor. This structural organization allows one binding site to stay firmly attached to the track, while the other site releases the track and advances to a new binding site. This stepping mechanism is enabled by the binding and hydrolysis of ATP, which, along with providing the energy for these motors to move along their tracks and do work, also causes conformational changes within the protomers that drive the motors forward.

The microtubule filaments that serve as the tracks for kinesin and dynein are tubular polymers comprised of alpha- and beta-tubulin dimers. These dimers polymerize longitudinally to form protofilaments, while latitudinally they polymerize to form hollow cylindrical tubes,

typically containing 13 protofilaments around the circumference (2). The different ends of microtubules polymerize with very different kinetics. The so-called “minus” end of microtubules, typically located near the perinuclear region, polymerizes slowly, while the the “plus” end of the microtubule, which typically projects away from the cell center, grows rapidly

(8). Kinesin and dynein both interact with the microtubule in a polarized fashion; dynein walks

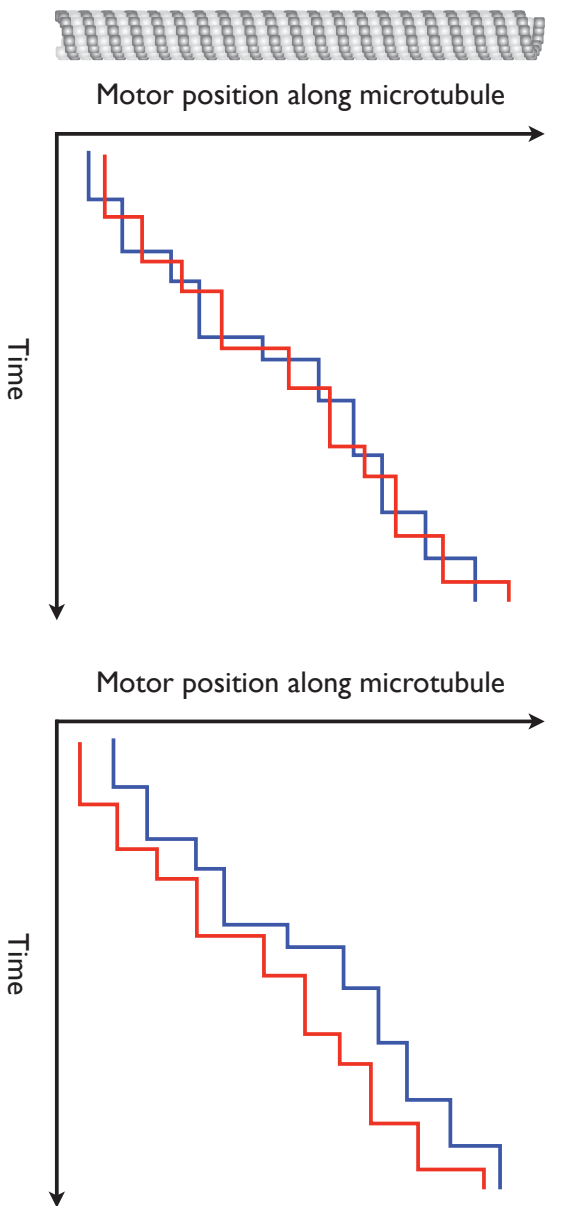


Figure 1.3 Simulated position vs. time traces for motor stepping models. **a)** Schematic diagram of a dynein motor. The motor is labeled on its motor domains with two different fluorophores. One fluorophore is blue, while the other is red. This labeling scheme enables the two motor domains to be independently observed using TIRF microscopy. Theoretical stepping patterns observable with this labeling scheme are shown in b) and c). **b)** Graph depicting simulated data representing a “hand-over-hand” stepping pattern. An idealized representative data trace would appear this way if the dynein motor shown in a) were to walk along microtubules with its two motor domains alternating stepping in time and alternating lead position along the microtubule. **c)** Graph depicting simulated data representing an “inchworm” stepping pattern. A representative simulated data trace would appear this way if the dynein motor shown in a) were to walk along microtubules with the blue motor domain always maintaining its role in lead position. Similarly to the idealized data in b), the motor domains alternate their steps in time.

towards the minus end (9), while most kinesins walk towards the plus end (4). This polarization of motility, combined with the organization of microtubule minus ends near the cell center, leads to a spatially oriented division of transport labor within cells. Dyneins move cargo from the cell periphery to the cell center, while kinesins move cargo in the opposite direction.

Biochemically and biophysically, dynein is substantially different from its counterparts. It is larger and more complex than both myosin and kinesin (10-12). This complexity may allow it to make up for its comparative lack of isoform diversity through tuning mechanisms within the cell that alter its functionality and thus enable it to perform diverse tasks. Dynein's size and relative complexity have made it more challenging to study, and consequently, much more is known about the biophysical interactions that lead to, and define, the stepping mechanisms of myosin and kinesin (13). For these motors, the two protomers within each homodimer coordinate their catalytic ATPase activity asynchronously, with each protomer stepping alternately with the other. In both cases, the motors walk with seemingly anthropomorphic "hand-over-hand" mechanism characterized by the stepping of the rear, or "lagging", protomer past the front, or "leading", protomer (Figure 1.3a,b) (14-16). In this way, the two protomers alter their leading or lagging identity with each step. Because the lagging protomer is always the one to release the track and step, the leading protomer stays bound to the track, thus ensuring that one point of contact between motor and track is always maintained (13). This coordinated stepping mechanism enables the motors to move processively, taking hundreds or thousands of consecutive steps.

How dynein coordinates its steps to achieve processive motility is not known (17). A full characterization of dynein’s stepping mechanisms requires knowledge of the relative spatial and temporal locations of the two protomers within the dynein dimer during the motor’s stepping cycle. One-color, single molecule analysis of dynein stepping has provided hints, but multiple stepping mechanisms are consistent with the data (17, 18). Two models of spatial-temporal coordination for dynein are prominent. The first is a hand-over-hand model (similar to myosin and kinesin), while the second is known as the “inchworm” model (18). This latter model is defined by the identities of the motor’s two protomers never changing: the leading protomer always leads and the lagging protomer always stays behind. In this model, the protomers alternate their steps temporally, but the protomers never pass one-another on their track. Every time the leading head steps, the lagging head steps to “catch-up” to, but not pass, the leading head (Figure 1.3a,c).

Dynein’s stepping coordination is an important facet of its overall mechanism and the determination of its stepping pattern comprises a major component of the work presented in this dissertation. Chapter two reports my work on the spatial-temporal relationship of dynein’s two protomers during processive motion and how the motor’s steps are coordinated. To address these questions, I created an approach that enabled direct, orthogonal observation of both protomers within the dynein motor.

Intracellular cargos often exhibit complex motile behavior characterized by variable velocities and distances traveled, pauses in motion, and reversals in the direction of motion. As

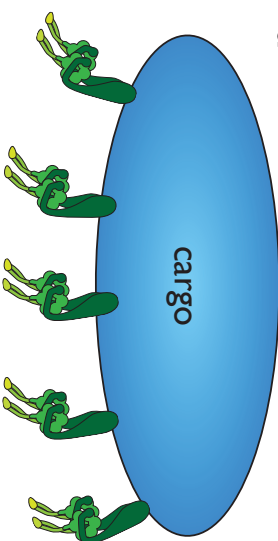
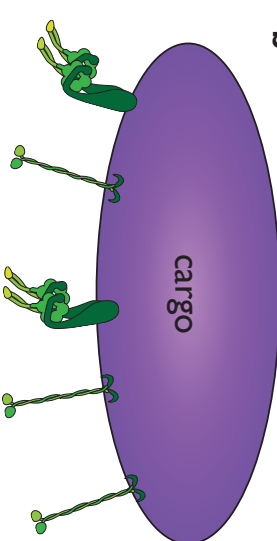
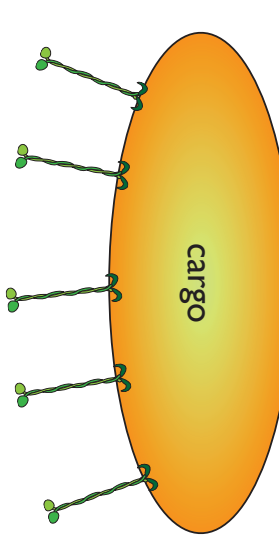
a**b****c**

Figure 1.4 Examples of microtubule-based motor ensembles. **a)** Schematic diagram depicting an intracellular cargo driven by a homomeric ensemble of five dynein motors. **b)** Schematic diagram of an intracellular cargo driven by a heteromeric ensemble of two dynein motors and 3 kinesin motors. **c)** Schematic diagram of an intracellular cargo driven by a homomeric ensemble of five kinesin motors.

cargos (22–26), but addressing these models *in vivo* is technically very challenging (27). Thus, the general underlying biophysical mechanisms that govern interactions between motors within ensembles are poorly understood and conceptually simply questions regarding these mechanisms remain unanswered. For example, the effect of motor copy number on cargo velocity is unknown

many intracellular cargos are hauled by teams of between 2 and 10 motors (19–21), these complex and variable motile characteristics have been hypothesized to be the result of the collective emergent behavior of motor ensembles.

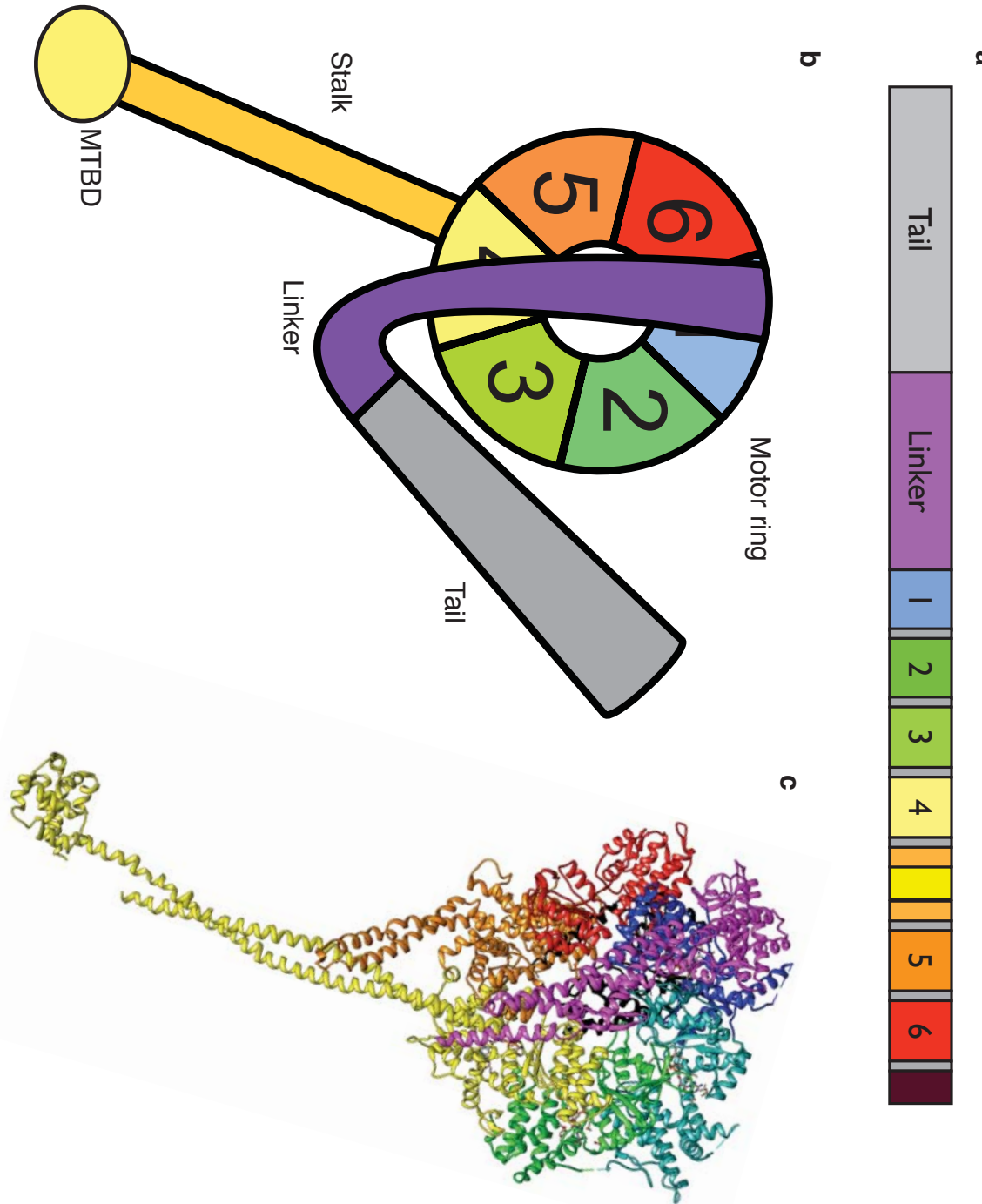
However, the degree to which this collective behavior is regulated by the cell, or dependent upon the biophysical interactions among the motors and their tracks, is not known. For cargos transported on microtubules, motor ensembles can be comprised of multiple dyneins, multiple kinesins, or a mixture of both kinesins and dyneins (Figure 1.4). How motors of both similar and opposite polarity within these

ensembles coordinate their stepping with one another is not known. Several theories have been proposed to explain interactions that could lead to the observed *in vivo* motile characteristics of

and how mixtures of dynein and kinesin coordinate to determine the net direction of motion of the cargo to which they are bound is not understood. Additional questions relate to the mechanisms that enable motors within an ensemble to coordinate their stepping, and whether such coordination leads to force output greater than that achievable by single motors acting alone. Ultimately, understanding how cells deliver cargos with high spatial and temporal fidelity requires an understanding of the nanoscale biophysics that govern the collective behavior of motor ensembles. Chapter three presents my work addressing these questions, for which I developed a synthetic system that enabled control over motor type, number and geometry on a synthetic cargo.

Addressing the questions of coordination at the levels of both single motors and motor ensembles required experimental systems offering a high degree of modularity. Thus, I utilized the modularity and hybridization specificity afforded by the chemistry of DNA (28) to enable each component within my experimental platforms to be treated as an interchangeable mechanical “standard part.” My methods allow both motors and motor domains to be physically coupled together through DNA hybridization to create complete and functional transport modules. These techniques offer a high degree of control over the physical architecture of motors and motor ensembles, thus enabling the construction of experimental platforms designed to answer specific questions about motor mechanisms.

Figure 1.5 Structure and domain architecture of the dynein heavy chain. **a**) Linear map of the dynein heavy chain domains. Numbers indicate AAA+ subdomains. **b**) Schematic of folded dynein heavy chain. Major domains within the motor are labeled. The microtubule binding domain (MTBD) is the domain that makes contact with the motor's microtubule track. **c**) Crystal structure of the dynein heavy chain (PDB 3QMZ (59)) lacking the tail. Domains are color coded to match a) and b).



Hows does dynein coordinate its stepping to move processively?

Single molecule observations have shown that dynein has a broad distribution of step sizes along the microtubule axis. These steps range from 4 nm (the distance between binding sites on the microtubule lattice (2)) up to several tens of nanometers and include off-axis (sideways) steps and steps in both the forward (minus end directed) and backward (plus end directed) directions (18). This is in stark contrast to kinesin, which takes regular 8 nm steps in its forward direction toward the microtubule's plus end (14). As kinesin and dynein share a binding site on the microtubule (29), such disparity in their stepping is likely due to differences in their structure and mechanism. The dynein holoenzyme contains two ~500 kD heavy chain protomers that form a homodimer essential for dynein function (18, 30). These heavy chains contain several sub-domains: the tail, linker, motor head, stalk, and microtubule binding domain (MTBD) (Figure 1.5) (31-33). The two heavy chain protomers are dimerized through the dynein's large tail domain (18). The motor ring domain is the site of catalytic activity in the motor; being a member of the AAA+ family of proteins, it contains 6 AAA+ sub-domains arranged in a continuous hexameric ring (6, 31, 32). Four of these sites bind ATP, with site number one being the primary and essential site for motor activity (34). The motor domain is connected to the tail through the linker domain, which swings across the dynein's ring during ATP binding and hydrolysis (33, 35). Finally, projecting radially outward from the motor ring at AAA+ domain number four is a coiled-coil stalk, the end of which contains the MTBD (36, 37). Notably, dynein's catalytic sites are located over 15 nm from the MTBD. Thus, the signals initiated by nucleotide binding and hydrolysis that control the motor's binding and unbinding from its track

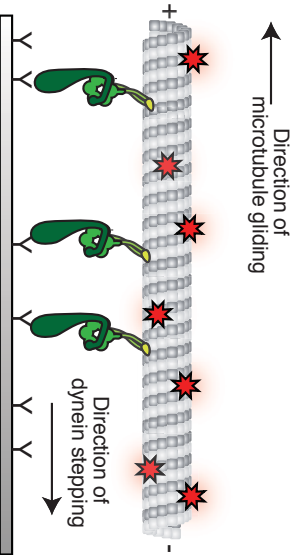
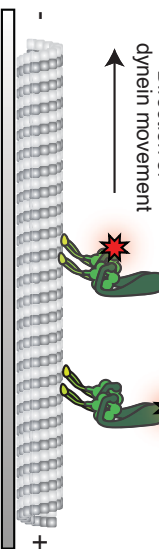
a**b**

Figure 1.6 Methods of observing dynein motility. **a)** In the “gliding assay” configuration, multiple dynein monomers can propel microtubules. In this configuration, dynein monomers are surface bound via an antibody to a microscope coverslip. Fluorescently labeled (red stars) microtubules are driven by the dynein motors. Many copies of the dynein monomers are required to maintain constant points of contact between the microtubule and the coverslip. **b)** Individual dynein motors can move processively along microtubule tracks. Dimerization is required so that each motor has two points of contact with its track. The dynein motor on the left is labeled with a red fluorophore on one of its motor domains. The dynein motor on the right is labeled with a red fluorophore on one of its tail domains. Figure adapted from (60).

require structural transmission from the motor domain, through the stalk, to the MTBD (37, 38). This, again, is in contrast to kinesin, which in addition to being a smaller motor, contains its catalytic ATP hydrolysis activity in close proximity to the microtubule (10).

Single dynein monomers working in concert

can move microtubules in a “gliding assay” type configuration due to the multiple points of contact between the motors and the microtubule

(Figure 1.6a, (18)). However, processive motion of individual dynein motors along microtubules requires the formation of a dynein homodimer (Figure 1.6b, (18)). Heavy chain protomers lacking the tail dimerization domain do not dimerize, and thus do not move processively. However, dynein motors can be artificially dimerized such that they maintain their

processivity. Recombinant dynein from the yeast *Saccharomyces cerevisiae* can be expressed with its tail domain replaced by the stable homodimer glutathione-S-transferase (GST). This “truncated dynein” is processive and moves at the single molecule level with great similarity to

native dynein (*18*). Importantly, dynein heterodimers can also be formed. Use of the FRB-rapamycin-FKBP system (*39*) has previously been used to form dynein heterodimers; these motors were motile and processive, but the low affinity of the rapamycin-mediated interaction led to low lifetimes of dimerization, a problem for single molecule assays where the total protein concentration must be sub-nanomolar (*18*).

Single molecule studies using native and this recombinant dynein led to an initial, but incomplete, understanding of the dynein stepping mechanism (*18*). In this work, dynein motors were fluorescently labeled with a quantum dot at either their tail or motor domain, enabling one-color, high-precision observation of the stepping patterns of these domains. As the tail domain was found to take a mean step of 8 nm and the motor domain a mean step of 16 nm, a hand-over-hand mechanism was a potential method of dynein stepping (*18*). However, these stepping data were also consistent with other models of motion, including “inchworm” stepping (*18*). In addition, the highly variable step size of the motor, which includes backwards and off-axis sideways steps, provided hints that dynein’s stepping was complex (*18, 40, 41*).

Although much can be learned from one-color signal molecule observations of motor stepping, a more ideal experimental system allows multiple domains within a single motor to be orthogonally labeled with different color fluorophores. Such systems have been used to directly observe the stepping pattern of myosin. In these studies, the two myosin protomers were labeled with different color fluorophores , allowing their relative spatial-temporal relationships to be determined (*15, 16*). Using TIRF microscopy and a high precision alignment between the red and

green emission channels in the microscope, the motor was found to follow a hand-over-hand type mechanism. As the myosin motor takes relatively long steps (72 nm) along its actin filament track, steric clashes did not prevent each protomer from binding a separate quantum dot (15). As quantum dots are typically in the 12-24 nm size range, this can be a problem in smaller stepping motors. Until recently (42), two-color quantum dot labeling of dynein had been unsuccessful, likely due to the large size of quantum dots as compared to the mean step size (16 nm) of dynein motor domains (18). For the small stepping motors kinesin and dynein, smaller fluorophores, such as organic small molecules, offer a technical trade-off: they are not as bright as quantum dots, but due to their small size, there is less potential for steric interactions and alterations of the motor mechanism.

Inspired by the observations of myosin's stepping (15, 16), we sought to directly observe orthogonally labeled, two-color dynein motors. However, a robust method for creating dynein heterodimers was needed to enable orthogonal labeling of each protomer with a different color organic fluorophore. Consequently, I developed methods utilizing DNA base-pairing to artificially dimerize dynein monomers. In chapter two, I present this work and our findings that dynein's method of coordination is dramatically different from those of kinesin and myosin. We show that dynein moves with a combination of both coordinated and stochastic stepping, dependent upon a tension based mechanism between the two motor domains within the functional heterodimer.

How do motors within an ensemble coordinate their interactions to collectively haul cargo?

A wide variety of intracellular objects serve as cargos for microtubule based motors. Among these cargos are mitochondria and organelles, such as endosomes, peroxisomes and lysosomes. When observed *in vivo*, these intracellular cargos exhibit complex motile characteristics (1). For example, sustained unidirectional cargo motility occurs with a broad distribution of velocities and total distances traveled. Interestingly, individual motile events often occur with velocities and run lengths greater than typically observed in single motors in *in vitro* experiments. In some cases, the velocity distributions of intracellular cargos have been found to be multi-modal (43, 44), leading to a controversial hypothesis suggesting that cargo velocity can be directly proportional to the number of motors hauling the cargo (45). In addition, motile events also include pauses, reversals, and both sustained uni- and bi-directional motility. As dynein and kinesin move in opposite directions on microtubules, changes in cargo direction are often attributed to a change in which motor type is engaged on the microtubule and powering the motion of the cargo. The underlying mechanisms that determine these motile characteristics are largely unknown.

Several hypotheses and models have addressed how interactions among motor ensembles might lead to the collective motile behavior observed *in vivo* (22-26). However, the complexity of the intracellular environment has made directly testing these hypotheses difficult (27). Primary hurdles include the difficulty of reliably determining discrete motor copy number *in vivo*; determining if motors are not only present on a cargo, but also actively engaged with the

microtubule; and determining the presence and effect of regulatory factors and other modulators of motor activity. Although a great deal is now known about the motile behaviors of individual motors (13, 17), extrapolating the effects of these attributes to motor ensembles is difficult, as the many parameters contributing to individual motor mechanism create a complicated biophysical system when combined into an ensemble (24, 46, 47). For example, attributes such as track affinity, duty ratio, stalling and unbinding forces, motor-track-cargo geometry and differential responses to forward and backward loads can all effect the collective behavior of motor ensembles (24, 46-52). Consequently, conceptually simple but critically important biophysical characterizations of motor teams are undetermined and controversial (19, 27, 45, 53).

A highly controllable *in vitro* system is needed to understand the specific motor attributes that lead to collective motor behavior (27). Structural DNA nanotechnology (28, 54) provides a method for creating a synthetic cargo system with attributes that enable the biophysical characterization of interacting motors (48, 55). In recent years, many techniques have been developed for building custom-designed shapes at the nanoscale using DNA as a construction medium. In these systems, the DNA sequence is used to encode structural information rather than genetic information -- by designing DNA sequences that allow only user -esigned hybridization to occur, a target shape can be self assembled through complimentary base pairing (28).

In particular, the methods of scaffolded DNA origami (56) offer a convenient means for building nanoscale objects at high yields with specified binding sites for motor proteins and other moieties, such as fluorophores, that enable single molecule observations (57, 58). These DNA

origami structures are designed with unpaired regions of single stranded DNA (ssDNA) that project outward in precisely defined locations from the otherwise compact DNA structure. Termed “handles,” these ssDNA projections serve as attachment points for anything bearing the complementary sequence (termed “anti-handles”). For example, chemical functionalizations such as biotin and small molecule fluorophores can be bound to the DNA origami structures with very

high affinity if they are covalently linked to the appropriate anti-handle sequences (57). Proteins bearing complimentary anti-handle strands can also be linked to the structures with this method (Figure 1.7).

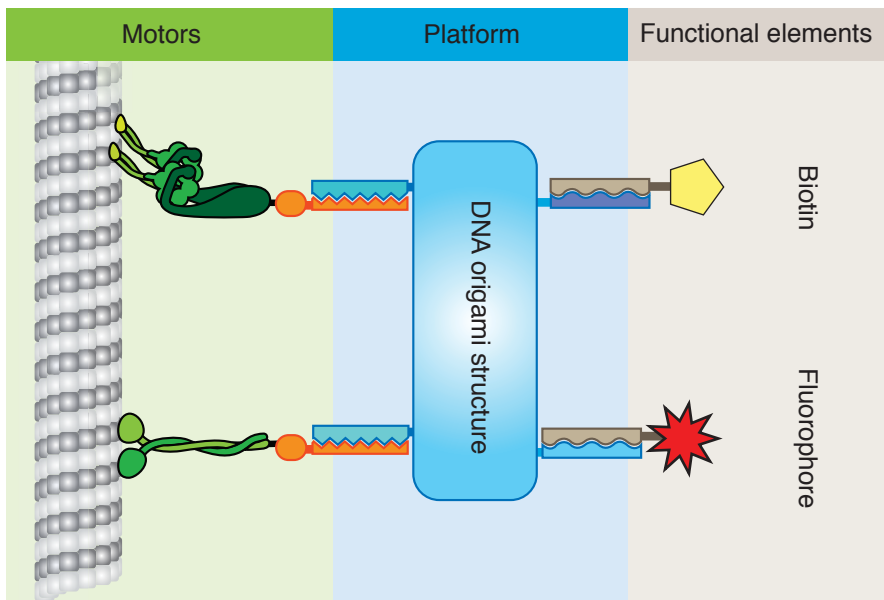


Figure 1.7 Schematic diagram of DNA origami based synthetic cargo system. DNA origami can be used to create a platform (middle) to which multiple moieties can be attached. Motors (bottom) are linked to the DNA origami structure through sequence specific DNA linkages. By moving on microtubules these motors provide motility for the platform. Functional elements (top) such as biotin and fluorophores can also be linked via sequence specific DNA attachments. These elements enable microscopy and other assays to be performed using the system. Figure adapted from (60).

By creating a programmable synthetic cargo and treating dynein and kinesin motors as standard, interchangeable parts, I have developed a system that enables motor ensembles to be built with a high degree of precision and specificity. Specifically, I have used DNA origami to create a synthetic cargo “chassis” to which defined numbers of motors can be attached, with control over motor type, location and stoichiometry. In chapter 3, I present this system and our initial results

studying the collective biophysical behavior of ensembles of well characterized model molecular motors. We show that ensembles of dynein from *S. cerevisiae* demonstrate enhanced run length and run time and diminished velocity with increasing motor number. Human kinesin constructs expressed in *E. coli* exhibit constant velocity and moderately enhanced run length and time with increasing motor number. When these motors interact in a mixed ensemble, motility driven by kinesin is infrequent; most ensembles are immobile or move in the dynein-driven direction. Disengaging one motor type from immobilized ensembles resolves this tug of war, enabling motility by the remaining motor type. This work suggests that many emergent behaviors of motor ensembles depend on attributes of the specific motors involved, a result highlighting the complexity of these biophysical interactions.

References

1. R. D. Vale, The molecular motor toolbox for intracellular transport, *Cell* **112**, 467–480 (2003).
2. E. Nogales, Structural insights into microtubule function, *Annu. Rev. Biochem.* (2000).
3. R. D. Vale, Switches, latches, and amplifiers: common themes of G proteins and molecular motors, *J. Cell Biol.* **135**, 291–302 (1996).
4. N. Hirokawa, Y. Noda, Y. Tanaka, S. Niwa, Kinesin superfamily motor proteins and intracellular transport, *Nat Rev Mol Cell Biol* **10**, 682–696 (2009).
5. T. Hodge, M. Jamie, T. V. Cope, A myosin family tree, *J. Cell. Sci.* (2000).
6. J. P. Ezzberger, J. M. Berger, Evolutionary relationships and structural mechanisms of AAA+ proteins, *Annu. Rev. Biophys. Biomol. Struct.* **35**, 93–114 (2006).
7. R. B. Vallee, J. C. Williams, D. Varma, L. E. Barnhart, Dynein: An ancient motor protein involved in multiple modes of transport, *J. Neurobiol.* **58**, 189–200 (2003).
8. A. Desai, T. J. Mitchison, Microtubule polymerization dynamics, *Annu. Rev. Cell Dev. Biol.* **13**, 83–117 (1997).
9. S. L. Reck-Peterson, N. D. Derr, N. Stuurman, Imaging single molecules using total internal reflection fluorescence microscopy (TIRFM), *Cold Spring Harb Protoc* **2010**, pdb.top73 (2010).
10. J. A. Spudich, Biochemistry. Molecular motors, beauty in complexity, *Science (New York, N.Y.)* **331**, 1143–1144 (2011).
11. A. P. Carter, C. Cho, L. Jin, R. D. Vale, Crystal structure of the dynein motor domain, *Science (New York, N.Y.)* **331**, 1159–1165 (2011).
12. T. Kon, K. Sutoh, G. Kurisu, X-ray structure of a functional full-length dynein motor domain, *Nat Struct Mol Biol* **18**, 638–642 (2011).
13. F. J. Kull, S. A. Endow, Force generation by kinesin and myosin cytoskeletal motor proteins, *J. Cell. Sci.* **126**, 9–19 (2013).
14. A. Yildiz, M. Tomishige, R. D. Vale, P. R. Selvin, Kinesin walks hand-over-hand, *Science (New York, N.Y.)* **303**, 676–678 (2004).
15. D. M. Warshaw *et al.*, Differential labeling of myosin V heads with quantum dots allows direct visualization of hand-over-hand processivity, *Biophysical Journal* **88**, L30–2 (2005).

16. L. S. Churchman, Z. Okten, R. S. Rock, J. F. Dawson, J. A. Spudich, Single molecule high-resolution colocalization of Cy3 and Cy5 attached to macromolecules measures intramolecular distances through time, *Proc. Natl. Acad. Sci. U.S.A.* **102**, 1419–1423 (2005).
17. A. Gennarich, R. D. Vale, Walking the walk: how kinesin and dynein coordinate their steps, *Current Opinion in Cell Biology* **21**, 59–67 (2009).
18. S. L. Reck-Peterson *et al.*, Single-Molecule Analysis of Dynein Processivity and Stepping Behavior, *Cell* **126**, 335–348 (2006).
19. S. A. Bryantseva, O. N. Zhapparova, Bidirectional transport of organelles: unity and struggle of opposing motors, *J. Cell Biol.* **36**, 1–6 (2011).
20. N. Hirokawa, S. Niwa, Y. Tanaka, Molecular motors in neurons: transport mechanisms and roles in brain function, development, and disease, *Neuron* **68**, 610–638 (2010).
21. M. A. Welte, Bidirectional Transport along Microtubules, *Current Biology* **14**, R525–R537 (2004).
22. S. Klumpp, R. Lipowsky, Cooperative cargo transport by several molecular motors, *Proc. Natl. Acad. Sci. U.S.A.* **102**, 17284–17289 (2005).
23. M. J. I. Müller, S. Klumpp, R. Lipowsky, Bidirectional Transport by Molecular Motors: Enhanced Processivity and Response to External Forces, *Biophysical Journal* **98**, 2610–2618 (2010).
24. D. K. Jamison, J. W. Driver, M. R. Diehl, Cooperative Responses of Multiple Kinesins to Variable and Constant Loads, *Journal of Biological Chemistry* **287**, 3357–3365 (2012).
25. A. Hendricks, B. Epureanu, E. Meyhofer, Collective dynamics of kinesin, *Phys. Rev. E* **79**, 031929 (2009).
26. R. P. Erickson, Z. Jia, S. P. Gross, C. C. Yu, How molecular motors are arranged on a cargo is important for vesicular transport, *PLoS Comput. Biol.* **7**, e1002032 (2011).
27. M. W. Elting, J. A. Spudich, Future challenges in single-molecule fluorescence and laser trap approaches to studies of molecular motors, *Dev. Cell* **23**, 1084–1091 (2012).
28. V. Linko, H. Dietz, The enabled state of DNA nanotechnology, *Curr. Opin. Biotechnol.* (2013), doi:10.1016/j.copbio.2013.02.001.
29. N. Mizuno *et al.*, Dynein and kinesin share an overlapping microtubule-binding site, *EMBO J.* **23**, 2459–2467 (2004).
30. J. R. Kardon, R. D. Vale, Regulators of the cytoplasmic dynein motor, *Nat Rev Mol Cell Biol* **10**, 854–865 (2009).

31. H. Schmidt, E. S. Gleave, A. P. Carter, Insights into dynein motor domain function from a 3.3-Å crystal structure, *Nat Struct Mol Biol* **19**, 492–7–S1 (2012).

32. T. Kon *et al.*, The 2.8 Å crystal structure of the dynein motor domain, *Nature* **484**, 345–350 (2012).

33. A. J. Roberts *et al.*, AAA+ Ring and linker swing mechanism in the dynein motor, *Cell* **136**, 485–495 (2009).

34. C. Cho, S. L. Reck-Peterson, R. D. Vale, Regulatory ATPase sites of cytoplasmic dynein affect processivity and force generation, *J. Biol. Chem.* **283**, 25839–25845 (2008).

35. S. A. Burgess, M. L. Walker, H. Sakakibara, P. J. Knight, K. Oiwa, Dynein structure and power stroke, *Nature* **421**, 715–718 (2003).

36. A. P. Carter *et al.*, Structure and functional role of dynein's microtubule-binding domain, *Science (New York, N.Y.)* **322**, 1691–1695 (2008).

37. T. Kon *et al.*, Helix sliding in the stalk coiled coil of dynein couples ATPase and microtubule binding, *Nat Struct Mol Biol* **16**, 325–333 (2009).

38. W. B. Redwine *et al.*, Structural basis for microtubule binding and release by dynein, *Science (New York, N.Y.)* **337**, 1532–1536 (2012).

39. L. A. Banaszynski, C. W. Liu, T. J. Wandless, Characterization of the FKBP-rapamycin.FRB ternary complex, *J. Am. Chem. Soc.* **127**, 4715–4721 (2005).

40. R. Malik, B. C. Carter, S. A. Lex, S. J. King, S. P. Gross, Cytoplasmic dynein functions as a gear in response to load, *Nature* **427**, 649–652 (2004).

41. Z. Wang, S. Khan, M. P. Sheetz, Single cytoplasmic dynein molecule movements: characterization and comparison with kinesin, *Biophysical Journal* **69**, 2011–2023 (1995).

42. M. A. DeWitt, A. Y. Chang, P. A. Combs, A. Yildiz, Cytoplasmic dynein moves through uncoordinated stepping of the AAA+ ring domains, *Science (New York, N.Y.)* **335**, 221–225 (2012).

43. D. B. Hill, M. J. Plaza, K. Bonin, G. Holzwarth, Fast vesicle transport in PC12 neurites: velocities and forces, *Eur Biophys. J.* **33**, 623–632 (2004).

44. C. Kural *et al.*, Kinesin and dynein move a peroxisome in vivo: a tug-of-war or coordinated movement? *Science (New York, N.Y.)* **308**, 1469–1472 (2005).

45. J. E. Martinez, M. D. Vershinin, G. T. Shubeita, S. P. Gross, On the use of in vivo cargo velocity as a biophysical marker, *Biochem. Biophys. Res. Commun.* **353**, 835–840 (2007).

46. R. D. Vale, F. Malik, D. Brown, Directional instability of microtubule transport in the presence of kinesin and dynein, two opposite polarity motor proteins, **119**, 1589–1596 (1992).
47. K. Uppulury *et al.*, How the Interplay between Mechanical and Nonmechanical Interactions Affects Multiple Kinesin Dynamics, *J. Phys. Chem. B* **116**, 8846–8855 (2012).
48. A. R. Rogers, J. W. Driver, P. E. Constantinou, D. Kenneth Jamison, M. R. Diehl, Negative interference dominates collective transport of kinesin motors in the absence of load, *Phys. Chem. Chem. Phys.* **11**, 4882–4889 (2009).
49. H. Lu *et al.*, Collective Dynamics of Elastically Coupled Myosin V Motors, *Journal of Biological Chemistry* **287**, 27753–27761 (2012).
50. J. Xu, Z. Shu, S. J. King, S. P. Gross, Tuning Multiple Motor Travel via Single Motor Velocity, *Traffic* **13**, 1198–1205 (2012).
51. M. Y. Ali *et al.*, Myosin Va and myosin VI coordinate their steps while engaged in an in vitro tug of war during cargo transport, **108**, E535–41 (2011).
52. A. Kunwar *et al.*, Mechanical stochastic tug-of-war models cannot explain bidirectional lipid-droplet transport, **108**, 18960–18965 (2011).
53. P. E. Constantinou, M. R. Diehl, The mechanochemistry of integrated motor protein complexes, *Journal of Biomechanics* **43**, 31–37 (2010).
54. N. C. Seeman, An Overview of Structural DNA Nanotechnology, *Mol Biotechnol* **37**, 246–257 (2007).
55. K. Furuta *et al.*, Measuring collective transport by defined numbers of processive and nonprocessive kinesin motors, *Proc. Natl. Acad. Sci. U.S.A.* **110**, 501–506 (2013).
56. W. M. Shih, C. Lin, Knitting complex weaves with DNA origami, *Current Opinion in Structural Biology* **20**, 276–282 (2010).
57. C. Lin *et al.*, Submicrometre geometrically encoded fluorescent barcodes self-assembled from DNA, *Nature Chem* **4**, 832–839 (2012).
58. B. Saccà *et al.*, Orthogonal protein decoration of DNA origami, *Angew. Chem. Int. Ed. Engl.* **49**, 9378–9383 (2010).
59. T. Kon *et al.*, The 2.8 Å crystal structure of the dynein motor domain, *Nature* **484**, 345–350 (2012).
60. B. S. Goodman, N. D. Derr, S. L. Reck-Peterson, Engineered, harnessed, and hijacked: synthetic uses for cytoskeletal systems, *Trends Cell Biol.* **22**, 644–652 (2012).

Chapter 2

Dynein achieves processive motion
using both stochastic and coordinated stepping

Weihong Qiu, Nathan D. Derr, Brian S. Goodman, Elizabeth Villa,
David Wu, William M. Shih and Samara L. Reck-Peterson

Contributions

Nathan Derr and Weihong Qiu contributed equally. Nathan Derr and Weihong Qiu initiated the project. Nathan Derr designed the DNA-based heterodimerization method. Weihong Qiu developed the 2D tracking methods. Weihong Qiu, Nathan Derr and Brian Goodman conducted the experiments and analyzed the data. Elizabeth Villa and David Wu wrote the 2D tracking software. Samara Reck-Peterson and William Shih provided mentorship. This work was published in: Dynein achieves processive motion using both stochastic and coordinated stepping, *Nature Structural Molecular Biology* **19**, 193–200 (2012).

Abstract

Processivity, the ability of single molecules to move continuously along a track, is a fundamental requirement of cargo-transporting molecular motors. Here, we investigate how cytoplasmic dynein, a homodimeric, microtubule-based motor, achieves processive motion. To do this, we developed a versatile method for assembling *Saccharomyces cerevisiae* dynein heterodimers, using complementary DNA oligonucleotides covalently linked to dynein monomers labeled with different organic fluorophores. Using two-color, single-molecule microscopy and high-precision, two-dimensional tracking, we find that dynein has a highly variable stepping pattern that is distinct from all other processive cytoskeletal motors, which use ‘hand-over-hand’ mechanisms. Uniquely, dynein stepping is stochastic when its two motor domains are close together. However, coordination emerges as the distance between motor domains increases, implying that a tension-based mechanism governs these steps. This plasticity may allow tuning of dynein for its diverse cellular functions.

Results

The microtubule-based motor cytoplasmic dynein (referred to here as dynein) powers the transport of a diverse array of cargos, allowing cells to organize their contents, move, divide, and respond to stimuli. Neurons and other long cells are especially sensitive to defects in transport; mutations in dynein motor-associated subunits lead to neurodevelopmental and neurodegenerative diseases (*1, 2*). Like other motors that move cargo over long distances, single dynein molecules move processively along their microtubule track (*3-8*). Dynein is the last class of cytoskeletal motor for which the mechanism of processive motility remains unknown.

Dynein's mechanism continues to be mysterious due to its enormous size and complexity (*9*). The dynein holoenzyme is composed of two ~500 kDa motor (or "head") containing heavy chain subunits and at least 6 other polypeptides. The domain structure of the dynein heavy chain is shown in Figure 1a. The N-terminal "tail" domain represents ~30% of the entire mass of the heavy chain and is required for dimerization and the interaction of most dynein subunits and associated proteins. Connected to the tail is the "linker" domain, which is thought to amplify structural changes during dynein's ATPase cycle and is required for motility (*5, 10-12*). Following the linker domain are six concatenated AAA+ (ATPase Associated with diverse cellular Activities) domains, which fold into a ring. As a member of the AAA+ superfamily, dynein is evolutionarily distinct from kinesin and myosin, which are distantly related to G-proteins (*13*). Dynein's first AAA+ domain is the primary site of ATP hydrolysis (*14*), but AAA+ domains 2–4 are also expected to bind ATP or ADP based on mutant phenotypes (*5, 15-17*). Projecting from the fourth AAA+ domain is a 15 nm, antiparallel, coiled-coil "stalk" capped by a globular microtubule-binding domain (*18-20*).

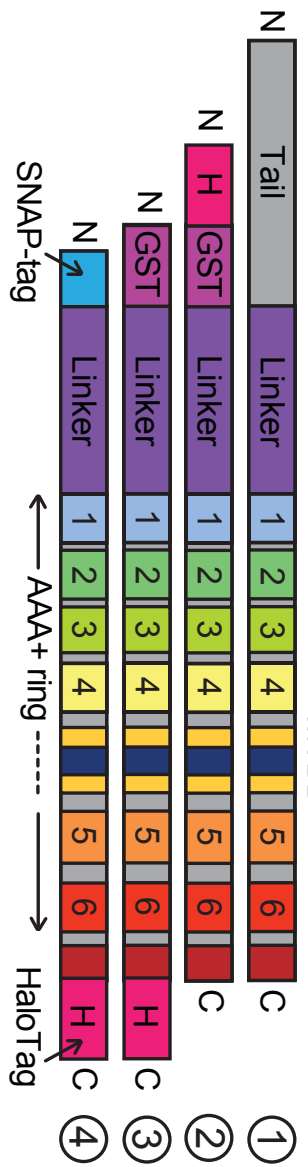
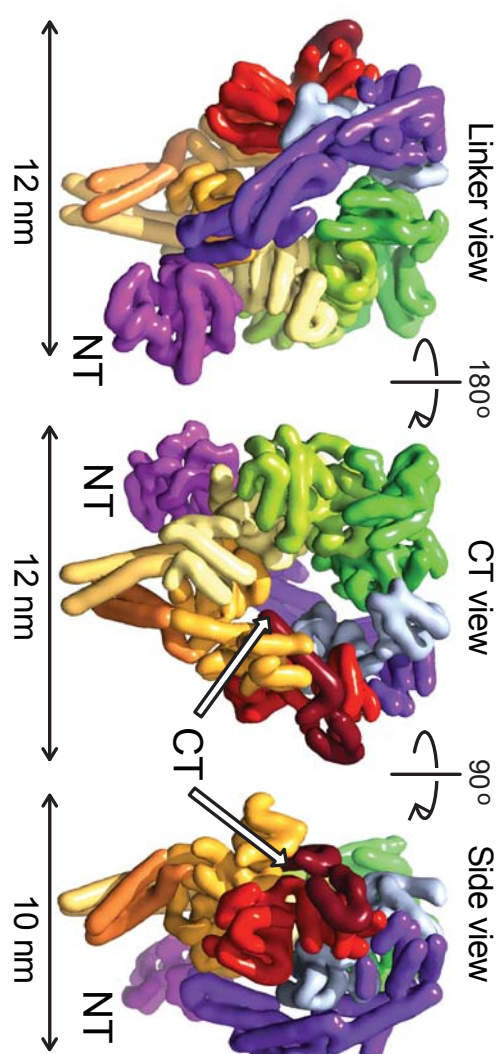
a**c**

Figure 2.1 Dynein structure and constructs used in this study. (a) Linear diagrams of native dynein's domain structure (1) and constructs used in this study: GST-dimerized dynein with an N-terminal HaloTag (H) for tail-labeled experiments (2); dynein monomer with a C-terminal HaloTag for motor domain-labeled experiments (3); dynein monomer with an N-terminal SNAP-tag for DNA dimerization and a C-terminal HaloTag for motor domain labeling (4). MTBD, microtubule-binding domain. (b) Two-dimensional schematic of dimeric dynein. Dimerization (white box) can be achieved using the native protein dimerization domain, GST or complementary DNA oligomers attached through a SNAP-tag. (c) Three-dimensional structure of yeast dynein (PDB 3QMZ (18)), filtered to 8 Å resolution. Views from left to right: the linker face, the opposite face of the ring containing the C-terminal (CT) alpha helix, and the side of the ring. Dimerization is achieved through GST (magenta) at the N terminus (NT).

Despite the complexity of the dynein motor, a dimer of two truncated *Saccharomyces cerevisiae* dynein heavy chains is sufficient for processive motility (5, 21). Previously we showed that dynein monomers lacking most of the tail domain were not processive on their own, but moved processively when they were linked together with glutathione S-transferase (GST, a stable homodimer) (5) (Fig. 2.1b). GST–dynein homodimers behaved similarly to native yeast dynein with respect to velocity, processivity, stepping behavior, and force production *in vitro* (5, 22), demonstrating that the native dimerization interface is not required for motility and suggesting that the basic motile mechanism is insensitive to the method of dimerization.

However, how dynein achieves processive motility remains unknown. For the well-studied kinesin-1 and myosin-V motors, nucleotide-driven conformational changes of their mechanical elements power the sequential “hand-over-hand” stepping of their two identical motor domains (23–27). Previously, to investigate the dynein stepping mechanism, we labeled GST–dynein homodimers with a single Quantum dot (Qdot) on a single motor domain or on the tail domain (approximate center of mass). High-precision one-dimensional stepping analyses revealed that the motor domain step size was nearly twice the size of the tail step size, consistent with a model in which dynein’s two motor domains alternate their position in time and pass each other in space (5). However, unlike kinesin, dynein takes steps of variable size and direction (23–27), making other stepping patterns theoretically possible (5). Dynein’s variable stepping behavior is likely due to its large size (10, 12, 28), which allows the motor rings to separate and access multiple microtubule binding sites. While advances in understanding the architecture of the dynein motor domain have come from two near-atomic resolution crystal structures (18, 20)

(Fig. 2.1c), how dynein's two motors are arranged on the microtubule when moving processively also remains unknown. Here, we set out to determine how dynein achieves processive motility.

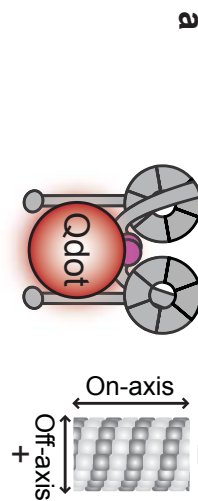
A major barrier to determining the dynein stepping pattern and its structural basis is the lack of an efficient system to make high-affinity, functional heterodimers, so that each protomer can be probed independently. We have created *S. cerevisiae* dynein heterodimers labeled with two distinct fluorophores through base-pairing of covalently-attached, complementary DNA oligonucleotides. DNA-dimerized dynein behaves indistinguishably from native dynein and protein-based dynein homodimers (5, 22). Using two-color, single-molecule microscopy coupled with high-precision, two-dimensional particle tracking, we find that dynein has a highly unusual stepping pattern compared to processive kinesins and myosins. We show that dynein's two motor domains can step both alternately and non-alternately in time, and can either pass or not pass each other in space. Surprisingly, we have found that many dynein steps are uncoordinated, but become coordinated as the distance between the two motor domains increases. These results suggest that dynein can switch between stochastic and tension-based stepping, making it distinct from all two-headed processive motors.

Because dynein's steps are known to have an off-axis component (5, 8), analysis of stepping projected onto one dimension (1-D) along the microtubule axis (as is standard in the field) could yield an underestimate of dynein's true step size. To determine the step size of dynein in two dimensions (2-D), we implemented a custom step-finding program (see Methods). Before analyzing dynein's stepping behavior in 2-D, we first determined the measurement precision of our total internal reflection fluorescence (TIRF) microscope to be ~1.5 nm for Qdot 655 and ~3.5 nm for the organic fluorophores Atto647N and Cy3B (Fig. A1.1a–c; Methods). As

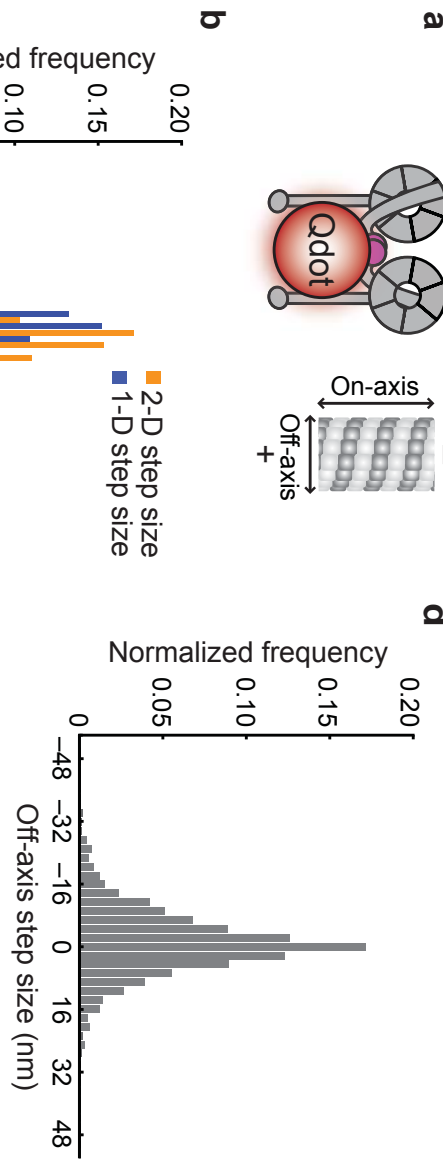
an additional control for the precision of our methods, we performed 1-D and 2-D stepping experiments with the yeast kinesin-8/Kip3 (29). We found that kinesin-8/Kip3 labeled on a single motor domain takes ~16 nm steps (Fig. A1.2a-d), similar to other kinesin family members (27).

To determine the 2-D step size of dynein, we tracked the stepping of GST-dynein homodimers labeled with a single Qdot 655 placed on either the tail domain (via an N-terminal HaloTag; Figs. 1a and 2a-e) or on a single motor domain (via a C-terminal HaloTag; Fig. 2.1a and Fig. A1.2e-j) (5). Our new analysis method revealed that the 2-D step size of tail-labeled dynein was ~10 nm (Fig. 2.2b), which is larger than the originally reported 1-D step size. However, when the 2-D data was projected onto the direction of motion along the microtubule axis, we observed an ~8 nm 1-D step size (Fig. 2.2b), in agreement with previous 1-D on-axis step sizes reported for dynein (5, 7, 22). Observation of a fluorophore on a single motor domain (head-labeled) resulted in a 2-D step size of ~14–16 nm, while the 1-D on-axis step size was slightly smaller (Fig. A1.2i). As reported previously, we found that the majority of dynein steps were in the forward direction (Fig. 2.2c and Fig. A1.2j) (5).

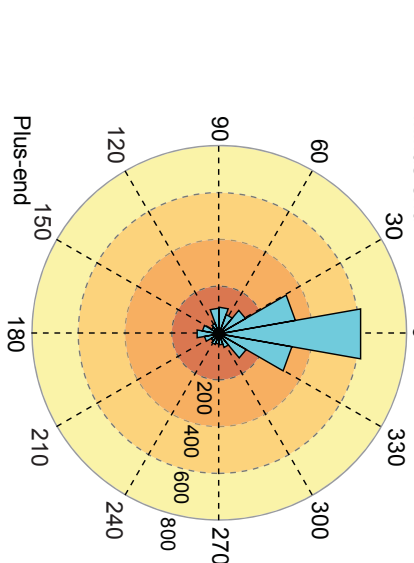
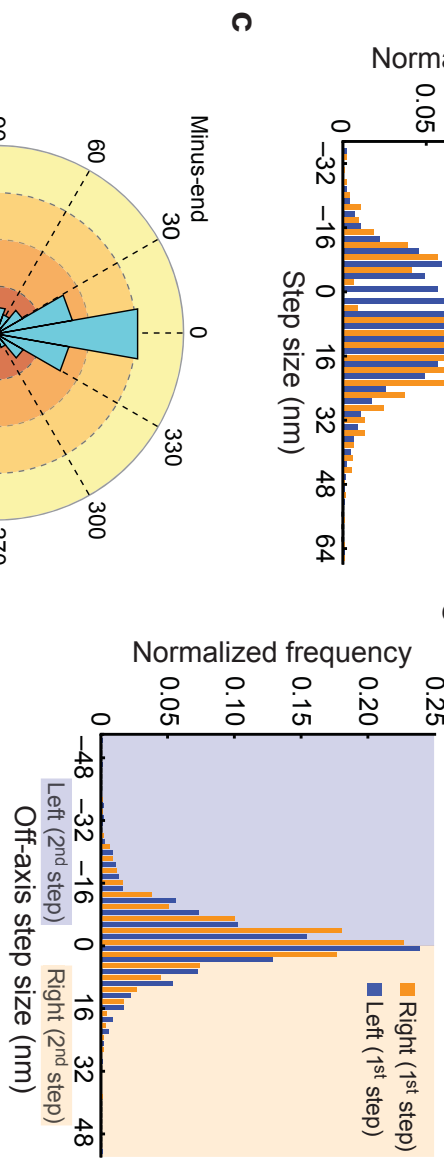
Analysis of the 2-D stepping data allowed us to determine the step size and angle of dynein's off-axis steps for the first time. We found that many steps taken by the tail-labeled dynein and the single motor domain-labeled dynein contained an off-axis component > 6 nm (Fig. 2.2d, Fig. A1.2g.). By contrast, most kinesin-8/Kip3 steps did not contain an off-axis component (Fig. A1.2c), similar to other kinesins (30, 31). The percentage of off-axis steps observed here was higher than previously reported (5), most likely due to our development and implementation of the 2-D stepping algorithm, which allows a more accurate and thorough classification of the off-axis component of dynein stepping. However, both the curvature of the



a



e



c

Figure 2.2 Two-dimensional stepping analysis of GST-dynein homodimers. (a) Schematic of a GST-dynein homodimer labeled with a Qdot through an N-terminal (tail domain) HaloTag and a diagram of a microtubule showing on- and off-axis directions of movement. (b) Histograms of dynein's step sizes in one (1D) and two (2D) dimensions. $N = 1,391$ steps for all panels. (c) An angle histogram (or rose plot) of the step angles. The stepping angle is defined as the angle between the stepping vector and the direction of on-axis movement. Steps to the left or right of the direction of motion are between 0° and 180° or between 180° and 360° , respectively. Steps between 90° and 270° are backwards steps. (d) Histogram of off-axis step sizes. (e) Histograms of leftward or rightward steps after a previous left or right step. Leftward and rightward steps are shown as steps with negative and positive off-axis components, respectively.

microtubule and the geometry associated with the distance between the fluorophore on the dynein motor domain and dynein's microtubule-binding domain could introduce additional sources of error for measurements in the off-axis direction. Thus, distances measured in the off-axis direction may be an underestimate and dynein may take more frequent and larger off-axis steps than we can detect.

The 2-D analysis also allowed us to investigate whether dynein has a preference for stepping to the left or right. We calculated the probability that an off-axis step is followed by another off-axis step in the same direction (for example, how likely it is that a leftward step is followed by another leftward step). For tail-labeled dynein, for which every step is observed, dynein is equally likely to step to the left or the right (Fig. 2.2e), irrespective of the direction of a prior off-axis step. In summary, by analyzing dynein stepping in two dimensions, we have found that dynein's true step size is larger than the previously reported 1-D step size, many steps contain an off-axis component, and steps are equally likely to be to the left or to the right.

To determine how dynein's two motor domains move processively, we next wanted to examine the stepping behavior of each of dynein's two motor domains independently. Our prior work used a rapamycin–FKBP–FRB-mediated heterodimer (5), however this complex has lower affinity (32) than is desirable for creating robust and stable heterodimers at the low protein concentrations necessary for single molecule experiments. Instead, we chose a DNA-based dimerization approach that achieves high affinity (subfemtomolar for a 21 base-pair duplex at 22°C (33)), combinatorial flexibility, and allows individual modification of each protomer within the dimer (34). We reasoned that the dynein molecule would be amenable to this method, since its dimerization interface exhibits great plasticity (5). Furthermore, the DNA dimerization

interface should be stable under load as yeast dynein's maximum force generation has been measured to be ~7 pN (22), whereas "unzipping" DNA requires a force of ~14 pN (35).

To make DNA-based dynein dimers, we engineered a dynein monomer fusion protein in which the SNAP-tag replaced the N-terminal dimerization domain of the endogenous dynein heavy chain (Fig. 2.1a,b). Like the Qdot-labeled dynein motors, this dynein monomer is also fused to a HaloTag at the C terminus of the motor domain to enable fluorophore labeling (Figs. 2.1a and 2.3a). Both the SNAP-tag and HaloTag are small enzymes that form covalent bonds with substrates that can be coupled to fluorophores, biotin, or reactive chemical groups. Taking advantage of the flexibility of the SNAP-tag, we next coupled the 5' or 3' end of complementary, 21 nucleotide DNA oligonucleotides to the SNAP substrate, benzylguanine (BG), and the DNA–BG molecules were then mixed with purified, SNAP-tagged dynein monomers. We found that this dimerization method was highly specific, with dynein monomers attached to complementary oligomers forming stable dimers, but not in the presence of excess, competing oligomers (Fig. 2.3b, compare lanes 3 and 4).

To determine if DNA-dimerized dynein was functional, we compared its motility and stepping pattern to GST–dynein homodimers. Each dynein monomer was labeled with a different small organic fluorophore (TMR or Atto647N) via the C-terminal HaloTag prior to dimerization (Fig. 2.3a). Using TIRF microscopy, we found that the majority of moving motors were dual-labeled (Fig. 2.3c), and their velocities and run lengths were similar to GST–dynein homodimers (Fig. 2.3d,e). As a more stringent test of functionality, we determined the 2-D step size and dwell time distribution of DNA–dynein dimers by labeling their tail domains with a Qdot 655. Again, we found these parameters to be comparable to that of GST–dynein homodimers (Fig. 2.3f–h).

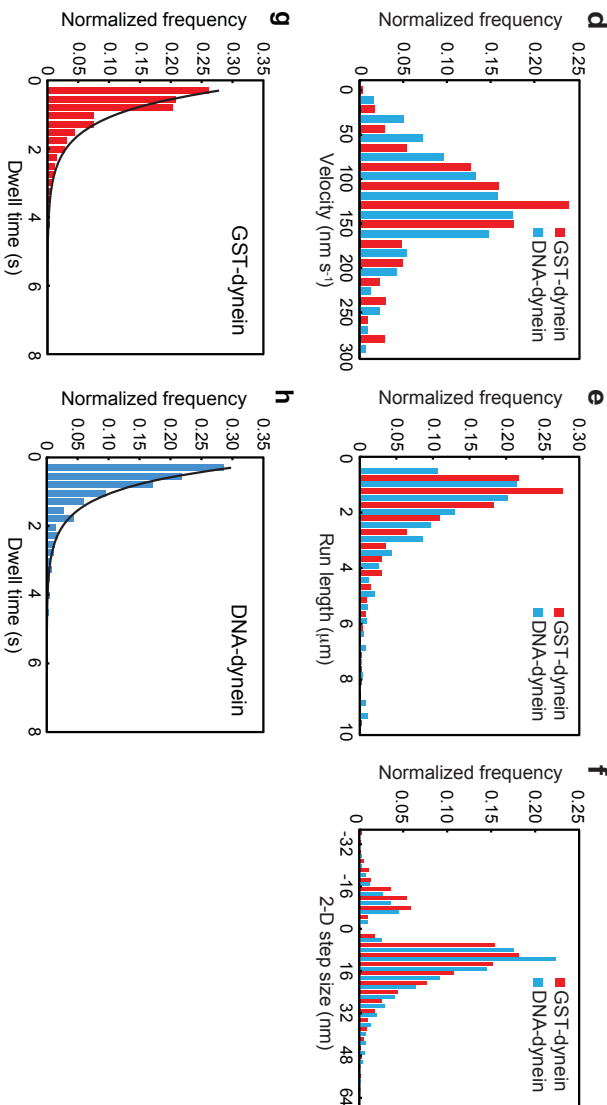
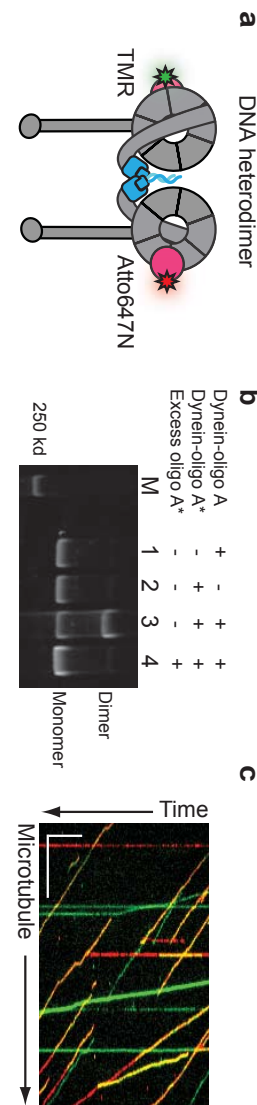


Figure 2.3 DNA-based dynein heterodimers are functional and step similarly to protein-based dynein homodimers. (a) Schematic of a DNA-based dynein heterodimer labeled with Atto647N (red star) and TMR (green star) through a C-terminal HaloTag (pink circles). The SNAP-tag and DNA oligomers (attached through the N-terminal SNAP-tag) are shown in blue. (b) LDS-PAGE gel showing dimerization of dynein monomers through DNA hybridization. Oligo, oligonucleotide. (c) Kymograph of the motility of DNA-based dynein dimers labeled with TMR (green) and Atto647N (red), with overlapping, dual-labeled heterodimers in yellow. Scale bars: y, 1 min; x, 10 μm . (d) Histograms of the velocity of GST- and DNA-based dynein dimers. (e) Histograms of the run length of GST- and DNA-based dynein dimers. (f) Histograms of the two-dimensional (2D) step size of GST- and DNA-based dynein dimers labeled with a single Qdot 655 on the N-terminal tail domain. (g,h) Histograms of the dwell time distribution of GST-dynein homodimers (g) and DNA-dynein heterodimers (h) labeled with a single Qdot 655 on the N-terminal tail domain. The distributions are fit to single exponential functions with stepping rates of $k = 1.78 \pm 0.13 \text{ s}^{-1}$ and $1.43 \pm 0.10 \text{ s}^{-1}$, respectively.

Importantly, the stepping behavior of DNA-dynein heterodimers was also similar to native yeast dynein analyzed at both rate limiting and cellular ATP concentrations (5, 22), a further indication that both the method of dimerization and low ATP concentrations (to slow the speed of the motor) used in our experiments do not alter the dynein stepping behavior. Together, these results indicate that DNA-dynein heterodimers are an excellent model system for dissecting the dynein stepping mechanism.

All dimeric processive myosin and kinesin motors studied to date achieve processive motility by alternating the position of their two motor domains in both space and time (hand-over-hand stepping). We sought to determine if dynein had a similar spatial and temporal pattern of stepping. To do so, we used our DNA dimerization method to construct dynein heterodimers labeled with the bright fluorophores Cy3B and Atto647N, which are much smaller (~ 2 nm in size) than Qdots (typically > 15 nm, larger than a dynein motor domain), and thus unlikely to interfere with dynein's motion. Dual-labeled dynein motors were imaged using near-simultaneous, alternating-excitation, high-precision TIRF microscopy under rate-limiting ATP conditions. We located the centroid position of each fluorophore-labeled motor domain with high precision by applying a 2-D Gaussian fit to the data from each channel (36), allowing for a position measurement precision of ~3.5 nm in both the x and y directions for both the Atto647N and Cy3B channels (Fig. A1.2b,c; see Methods). To precisely co-localize the Cy3B and Atto647N data, we applied the Single molecule High Resolution Co-localization (SHREC) method (37), which yielded a mean mapping error of ~4 nm in both the x and y directions, and an overall uncertainty in our measurements of ~6 nm (Fig. A1.3a,b; see Methods).

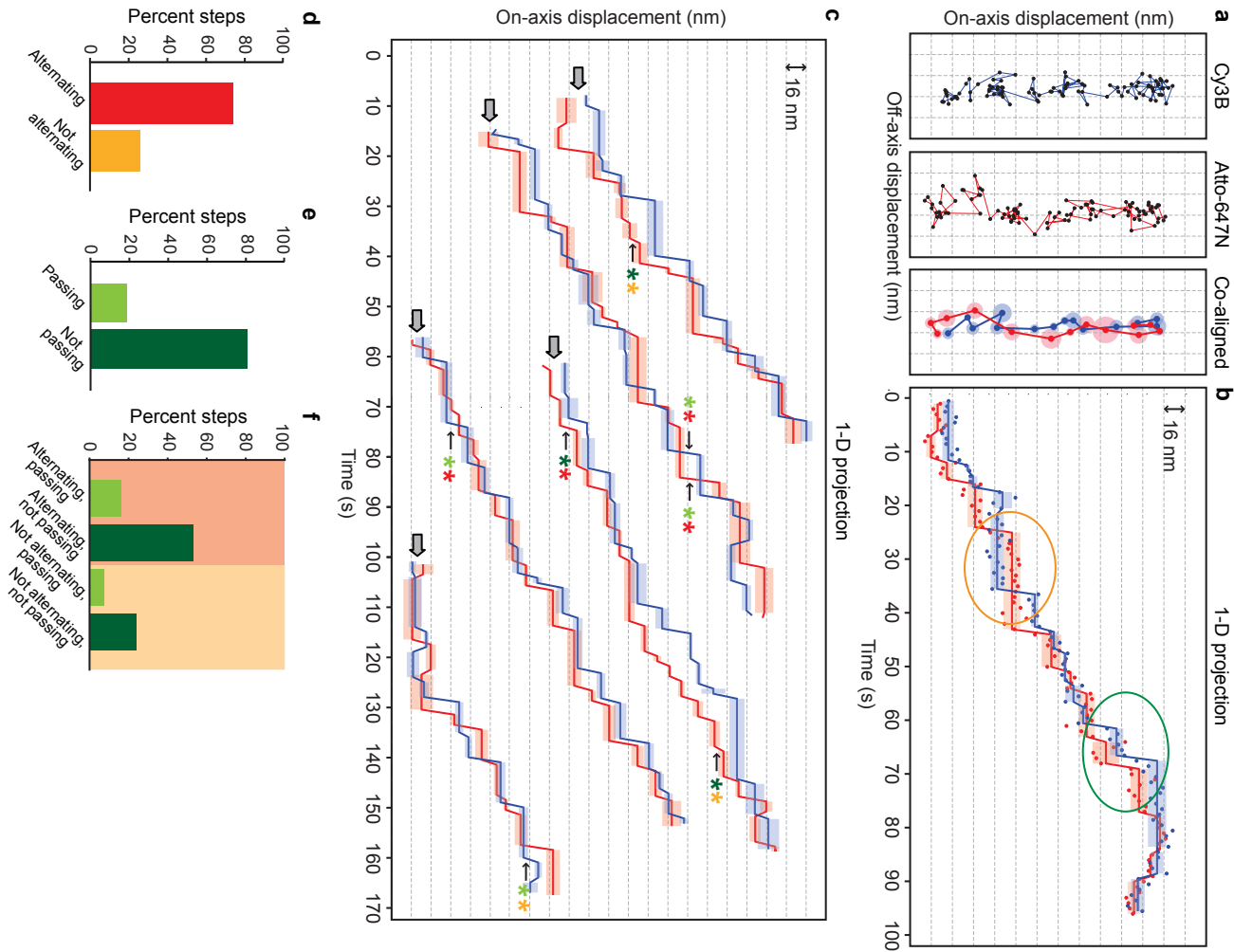


Figure 2.4 Two-color tracking of dynein stepping. (a) Representative two-color stepping trace of a DNA-dynein heterodimer. Left and center panels, raw two-dimensional positions (black dots in left and center panels) from a DNA-dynein heterodimer labeled with Cy3B and Atto647N. Right panel, co-alignment of the motor domain traces from each channel. Darker blue (Cy3B) and red (Atto647N) lines and dots represent steps determined by a two-dimensional step finding algorithm; larger, lighter-colored blue and red circles represent the s.d. of individual steps. (b) One-dimensional on-axis projection of the two-dimensional data from a, with lighter blue and red bars representing the s.d. of individual steps. Ovals highlight examples of hand-over-hand (orange) or inchworm (green) steps. The y-axis grid lines are spaced 16 nm apart in all panels. (c) Examples of one-dimensional on-axis projections of two-color stepping trace pairs from dual-labeled DNA-dynein heterodimers colored the same as in b. Grey arrows, start of each trace. Light green and red asterisks, alternating and passing steps (hand-over-hand); dark green and light orange asterisks, not alternating and not passing steps ('inchworm'); light green and light orange asterisks, not alternating and passing steps; dark green and light orange asterisks, not alternating and not passing steps. (d) Temporal analysis of the relative frequency of stepping events. Alternating, current and previous stepping events originating from different heads; non-alternating, current and previous stepping events originating from the same head. N = 268. (e) Spatial analysis of the relative frequency of passing or not passing stepping events. N = 233. (f) Combined temporal and spatial analysis of stepping events. N = 135.

Images from the Cy3B and Atto647N channels were screened for dual-labeled motile molecules with clearly defined 2-D stepping clusters (see Methods). We analyzed 27 different two-color dynein stepping trace pairs, containing 708 steps (Fig. 2.4a,b; Fig. A1.3c–l). The average 1-D, 2-D (compare Fig. A1.2i with Fig. A1.3g,h) and off-axis step sizes (compare Fig. A1.2g with Fig. A1.3i,j) were similar to the motor domain step sizes we observed for Qdot labeled GST-homodimers. Additionally, the 1-D on-axis step sizes (Fig. A1.3g,h) we observed in each channel for the DNA–dynein were also very similar to those that we previously measured for full-length native yeast cytoplasmic dynein (5), another indication that the DNA-dimerization method is an excellent model system for examining the dynein stepping mechanism.

Labeling each of dynein’s two motor domains with different colored fluorophores allowed us to observe spatial and temporal relationships of the motor domains during processive motion (Fig. 2.4a,b; Fig. A1.3c–f). Here we use the terms “alternating” or “not alternating” to describe the motor domains relative temporal behavior, and “passing” or “not passing” to describe their relative spatial behavior. We found that the majority (~74%) of dynein steps alternated in time (each head “taking turns” stepping), but non-alternating events (a single head taking multiple steps in a row) were also observed (Fig. 2.4b–d; Fig. A1.3d,f). In our spatial analysis of dynein stepping, we found that the majority (~83%) of dynein steps did not pass each other (leading and lagging heads maintained their identity), although passing events (one head switching from the leading to the lagging position) were also observed (Fig. 2.4b,c,e; Fig. A1.3d,f). These results (Fig. 2.4f) are in marked contrast to the well-studied two-headed processive kinesin and myosin motors, which alternate their steps in time and pass one another in space, the combination of which results in hand-over-hand stepping (26, 27).

Despite recent reports of dynein's motor domain structure at near atomic resolution (18, 20), the position and orientation of each motor domain within the dimer when bound to microtubules remain unknown. Therefore, we next determined the distance between dynein's motor domains in the "two-head-bound state", when both heads were simultaneously bound to the microtubule (Fig. 2.5a, b, and Fig. A1.4a-c). Given that the dimensions of a dynein motor domain are ~12 nm (diameter of the AAA+ ring) \times 10 nm (thickness of the AAA+ ring and linker) (Fig. 2.1c), our data suggest that the dynein motor domains are positioned close together. However, to accommodate the largest distances we observed between motor domains (4% of head-to-head distances were > 30 nm), linker domain undocking from the motor domain likely occurs, a phenomenon that has been observed in electron microscopy studies of both cytoplasmic and axonemal dyneins (10, 12). In addition, unlike other cytoskeletal motors, the distribution of head-to-head distances for dynein was broad and varied widely within individual traces (Fig. 2.4a-c and Fig. A1.3c-f), further highlighting the unusual nature of dynein's stepping mechanism.

Our 2-D tracking of dynein stepping also allowed us to determine the spatial relationship of each dynein motor domain in the two-head-bound state relative to the direction of motion along the microtubule (Fig. 2.5a). Analysis of the position of each of dynein's motor domains revealed that the leading head was more likely to be to the right of the axis of motion, while the lagging head was more likely to be to the left of the axis of motion (Fig. 2.5c). This analysis included only motors with statistically resolvable leading or lagging and left or right positions (two-tailed Student's t-test with alpha 0.05). We also performed this analysis on our entire data set and observed the same trend (Fig. A1.4d). This observation suggests that the two motor

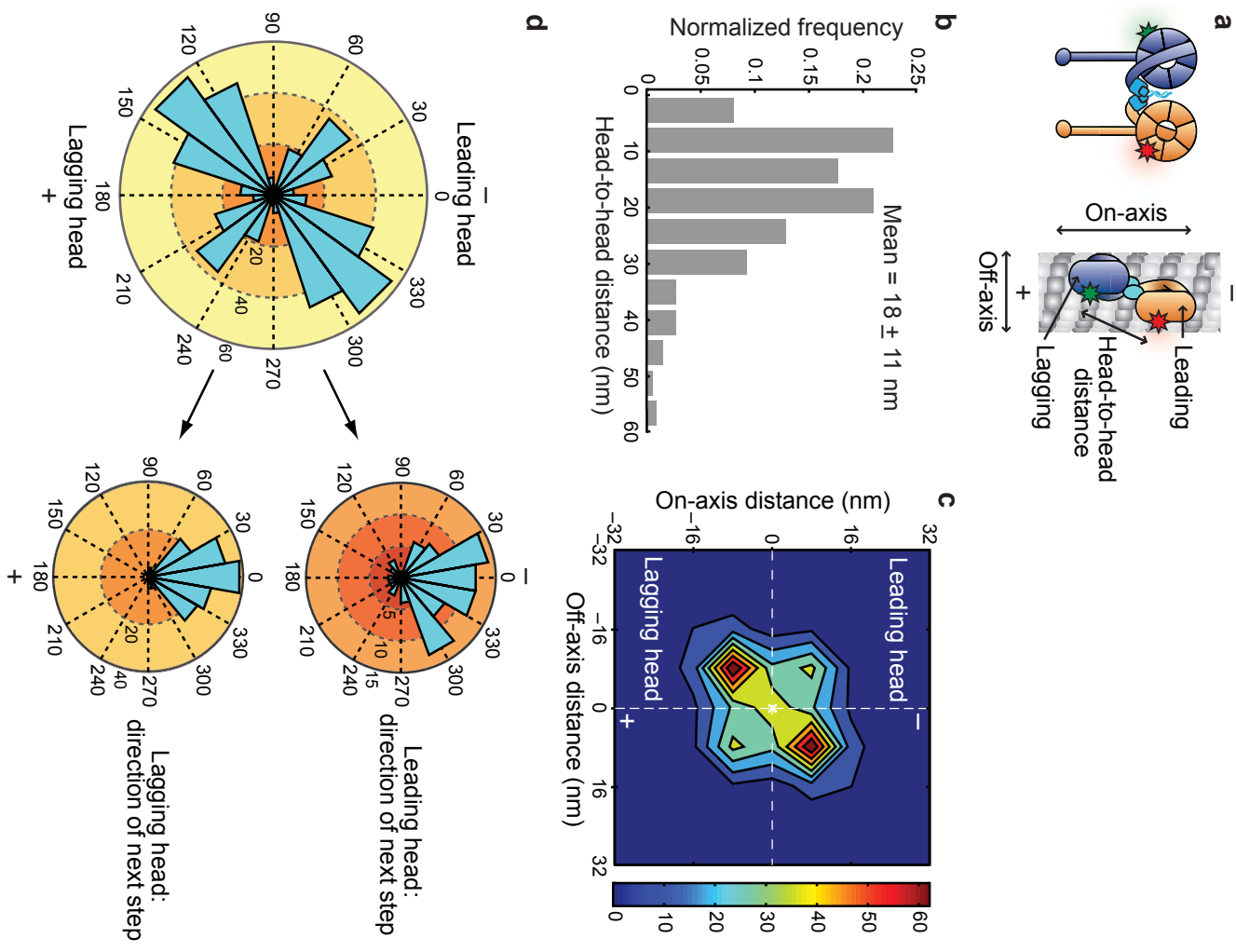


Figure 2.5 Spatial arrangement of dynein motor domains during the two-head-bound state. (a) Schematic of dual-labeled DNA-dimerized dynein bound to a microtubule. Other arrangements of the motor domains are possible. Fluorophores are represented by red and green stars. (b) Histogram of dynein's head-to-head distances during the two-head-bound state. $N = 523$. (c) Contour plot showing the left and right asymmetry between the leading and lagging heads. Orientation of the microtubule axis is vertical, as indicated by – and +, with the centroid position of each dynein molecule placed at the origin of the axes (white X). The number of occurrences of each position is indicated by the color bar on the right, with bin edges at 8-nm increments on both axes. $N = 256$ dimers or 512 heads. (d) Left, angle histogram of the position of the leading and lagging heads of individual dynein dimers relative to their respective centroid position (placed at the origin of the axes). Locations to the left or right of the direction of motion are between 0° and 180° , or 180° and 360° , respectively. $N = 256$ dimers or 512 heads. Right, angular distributions of the next step taken by the leading or lagging head. Steps between 90° and 270° are backward steps.

domains of a dynein dimer do not typically reside on the same protofilament of a microtubule.

Additionally, these findings support the idea that each dynein motor domain maintains a relatively stable identity of being a right leading head or a left lagging head. Although the dynein heads have a distinct left or right identity, the direction of the next step taken by either a leading or lagging head is predominantly forward, with no off-axis bias (Fig. 2.5d), suggesting that dynein's two motor domains typically straddle at least one microtubule protofilament, but then move forward toward the microtubule's minus-end.

The spatial asymmetry between the leading and lagging motor domains suggested that dynein's two heads have distinct identities when microtubule-bound. Additionally, optical trapping studies have shown that dynein responds asymmetrically to rearward and forward forces (22). To determine whether tension played a role in the dynein stepping mechanism, we analyzed the duration of two-head-bound states associated with leading or lagging head stepping events. The mean duration for two-head-bound states terminated by a lagging head stepping is significantly shorter than that of two-head-bound states terminated by a leading head stepping (Fig. 2.6a). We hypothesized that the asymmetric response of leading and lagging heads is due to the difference in direction of the respective force vectors acting upon them along the microtubule axis (forward-directed force for the lagging heads and rearward-directed force for the leading heads).

Since motor domains separated by larger distances may experience increased tension, we examined whether dynein's stepping pattern changed as a function of the head-to-head distance. When the dynein motor domains were close together, we found that there was an equal probability of the leading or lagging head stepping (Fig. 2.6b). However, as the heads became

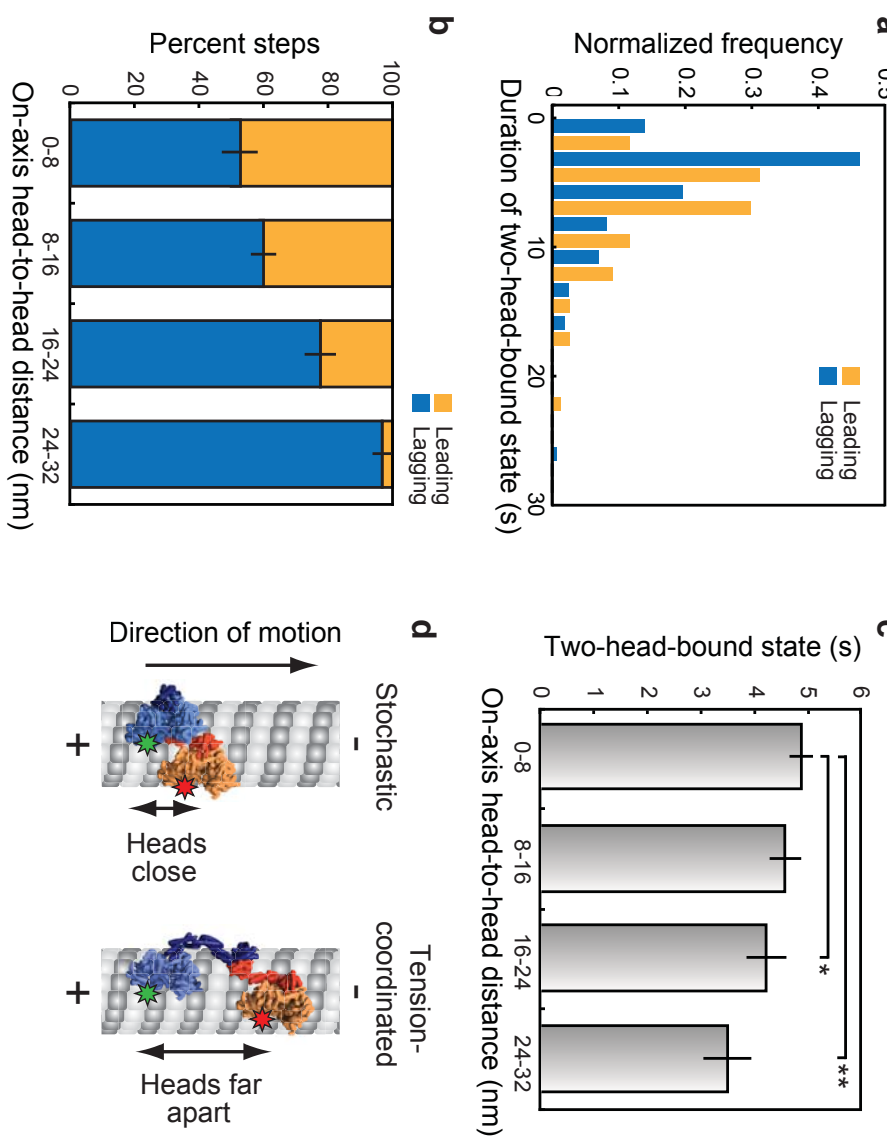
separated by larger distances in the on-axis direction, the lagging head was increasingly more likely to step (Fig. 2.6b). This trend was also observable when we examined the duration of the two-head-bound state as a function of distance between motor domains in the on-axis direction.

As larger distances separated the motor domains, the duration of the two-head-bound state decreased (Fig. 2.6c). Additionally, we found that the direction of the force is important for this effect, as neither the percentage of leading vs. lagging heads stepping, nor the duration of the two-head-bound state varied as a function of the distance between motor domains in the off-axis direction (Fig. A1.5a,b).

Our results suggest that stochastic, uncoordinated stepping dominates when dynein's motor domains are close together, but when dynein's two motor domains are separated by larger distances, stepping becomes increasingly coordinated (Fig. 2.6d). We hypothesize that when large distances separate dynein's two motor domains, the dynein microtubule-binding domain may respond asymmetrically to force in the direction of movement along the microtubule (on-axis), but not across the microtubule (off-axis). This is consistent with reports that dynein responds asymmetrically to forward- and rearward- directed forces (5, 22), as well as studies that demonstrate that dynein's step size is smaller under increased load (4, 22).

By combining two-color, single-molecule microscopy with high-precision, two-dimensional tracking, we have shown that dynein's stepping mechanism is distinct from all cytoskeletal molecular motors characterized to date. Although many of dynein's steps alternate in time, most stepping events do not switch the leading or lagging spatial identities of dynein's two heads, a distinction from the two-headed processive myosin and kinesin motors that use alternating and passing (hand-over-hand) mechanisms. Strikingly, our data suggest that dynein's

Figure 2.6 Dynein steps are stochastic at short head-to-head spacing and coordinated as head-to-head spacing increases. (a) Histograms of the duration of the two-head-bound states that are terminated by a leading-head stepping event or a lagging-head stepping event. (b) Relative stepping frequency of the leading and lagging heads as a function of the on-axis distance between motor domains. Error bars represent the s.e.m. and were generated by bootstrapping each bin. $N = 352$. (c) The duration of the two-head-bound state plotted as a function of the on-axis head-to-head distance. Mean durations \pm s.e.m. are shown (* $P = 0.0139$, ** $P = 0.0094$; two-tailed KS-test, alpha value 0.05, $N = 485$). (d) Model for the dynein stepping mechanism. The three-dimensional structure of dynein (PDB 3QMZ (18)), filtered to 8 Å resolution, was used to generate two microtubule-bound models of dimeric GST-dynein. The dynein rings are shown parallel to the long axis of the microtubule and parallel to each other, based on electron microscopy reconstructions (51–54). Stepping is stochastic when dynein's motor domains are close together (left panel). Large distances between the two motor domains result in a tension-based mechanism that coordinates stepping (right panel).



steps are uncoordinated when the distance between motor domains is small, presumably because the intramolecular strain is low. However, as the distance between motor domains increases, our data show that dynein becomes increasingly coordinated, likely through a tension-based mechanism. These findings demonstrate that dynein is the first two-headed processive cytoskeletal motor that can alternate between stochastic- and tension- based stepping to achieve processivity (Fig. 2.6d).

In addition to tension governing dynein's stepping behavior, the large size of the dynein motor domains (Fig. 2.1c) may impart steric constraints on the stepping pattern. Our data suggest that structural limitations influence the range and location of dynein on the microtubule lattice. We have found that dynein has an inherent left or right asymmetry, with the right motor domain of the dimer more likely to be the leading head and the left motor domain more likely to be the lagging head. It is unlikely that this asymmetry is generated by DNA-based dimerization, as the linkers we have included between dynein and the DNA contain multiple freely rotatable bonds. Therefore, a possible source of asymmetry could be the position of the linker domain, which lies across the face of the AAA+ ring and moves in response to the nucleotide occupancy at AAA1 (10, 12). We propose that the linker domain of the motor on the right is "sandwiched" between the dynein rings, while the linker domain of the motor on the left is not bound by another motor domain, imparting a structural and functional asymmetry (Fig. 2.6d). Our observation of large separations between dynein's two motor domains also suggests that the linker domain can undock from the motor domain (most likely the lagging motor as in Fig. 2.6d, panel 2), as has been observed in electron microscopy studies of both cytoplasmic and axonemal dyneins (10, 12).

The stochastic nature of dynein's stepping behavior raises the intriguing question of how a partially uncoordinated motor achieves processive motility. In the case of kinesin-1, myosin-V and myosin-VI, processivity is accomplished by maintaining the leading head in a strong, filament-bound state until the lagging head detaches from the filament to pass the bound head and becomes the new leading head. Intramolecular tension between the motor domains provides a nucleotide gating mechanism that favors the detachment of the lagging motor domain and promotes a biased, diffusion-based search of this head for the next filament binding site (38-43). For dynein, it is possible that dynein's high duty ratio (21) substantially reduces the likelihood that both motor domains simultaneously dissociate from their microtubule track. This idea is corroborated by recent findings showing that mutant myosin-V and -VI motors are still processive even when their tension-based gating mechanisms are impaired or destroyed (44, 45). However, our data do not rule out the possibility of nucleotide gating for dynein. For example, our finding that 74% of the steps we observed were alternating would be consistent with gating of some steps, as has been suggested by studies of *Dictyostelium* cytoplasmic dynein (46).

The similarity between the motility of the DNA-dynein heterodimer, the GST-dynein homodimer, and native yeast dynein (5, 22) suggests that the basic stepping mechanism will be the same for native dynein and the model systems that are currently being used to study the dynein mechanism. Thus, the DNA-based technique of heterodimer formation that we developed will be a powerful tool for orthogonal control over each dynein protomer for the study of additional heterodimer combinations in the future. However, our data do not rule out the possibility that dynein's native dimerization interface, dynein's associated subunits (intermediate, light intermediate, and light chains), cofactors (dynactin, Lis1, and Nudel), or cargo may impart

an additional layer of regulation on the dynein stepping mechanism. For instance, given that tension appears to coordinate dynein stepping, an interesting area for future study will be to determine if dynein's stepping mechanism becomes coordinated under the load of moving large cargo.

Compared to other cytoskeletal motors, dynein's stepping behavior shows great variability and flexibility. Many dynein steps have an off-axis component, some steps are backwards, and dynein's two motor domains can step independently of each other. We propose that this flexibility allows dynein to navigate a crowded cytoplasm as well as obstacles on microtubules. Our results provide a molecular explanation for the observation that dynein is better able to navigate obstacles than kinesin motors (47, 48).

This apparent plasticity of the dynein stepping mechanism suggests that layers of regulation may be used to accomplish different cell biological functions. In eukaryotic cells, dynein transports dozens, if not hundreds, of different cargo, but there is only a single gene encoding cytoplasmic dynein 1 in all sequenced eukaryotic genomes (with the exception of flowering plants and some algae, which lack dynein genes (49, 50)). Given the variability of the type, size, and loads imparted by different cargo (ranging from endosomes to the mitotic spindle), a number of mechanisms for regulating cytoplasmic dynein's stepping behavior may have evolved. Future studies on the function of dynein-associated subunits and cofactors, the effects of cargo load on motility, as well as how multiple motors may coordinate to move cargo, will determine whether this partially uncoordinated motor is regulated to step coordinately for some functions.

Methods

Yeast strains

Modification of the endogenous *S. cerevisiae* dynein heavy chain gene was accomplished by insertion of the *K. lactis* URA3 selectable marker into the DYN1 gene at the location of the desired change. The *K. lactis* URA3 gene was subsequently replaced with the SNAP-tag, SNAPf-tag (New England Biolabs), HaloTag (Promega), or GFP. Yeast strains used in this study are listed in Table A1.1.

Preparation of HaloTag ligand-fluorophores

HaloTag ligand-fluorophore conjugates not commercially available were prepared as follows. Atto647N was conjugated to the HaloTag ligand by mixing 10 mM Atto647N NHS ester (Atto-Tec), 20 mM HaloTag amine (O4) Ligand (Promega), and 30 mM N,N-diisopropylethylamine in dimethylformamide, and nutating at 30°C for 24 hrs. The HaloTag-Atto647N conjugate was separated from unreacted material by HPLC using a reverse-phase C18 column with a methanol:water gradient. Final product purity was >85% as assessed by mass spectrometry. Cy3B-Halotag was prepared by Bio-synthesis, Inc (Lewisville, TX) from Cy3B-NHS (GE Healthcare Lifesciences) and HaloTag amine (O4) ligand (Promega).

Benzylguanine-conjugated DNA oligonucleotides

Benzylguanine-conjugated DNA oligonucleotides (BG-oligos) were prepared by mixing 10 mM BG-GLA-NHS (New England Biolabs) in anhydrous DMSO with 0.33 mM PAGE-purified amine-functionalized oligos (Bioneer) in 67 mM HEPES (pH 8.5) and 50% DMSO (v/v) for 30

min at room temperature. Unreacted BG-GLA-NHS was removed using Micro Bio-Spin 6 Columns (Bio-Rad), pre-equilibrated with 10 mM Tris (pH 8.0), 150 mM KCl, and 10% (v/v) glycerol. Linkage of BG to oligos was confirmed by gel shift assays on 20% TBE gels (Invitrogen). Oligo sequences used for dynein dimerization are listed in Table A1.2.

Protein purification and labeling

Dynein motors were purified as described previously (5) with modifications detailed below. Motors were labeled with BG-oligos and HaloTag ligand-fluorophores during dynein purification. Oligo sequences used for labeling dynein and dynein monomers used in different experiments are listed in Tables A1.2 and A1.3, respectively.

TIRF microscopy

Motility assays were performed using an inverted objective type Olympus IX-81 TIRF microscope with a 100X 1.45 N.A. oil immersion TIRF objective (Olympus) equipped with four CW diode-pumped solid state lasers: 405 nm and 640 nm cubic lasers (Coherent Inc.) and 491 nm and 561 nm lasers (Cobolt). Signals were detected with a back-thinned electron multiplier CCD camera (Hamamatsu). For near-simultaneous, two-color imaging, the microscope was modified to include a dual-band laser polychroic mirror (z561/635rpc, Chroma) and a dual-band sputtered emission filter (etCy3/Cy5m, Chroma) in the main optical path. The excitation path of the 561 nm laser was controlled by an acousto-optical tunable filter (NEOS; response time of 10 ms), while that of the 640 nm laser was controlled by a fast mechanical shutter (SmartShutter, Sutter Inc.; response time of 25 ms).

Protein purification and labeling

Dynein motors were purified as described previously (5) with the following modifications. Labeling reactions were performed during the purification, when the motors were bound via the N-terminal ZZ-tag to IgG sepharose beads (GE Lifesciences). GST-based dynein dimers were labeled with either 1 mM Halo-TMR (Promega) or 1 mM Halo-biotin (Promega) in TEV cleavage buffer (10 mM Tris (pH 8.0), 150 mM KCl, 10% (v/v) Glycerol, 1 mM DTT, 0.1 mM Mg-ATP and 0.5 mM PMSF) for 10 min at room temperature. Dynein monomers for subsequent dimerization with DNA were labeled with 20 μ M BG-oligo with or without 2 μ M Halotag-fluorophore in TEV cleavage buffer for 30 min at room temperature. After dynein labeling, the beads were washed an additional 4 times with TEV cleavage buffer to remove unbound BG-oligos and HaloTag ligand-fluorophores. The purification was then completed as previously described (5). The oligomer sequences used for labeling and the pairs of dynein protomers used for different experiments are listed in Tables A1.2 and A1.3.

Formation of dynein heterodimers was detected using a PAGE gel shift assay that did not denature the duplex DNA. Dynein solutions with complementary oligos were mixed and incubated on ice for 15 min and then mixed with LDS sample buffer (Invitrogen) and separated on 3-8% tris-acetate gels (Invitrogen). Dynein was visualized with either SYPRO red protein stain, GFP fluorescence (present on the tail domain of all dynein constructs), or the covalently linked HaloTag fluorophores. Typically, 65% (SNAP-tag) or 90% (SNAPf-tag) of the dynein protomers formed heterodimers. The only difference between these tags is the kinetics of the SNAP-tag ligation to its BG substrate. The much higher heterodimer formation achieved with the

SNAPf-tag allows us to conclude that the yield of DNA-based dimerization is limited by the efficiency of linking SNAP-tagged monomers to BG-oligos, not by the efficiency of DNA hybridization. To minimize protein degradation, we chose to use short labeling times that resulted in incomplete oligo labeling of SNAP-tagged dynein monomers.

For the run length and velocity assays, inactive motors that could bind MTs, but not release, were removed by a MT affinity step in the presence of MgATP. Dynein was mixed with 0.1 volumes of 60 μ M taxol-stabilized MTs and 0.2 volumes 5X TEV cleavage buffer supplemented with 50 μ M taxol and incubated at room temperature for 10 min. The mixture was centrifuged at 108,000 \times g for 15 min at room temperature. The dynein-containing supernatant was aliquoted, snap frozen in liquid nitrogen, and stored at -80°C.

Single molecule run length and velocity assays

Flow chambers were made by attaching a coverslip to a glass slide by double-sided tape. The flow chamber was then incubated with one chamber volume (~10 μ l) of 1mg/ml biotin-BSA in BRB80 (80 mM PIPES (pH 6.8), 2 mM MgCl₂, and 1 mM EGTA) for 2 min at room temperature. Unbound free biotin-BSA was removed by washing the chamber with 4 chamber volumes of BRB80. The chamber was next perfused with 20 μ l of 0.5 mg/ml streptavidin in BRB80 and incubated at room temperature for 2 min to allow for biotin/streptavidin interactions, washed with 4 chamber volumes of dynein lysis buffer (1X dynein lysis buffer: 30 mM HEPES (pH 7.2), 50 mM KAcetate, 2 mM MgAcetate, 1 mM EGTA, 10% (v/v) glycerol, 1 mM DTT, 0.1 mM Mg-ATP and 0.5 mM PMSF) supplemented with 20 μ M taxol, but lacking ATP and PMSF, to remove excessive unbound streptavidin, and incubated with 10 μ l taxol-stabilized

bovine MTs (containing 10% Hilyte Fluor 488 (Cytoskeleton Inc.) labeled tubulin, and 10% biotinylated tubulin (Cytoskeleton Inc.)) at room temperature for 2 min. Finally, the chamber was perfused with dynein motors diluted in dynein motility buffer (30 mM HEPES pH 7.2, 50 mM KAcetate, 2 mM MgAcetate, 1 mM EGTA, 10% (v) glycerol, 1 mM DTT, 1 mM MgATP, 1.25 mg/ml casein and 20 μ M taxol) and supplemented with an oxygen scavenger system as previously described (5). The sample was alternatively excited with the 561 nm laser and 640 nm laser. Interspersed time-lapse image sequences were acquired at 1 frame/ 2 sec with an exposure time of 100 ms (typically for 10 min). Kymographs were generated and analyzed in ImageJ. Only those runs that were visible in both color channels were scored to ensure that all data came from dual labeled dynein heterodimers.

Calibration of the TIRF microscope for high precision experiments

Three different fluorophores (Qdots655, Cy3B and Atto647N) were used for high-precision measurements in this study. For each fluorophore, we determined the localization precision achievable under typical experimental conditions. We first immobilized the fluorophore on a coverslip, and moved the coverslip in a staircase pattern of precise increments (6 nm for Qdots655 and 16 nm for both Cy3B and Atto647N) using a piezo nanostage (MadCity Labs). Between stage movements, multiple images were taken using laser powers and exposure times identical to experimental conditions. The point-spread function of individual fluorophores were then fit with a 2-D Gaussian to determine their centroid position (36), and the average positions of the fluorophores between stage movements were determined by a custom MATLAB program (see below). To estimate the localization precision, we next computed the difference between the

raw centroid positions and the average positions from the step-finding program (Fig. A1.1a-c).

One-color high precision motility assays

All one-color high precision motility assays were performed with dynein singly-labeled via a N- or C-terminal HaloTag with a Qdot 655 (Invitrogen) on sea urchin axonemes (55) at room temperature. Previously, we observed that the large (15-20 nm) diameter of Invitrogen's Qdot 655 allowed labeling of only one motor domain within the dynein GST-dimer (even though both motors contained a labeling site), suggesting one site is sterically blocked (5). The flow chamber was first incubated with one chamber volume of axonemes in BRB12 (12 mM PIPES at pH 6.8, 2 mM MgCl₂ and 1 mM EGTA) for 2 min to allow axonemes to adhere to the coverslip, and was washed with 10 chamber volumes of BRB12 to remove unbound axonemes. The chamber was then washed with 1X dynein lysis buffer, incubated with 10 µl of biotinylated dynein molecules in the absence of ATP for 2 min, washed with 10 chamber volumes of dynein motility buffer to remove unbound dynein molecules, and incubated with 50 nM Qdot 655 streptavidin (Invitrogen). The labeling reaction was performed with dynein sparsely immobilized on axonemes to prevent biotinylated dynein molecules from aggregating on the streptavidin coated Qdots. High precision stepping experiments were performed in dynein motility buffer with 10 mM β-mercaptoethanol (in place of DTT) and 4-6 µM Mg-ATP (in place of 1mM ATP), supplemented with an ATP regeneration system (10 mg/ml pyruvate kinase and 10 mM phosphoenolpyruvate) and an oxygen scavenger system (5). The sample was excited with the 405 nm laser at ~5 mW. Time-lapse image sequences were stream acquired with 100 ms exposure time for 40-50 s. Fluorescent spots in the original images were then fit with a 2-D Gaussian to

precisely localize their position (36). Steps (1-D and 2-D) were determined by a custom MATLAB program (see below).

Two-color motility assays

For all two-color high precision experiments, we used DNA-based dynein heterodimers formed from two complimentary DNA-linked dynein protomers labeled with Halo-Cy3B and Halo-Atto647N at the C terminus. Sample slides were prepared as described above for the two-color run length and velocity assays with the following modifications: (1) Stepping experiments were performed using unlabeled (instead of fluorescent) taxol-stabilized MTs to minimize crosstalk between fluorophores. (2) The chambers were incubated with dynein motors in the absence of ATP for 2 min before an extensive wash with 5 chamber volumes of motility buffer lacking ATP to remove unbound dynein molecules. (3) Stepping experiments were performed in a dynein motility buffer lacking 50 mM KAcetate, supplemented with 500nM ATP (instead of 1 mM ATP) and 2 mM Trolox (which improved the photostability of both Cy3B and Atto647N; instead of 10 mM β -mercaptoethanol). The sample was alternatively excited with the 561 nm and 640 nm lasers (the power for each was ~10 mW at the objective), and interspersed time-lapse image sequences were stream acquired at an exposure time of 600 ms for a total duration of 2-3 min.

A custom MATLAB (The MathWorks, Natick, MA) program was used to screen for dual-labeled dynein molecules from the raw two-color image sequences. Dual-labeled dynein molecules were tracked with a 2-D Gaussian function to precisely localize their centroid locations in both the Cy3B and Atto647N channels throughout the image sequence. The resulting stepping traces (x-y coordinates of dynein's centroid positions) and the corresponding

fluorescence intensity profiles were then plotted independently for the Cy3B and Atto647N channels. At this point the data from each channel was visually inspected and traces were discarded for the following reasons: (a) If the stepping dwell clusters were not clearly defined. (b) If the fluorescence intensity was too low to yield high precision localization. (c) If the observable step sizes were much larger than the known dynein step size distribution (indicating missed steps). (d) If multiple-step photobleaching was observed based on the fluorescence intensity profile (indicating the presence of more than 1 dye per dynein head).

Two color stepping traces that passed the screening process were next precisely localized using an alignment procedure described previously (37). Briefly, we created an alignment grid surrounding each candidate two-color trace pairs by immobilizing a 0.2 μ m tetraspeck bead (Invitrogen) on a coverslip and moving it in a grid pattern (2.2 μ m X 2.2 μ m with a spacing of 200 nm) with a piezo nanostage (Madcity Labs). Fiducial data was acquired in both imaging channels at each grid point. This mapping method yielded a mean accuracy of ~4 nm as determined by the target registration error (37). We validated the alignment method by precisely aligning the positions of a tetraspeck bead determined from the two imaging channels (Fig. A1.3a,b). Aligned candidate two-color traces were next analyzed using a custom MATLAB 2-D stepping program (see below) to determine steps in 1-D and 2-D. Steps were discarded at this stage if a stretch (more than three) of dwell-clusters could not be identified in both channels. The remaining two-color stepping traces were further processed with the temporal and spatial analysis. Our dwell and step analyses only included trace regions where we could confidently define the spatial and temporal relationships between the Cy3B and Atto647N channels.

Two-dimensional step-finding algorithm

To determine dynein's step size and dwell time (the length of pausing between steps), we used an extended Chung-Kennedy edge-detecting algorithm (56) specifically designed for analyzing noisy time series (57). This algorithm uses running averages in the forward and backward directions, as well as the estimated noise of the trace, to calculate a probability function for the presence or absence of steps at a given point in time. A threshold is then suggested for statistically assigning steps. We implemented this filter in an automated step-detecting program in MATLAB, with parameters suggested by Smith et al (57). In order to detect steps, a stepping trace (or a two-color stepping trace pair) was first analyzed using principal component analysis and the direction of longer variance of the trace, which corresponds to the principal axis of motion, was aligned to the X-axis. Subsequently, the edge detector algorithm was independently applied to the X (on-axis) and Y (off-axis) components of the trace to find a stepping pattern in each direction. Steps were called when they had a component of either ≥ 4 nm on-axis (half the size of a tubulin dimer), ≥ 5 nm off-axis (the separation between two adjacent tubulin protofilaments), or both.

The suitability of this step-finding method was assessed by comparing the stepping statistics of Cy3B- and Atto647N- labeled dynein heads with that of the less noisy Qdot-655 labeled dynein head. Even with the lower precision of the organic fluorophore data, both the on- and off-axis step size distributions of the Cy3B- and Atto647- labeled heads were similar to the stepping statistics of the much brighter Qdot-655 labeled dynein head, suggesting that our step assignments for the two-color data are accurate.

Stepping and dwell analysis

A custom MATLAB program was used to analyze the data of fitted X and Y positions determined by the step finding program. The program used the following criteria to perform independent spatial and temporal analyses on the steps and allow for correlation analysis. For the heads to be called as leading, lagging, or uncertain, the on-axis positions of the two heads are compared using a two-sample t-test with a confidence level of 95%. The same spatial analysis was applied to the off-axis direction to call heads left, right, or uncertain. A passing step was defined as a switch in on-axis position (e.g. a leading head became a lagging head) while a not-passing step maintained the relative on-axis position of the two heads. If the relative position of the heads before or after a step was uncertain, the step was not called as passing or not passing. The same analysis was applied in the off-axis direction to determine whether the heads crossed from left to right.

For steps to be analyzed as alternating or not alternating, they had to be clearly resolvable in the time domain. Sequential steps were considered for this analysis only if both the step in question and the previous step were sufficiently resolvable in time. We defined a step as resolvable in time if it was at least one frame away from a step in the other channel. The head-to-head distance was calculated for all positions where the heads remained stationary for at least 3 points of overlap (two points in one channel and one point in the other). This was calculated in both the X and Y directions as the difference between the Cy3B and Atto647N positions.

The 2-D head-to-head distance and step size were calculated by measuring the magnitude of the vector composed of the on- and off- axis components.

Histograms

For all histograms with 1 variable, the bin width was determined using Scott's rule (58). For all histograms with 2 variables, the bin width was determined using Scott's rule on one variable as indicated in figure legends. For ease of visually comparing the two variables, the width of each variable's bar is 40% of the total bin width and the first variable is plotted in a position that is located at the bin center -0.25*bin width, while the second variable is plotted in a position that is located at the bin center +0.25*bin width.

Acknowledgements

We thank X. Su and D. Pellman (Harvard Medical School) for providing purified kinesin-8; S. Zou for technical assistance; A. Carter, S. Churchman, A. Gennrich, Y. Goldman, A. Hendricks, J. Huang, A. Leschziner and A. Roberts for critical comments on the manuscript; F. Aguet, A. Besser, M. Vilela and G. Danuser for discussions of data analysis; M. Bagonis for early work on oligomer-SNAP linking; A. Leschziner for help with figure design; and A. Carter for providing MATLAB code. W.Q. is supported by a postdoctoral fellowship from the American Heart Association. S.L.R.-P. is funded by the Rita Allen Foundation, the Harvard Armenian Foundation and a US National Institutes of Health New Innovator award (1 DP2 OD004268-01).

References

1. J. Eschbach, L. Dupuis, Cytoplasmic dynein in neurodegeneration, *Pharmacol Ther* **130**, 348–363 (2011).
2. A. Wynshaw-Boris, Lissencephaly and LIS1: insights into the molecular mechanisms of neuronal migration and development, *Clin Genet* **72**, 296–304 (2007).
3. S. J. King, T. A. Schroer, Dynactin increases the processivity of the cytoplasmic dynein motor, *Nat Cell Biol* **2**, 20–24 (2000).
4. R. Mallik, B. C. Carter, S. A. Lex, S. J. King, S. P. Gross, Cytoplasmic dynein functions as a gear in response to load, *Nature* **427**, 649–652 (2004).
5. S. L. Reck-Peterson *et al.*, Single-Molecule Analysis of Dynein Processivity and Stepping Behavior, *Cell* **126**, 335–348 (2006).
6. J. L. Ross, K. Wallace, H. Shuman, Y. E. Goldman, E. L. Holzbaur, Processive bidirectional motion of dynein-dynactin complexes in vitro, *Nat Cell Biol* **8**, 562–570 (2006).
7. S. Toba, T. M. Watanabe, L. Yamaguchi-Okimoto, Y. Y. Toyoshima, H. Higuchi, Overlapping hand-over-hand mechanism of single molecular motility of cytoplasmic dynein, *Proc Natl Acad Sci USA* **103**, 5741–5745 (2006).
8. Z. Wang, S. Khan, M. P. Sheetz, Single cytoplasmic dynein molecule movements: characterization and comparison with kinesin, *Biophysical Journal* **69**, 2011–2023 (1995).
9. J. R. Kardon, R. D. Vale, Regulators of the cytoplasmic dynein motor, *Nat Rev Mol Cell Biol* **10**, 854–865 (2009).
10. S. A. Burgess, M. L. Walker, H. Sakakibara, P. J. Knight, K. Oiwa, Dynein structure and power stroke, *Nature* **421**, 715–718 (2003).
11. T. Kon *et al.*, Helix sliding in the stalk coiled coil of dynein couples ATPase and microtubule binding, *Nat Struct Mol Biol* **16**, 325–333 (2009).
12. A. J. Roberts *et al.*, AAA+ Ring and linker swing mechanism in the dynein motor, *Cell* **136**, 485–495 (2009).
13. R. D. Vale *et al.*, Direct observation of single kinesin molecules moving along microtubules, *Nature* **380**, 451–453 (1996).
14. I. R. Gibbons *et al.*, Photosensitized cleavage of dynein heavy chains. Cleavage at the “V1 site” by irradiation at 365 nm in the presence of ATP and vanadate, *J. Biol. Chem.* **262**, 2780–2786 (1987).

15. C. Cho, S. L. Reck-Peterson, R. D. Vale, Regulatory ATPase sites of cytoplasmic dynein affect processivity and force generation, *J. Biol. Chem.* **283**, 25839–25845 (2008).
16. T. Kon, M. Nishiura, R. Ohkura, Y. Y. Toyoshima, K. Sutoh, Distinct Functions of Nucleotide-Binding/Hydrolysis Sites in the Four AAA Modules of Cytoplasmic Dynein †, *Biochemistry* **43**, 11266–11274 (2004).
17. A. Silivanovich, M. G. Li, M. Serr, S. Mische, T. S. Hays, The third P-loop domain in cytoplasmic dynein heavy chain is essential for dynein motor function and ATP-sensitive microtubule binding, *Mol. Biol. Cell* **14**, 1355–1365 (2003).
18. A. P. Carter, C. Cho, L. Jin, R. D. Vale, Crystal structure of the dynein motor domain, *Science (New York, N.Y.)* **331**, 1159–1165 (2011).
19. A. P. Carter *et al.*, Structure and functional role of dynein's microtubule-binding domain, *Science (New York, N.Y.)* **322**, 1691–1695 (2008).
20. T. Kon, K. Sutoh, G. Kurisu, X-ray structure of a functional full-length dynein motor domain, *Nat Struct Mol Biol* **18**, 638–642 (2011).
21. T. Shima, K. Imamula, T. Kon, R. Ohkura, K. Sutoh, Head-head coordination is required for the processive motion of cytoplasmic dynein, an AAA+ molecular motor, *J. Struct. Biol.* **156**, 182–189 (2006).
22. A. Gemnerich, A. P. Carter, S. L. Reck-Peterson, R. D. Vale, Force-Induced Bidirectional Stepping of Cytoplasmic Dynein, *Cell* **131**, 952–965 (2007).
23. A. Gemnerich, R. D. Vale, Walking the walk: how kinesin and dynein coordinate their steps, *Current Opinion in Cell Biology* **21**, 59–67 (2009).
24. J. R. Sellers, C. Veigel, Walking with myosin V, *Curr Opin Cell Biol* **18**, 68–73 (2006).
25. H. L. Sweeney, A. Houdusse, Myosin VI rewrites the rules for myosin motors, *Cell* **141**, 573–582 (2010).
26. A. Yildiz, Myosin V Walks Hand-Over-Hand: Single Fluorophore Imaging with 1.5-nm Localization, *Science (New York, N.Y.)* **300**, 2061–2065 (2003).
27. A. Yildiz, M. Tomishige, R. D. Vale, P. R. Selvin, Kinesin walks hand-over-hand, *Science (New York, N.Y.)* **303**, 676–678 (2004).
28. M. Samso, M. P. Koonce, 25 Angstrom resolution structure of a cytoplasmic dynein motor reveals a seven-member planar ring, *J. Mol. Biol.* **340**, 1059–1072 (2004).
29. X. Su *et al.*, Mechanisms underlying the dual-mode regulation of microtubule dynamics by Kip3/kinesin8, *Mol Cell* **43**, 751–763 (2011).

30. S. Ray, S. G. Wolf, J. Howard, K. H. Downing, Kinesin does not support the motility of zinc-macrotubes, *Cell Motil Cytoskeleton* **30**, 146–152 (1995).
31. S. Ray, E. Meyhofer, R. A. Milligan, J. Howard, Kinesin follows the microtubule's protofilament axis, *J. Cell Biol.* **121**, 1083–1093 (1993).
32. L. A. Banaszynski, C. W. Liu, T. J. Wandless, Characterization of the FKBP:rapamycin:FRB ternary complex, *J. Am. Chem. Soc.* **127**, 4715–4721 (2005).
33. N. R. Markham, M. Zuker, DiNA-Melt web server for nucleic acid melting prediction, *Nucleic Acids Research* **33**, W577–81 (2005).
34. Y. Miyazono, M. Hayashi, P. Karagiannis, Y. Harada, H. Tadakuma, Strain through the neck linker ensures processive runs: a DNA-kinesin hybrid nanomachine study, *EMBO J.* **29**, 93–106 (2010).
35. B. Essevaz-Roulet, U. Bockelmann, F. Heslot, Mechanical separation of the complementary strands of DNA, *Proc. Natl. Acad. Sci. U.S.A.* **94**, 11935–11940 (1997).
36. R. E. Thompson, D. R. Larson, W. W. Webb, Precise nanometer localization analysis for individual fluorescent probes, *Biophys J* **82**, 2775–2783 (2002).
37. L. S. Churchman, Z. Okten, R. S. Rock, J. F. Dawson, J. A. Spudich, Single molecule high-resolution colocalization of Cy3 and Cy5 attached to macromolecules measures intramolecular distances through time, *Proc. Natl. Acad. Sci. U.S.A.* **102**, 1419–1423 (2005).
38. A. Yildiz, M. Tomishige, A. Gennerich, R. D. Vale, Intramolecular Strain Coordinates Kinesin Stepping Behavior along Microtubules, *Cell* **134**, 1030–1041 (2008).
39. S. S. Rosenfeld, H. L. Sweeney, A model of myosin V processivity, *J. Biol. Chem.* **279**, 40100–40111 (2004).
40. T. J. Purcell, H. L. Sweeney, J. A. Spudich, A force-dependent state controls the coordination of processive myosin V, *Proc. Natl. Acad. Sci. U.S.A.* **102**, 13873–13878 (2005).
41. C. Veigel, S. Schmitz, F. Wang, J. R. Sellers, Load-dependent kinetics of myosin-V can explain its high processivity, *Nat Cell Biol* **7**, 861–869 (2005).
42. H. L. Sweeney *et al.*, How myosin VI coordinates its heads during processive movement, *EMBO J.* **26**, 2682–2692 (2007).
43. A. R. Dunn, P. Chuan, Z. Bryant, J. A. Spudich, Contribution of the myosin VI tail domain to processive stepping and intramolecular tension sensing, *Proc. Natl. Acad. Sci. U.S.A.* **107**, 7746–7750 (2010).

44. T. G. Baboolal *et al.*, The SAH domain extends the functional length of the myosin lever, *Proc. Natl. Acad. Sci. U.S.A.* **106**, 22193–22198 (2009).
45. M. W. Elting, Z. Bryant, J. C. Liao, J. A. Spudich, Detailed tuning of structure and intramolecular communication are dispensable for processive motion of myosin VI, *Biophys. J.* **100**, 430–439 (2011).
46. N. Numata, T. Shima, R. Ohkura, T. Kon, K. Sutoh, C-sequence of the Dictyostelium cytoplasmic dynein participates in processivity modulation, *FEBS Lett.* **585**, 1185–1190 (2011).
47. R. Dixit, J. L. Ross, Y. E. Goldman, E. L. Holzbaur, Differential regulation of dynein and kinesin motor proteins by tau, *Science (New York, N.Y.)* **319**, 1086–1089 (2008).
48. J. L. Ross, H. Shuman, E. L. Holzbaur, Y. E. Goldman, Kinesin and dynein-dynactin at intersecting microtubules: motor density affects dynein function, *Biophys. J.* **94**, 3115–3125 (2008).
49. C. J. Lawrence, N. R. Morris, R. B. Meagher, R. K. Dawe, Dyneins have run their course in plant lineage, *Traffic* **2**, 362–363 (2001).
50. B. Wickstead, K. Gull, Dyneins across eukaryotes: a comparative genomic analysis, *Traffic* **8**, 1708–1721 (2007).
51. T. Ishikawa, H. Sakakibara, K. Oiwa, The architecture of outer dynein arms in situ, *J. Mol. Biol.* **368**, 1249–1258 (2007).
52. N. Mizuno, A. Narita, T. Kon, K. Sutoh, M. Kikkawa, Three-dimensional structure of cytoplasmic dynein bound to microtubules, *Proc. Natl. Acad. Sci. U.S.A.* **104**, 20832–20837 (2007).
53. D. Nicastro *et al.*, The molecular architecture of axonemes revealed by cryoelectron tomography, *Science (New York, N.Y.)* **313**, 944–948 (2006).
54. H. Ueno, T. Yasunaga, C. Shingyoji, K. Hirose, Dynein pulls microtubules without rotating its stalk, *Proc. Natl. Acad. Sci. U.S.A.* **105**, 19702–19707 (2008).
55. C. M. Waterman-Storer, *Microtubule/Organelle Motility Assays* (John Wiley & Sons, Inc., Hoboken, NJ, USA, 2001).
56. S. H. Chung, R. A. Kennedy, Forward-backward non-linear filtering technique for extracting small biological signals from noise, *J. Neurosci. Methods* **40**, 71–86 (1991).
57. D. A. Smith, A quantitative method for the detection of edges in noisy time-series, *Philos. Trans. R. Soc. Lond., B, Biol. Sci.* **353**, 1969–1981 (1998).
58. D. W. Scott, On optimal and data-based histograms, *Biometrika* **66**, 605–610 (1979).

Chapter 3

Tug of War in Motor Protein Ensembles Revealed with a Programmable DNA Origami Scaffold

Nathan D. Derr, Brian S. Goodman, Ralf Jungmann,

Andres E. Leschziner, William M. Shih, and Samara L. Reck-Peterson

Contributions

Nathan Derr and Brian Goodman contributed equally. Nathan Derr initiated the project. Nathan Derr and Brian Goodman designed the experiments and performed all biochemistry, sample preparation, DNA origami folding, and single molecule motility experiments. Ralf Jungmann performed the DNA-PAINT experiment. Andres Leschziner performed the TEM experiment. William Shih designed the DNA origami chassis. William Shih and Samara Reck-Peterson provided mentorship. This work was published in: Tug-of-war in motor protein ensembles revealed with a programmable DNA origami scaffold, *Science (New York, N.Y.)* **338**, 662–665 (2012).

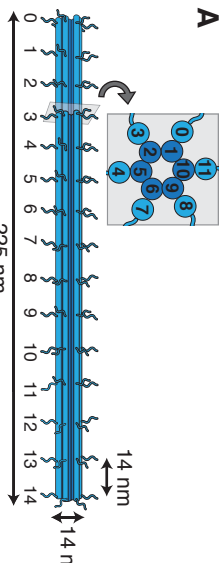
Abstract

Cyttoplasmic dynein and kinesin-1 are microtubule-based motors with opposite polarity that transport a wide variety of cargo in eukaryotic cells. Many cellular cargos demonstrate bidirectional movement due to the presence of ensembles of dynein and kinesin, but are ultimately sorted with spatial and temporal precision. To investigate the mechanisms that coordinate motor ensemble behavior, we built a programmable synthetic cargo using three-dimensional DNA origami to which varying numbers of DNA oligonucleotide-linked motors could be attached, allowing for control of motor type, number, spacing, and orientation *in vitro*. In ensembles of one to seven identical-polarity motors, motor number had minimal effect on directional velocity, whereas ensembles of opposite-polarity motors engaged in a tug-of-war resolvable by disengaging one motor species.

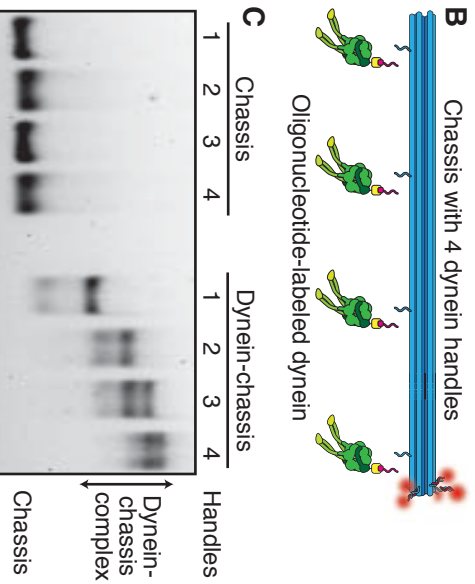
Results

Cyttoplasmic dynein and kinesin-1 (referred to as “dynein” and “kinesin” here) are opposite-polarity, microtubule-based motors responsible for producing and maintaining subcellular organization via the transport of many cargos in eukaryotic cells (1, 2). Defects in these transport processes have been linked to neurological diseases (1, 3, 4). Microtubules contain inherent structural polarity, polymerizing rapidly at their “plus” end and more slowly at their “minus” end (5), with dynein and kinesin driving most minus- and plus-end-directed microtubule transport, respectively (2). Although some transport tasks require a single motor type, many cargos use both dynein and kinesin and move bidirectionally on microtubules (1, 6, 7). The mechanisms that allow ensembles of identical-polarity motors to coordinate their activity and ensembles of opposite-polarity motors to achieve both processive movement and rapid switches in direction are unknown.

To dissect the biophysical mechanisms of motor-driven cargo transport, we designed a programmable, synthetic cargo using three-dimensional DNA origami (8, 9). The cargo consisted of a twelve-helix bundle with six inner and six outer helices (Fig. 3.1A, and Fig. A2.1) (10). We refer to this structure as a “chassis,” akin to an automobile chassis that serves as a skeletal frame for the attachment of additional components. The origami chassis was made by rapidly heating and slowly cooling an 8064-nucleotide, single-strand DNA “scaffold” in the presence of 273 short, single-strand DNA “staples” (Fig. A2.1A, and tables A2.1 to A2.3), which hybridize with discontinuous regions of the scaffold to fold it into a desired shape. Selective inclusion of staples with extra “handle” sequences that project out from the chassis provide site and sequence specific attachment points for motors, fluorophores, or other chemical moieties (Fig. 3.1B).



Next, we purified well-characterized model dynein and kinesin motors and covalently linked them to DNA oligonucleotide “anti-handles” complementary to the handle sequences on the chassis. We used a minimal dimeric *S. cerevisiae* dynein (*II*, *I2*) and a minimal dimeric human kinesin-1 (*I3*), both of which contained a SNAP-tag at their cargo-binding domain for oligonucleotide anti-handle attachment.



kinesin-1 (*I3*), both of which contained a SNAP-tag at their cargo-binding domain for oligonucleotide anti-handle attachment.

We next assessed motor-chassis complex assembly. Gel shift assays of dynein chassis

indicated an ~80% probability for individual dynein occupancy at each motor site on the

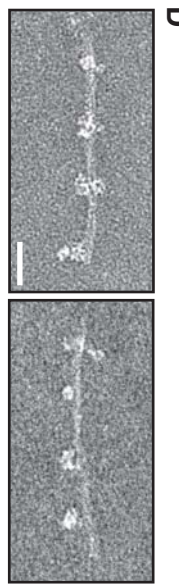


Figure 3.1. Design and validation of a three-dimensional DNA origami synthetic cargo.

(A) Schematic of the twelve-helix bundle chassis structure with 6 inner and 6 outer helices. Each outer helix contains up to 15 optional handles, yielding 90 uniquely addressable sites. Each handle consists of an unpaired 21-bp (~7 nm) oligonucleotide sequence for hybridization to complementary anti-handle sequences covalently attached to motors or fluorophores. Inset shows an orthogonal cross-section. (B) Schematic of a chassis labeled with 5 fluorophores (red) at handle position 14 on each of 5 outer helices and dynein handles at positions 1, 5, 9, and 13 on a single outer helix. Oligonucleotide-labeled dynein is also shown. (C) Agarose gel shift assay of TAMRA-labeled chassis containing 1–4 handles in the absence (left lanes) or presence (right lanes) of dynein labeled with an anti-handle oligonucleotide. Chassis are visualized by TAMRA fluorescence. See Fig. A2.2B for occupancy quantification. (D) Negative-stain TEM images of the 4 dynein-chassis complex. Scale bar, 40 nm.

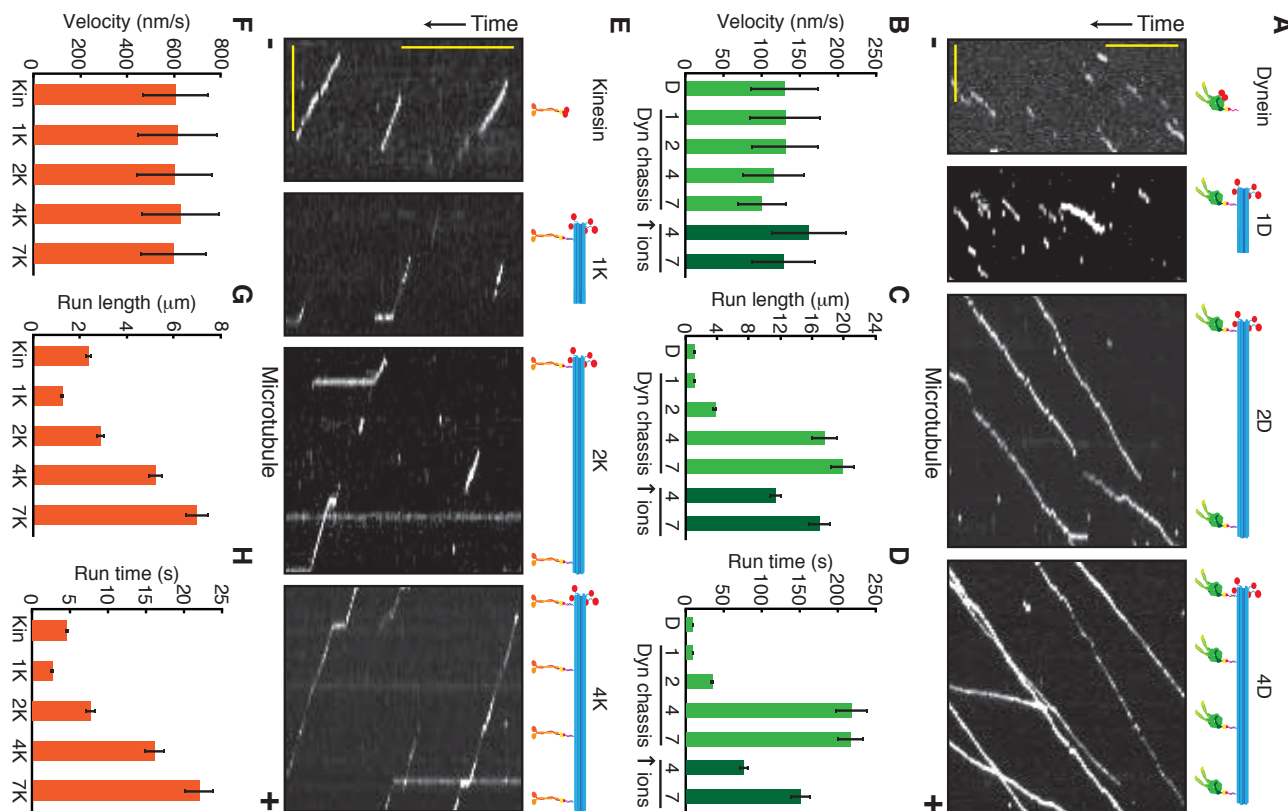
chassis (Fig. 3.1C and Fig. A2.2A). Due to kinesin’s small size relative to dynein, similar assays with kinesin chassis did not allow individual occupancy numbers to be resolved (Fig. A2.2B). When the kinesin anti-handle was used with dynein, however, we again observed ~80% occupancy, indicating no handle sequence specific effects on motor-chassis linking (Fig. A2.2C and A2.2D). Super-resolution

fluorescence imaging by DNA-PAINT (*14*) revealed that sub-maximal handle incorporation into the folded chassis was probably responsible for incomplete motor occupancy (Fig. A2.3), in agreement with previous reports (*15, 16*). Negative stain transmission electron microscopy (TEM) of fully assembled chassis structures showed dynein motors occupying sites on the chassis at the programmed locations (Fig. 3.1D).

We quantified the motile properties of dynein alone or dynein ensembles on chassis with 1, 2, 4, or 7 motor attachment sites (1D, 2D, 4D, and 7D, respectively) on microtubules at the single-molecule level using total internal reflection fluorescence (TIRF) microscopy (Fig. 3.2A). The average velocity of a single dynein was similar to that of the 1D and 2D ensembles, while 4D and 7D ensembles moved slightly slower (Fig. 3.2B, and Fig. A2.4A). The characteristic run length (total distance moved) and run time (total duration of the run) of dynein ensembles increased with the number of motor sites for the 1D, 2D, and 4D ensembles (Fig. 3.2, C and D, and Fig. A2.4B and A2.4C). The 4D and 7D ensembles were so processive that their run lengths and run times were similar to each other in standard assay buffer, where microtubule length and imaging duration become limiting (Fig. 3.2, C and D). However, when assayed in high ionic strength buffer, which decreases dynein's processivity (*17*), the 7D ensemble was more processive than the 4D ensemble (Fig. 3.2, C and D, Fig. A2.4, and Fig. A2.5).

We performed a similar analysis of kinesin alone and kinesin ensembles on chassis with 1, 2, 4, or 7 motor attachment sites (1K, 2K, 4K, and 7K, respectively; Fig. 3.2, E to H). The average velocities of kinesin ensembles remained constant (Fig. 3.2F, and Fig. A2.6A), while run lengths and run times increased with increasing motor number (Fig. 3.2, G and H, and Fig. A2.6B and A2.6C).

Figure 3.2. Single-molecule motile properties of chassis-motor complexes. (A) Kymographs of TMR-labeled dynein alone and TAMRA-labeled chassis with 1, 2, or 4 dyneins. Plus (+) and minus (-) denote microtubule polarity. Scale bars: 1 min (x), 5 μ m (y). (B) Quantification of average segment velocities \pm SD of dynein and dynein-chassis complexes. The 4D and 7D ensembles moved significantly slower than dynein alone, or the 1D or 2D ensembles (one-tailed t-test, $P < 0.001$; $N \geq 211$). In higher ionic concentration (\uparrow ions), the 4D and 7D ensemble velocities were significantly different (one-tailed t-test, $P < 0.001$; $N \geq 208$). (C) Quantification of run lengths \pm SE of dynein and dynein-chassis ensembles ($N \geq 208$). (D) Quantification of total run times \pm SE of dynein and dynein-chassis ensembles ($N \geq 208$). (E) Kymographs of TAMRA-labeled kinesin alone and TAMRA-labeled chassis with 1, 2, or 4 kinesins. Scale bars: 1 min (x), 5 μ m (y). (F) Quantification of average segment velocities \pm SD of kinesin and kinesin-chassis ensembles. Comparison of velocities yielded no statistical differences (ANOVA test, $P > 0.05$; $N \geq 301$). (G) Quantification of run lengths \pm SE of kinesin and kinesin-chassis ensembles ($N \geq 301$). For additional statistical analysis see Figs. A2.4-A2.6.



Recent models of motor ensemble behavior using a transition state framework predict run lengths that are several orders of magnitude higher than we observed (18). In contrast, our data suggest that motor microtubule binding dynamics may be influenced by the presence and number of other motors on a shared cargo, similarly to previous work (19-22). For 1–7 kinesins or 1–2 dyneins, velocity was unaffected by motor number, however for 4D and 7D ensembles velocity was decreased, suggesting inter-motor interference can affect motor stepping rate. To test this hypothesis, we engineered chassis with locations for inactive mutant dyneins (denoted d^I) incapable of binding ATP at dynein's main site of ATP hydrolysis; this mutant binds microtubules tightly, but does not move (23). Dynein ensembles programmed to bind differing ratios of active and inactive motors (table A2.6) moved with reduced velocity (Fig. A2.7), demonstrating that inter-motor negative interference decreases cargo velocity.

We next investigated the motility of chassis linked to “mixed” ensembles of opposite-polarity motors. We quantified the motility of chassis as a function of dynein to kinesin (D:K) ratio (table A2.6). All mixed-motor ensembles moved unidirectionally (Fig. 3.3A) with no reversals detected at a precision of ~10 nm. With the exception of the 1D:6K chassis, all ensembles were more likely to move toward the minus end of microtubules (Fig. 3.3B). Mixed-motor ensembles were relatively insensitive to increasing the number of kinesin motors compared to increasing the number of dynein motors, which could be due to kinesin ensembles operating predominantly through the actions of fewer motors at any given time (24). Based on the stall forces of dynein (~5 pN (25)) and kinesin (~7 pN (26)), we expected kinesin plus end runs would have been more dominant. In contrast, our results suggest that stall force was not the only parameter governing the behavior of opposite-polarity motor ensembles (27). Other

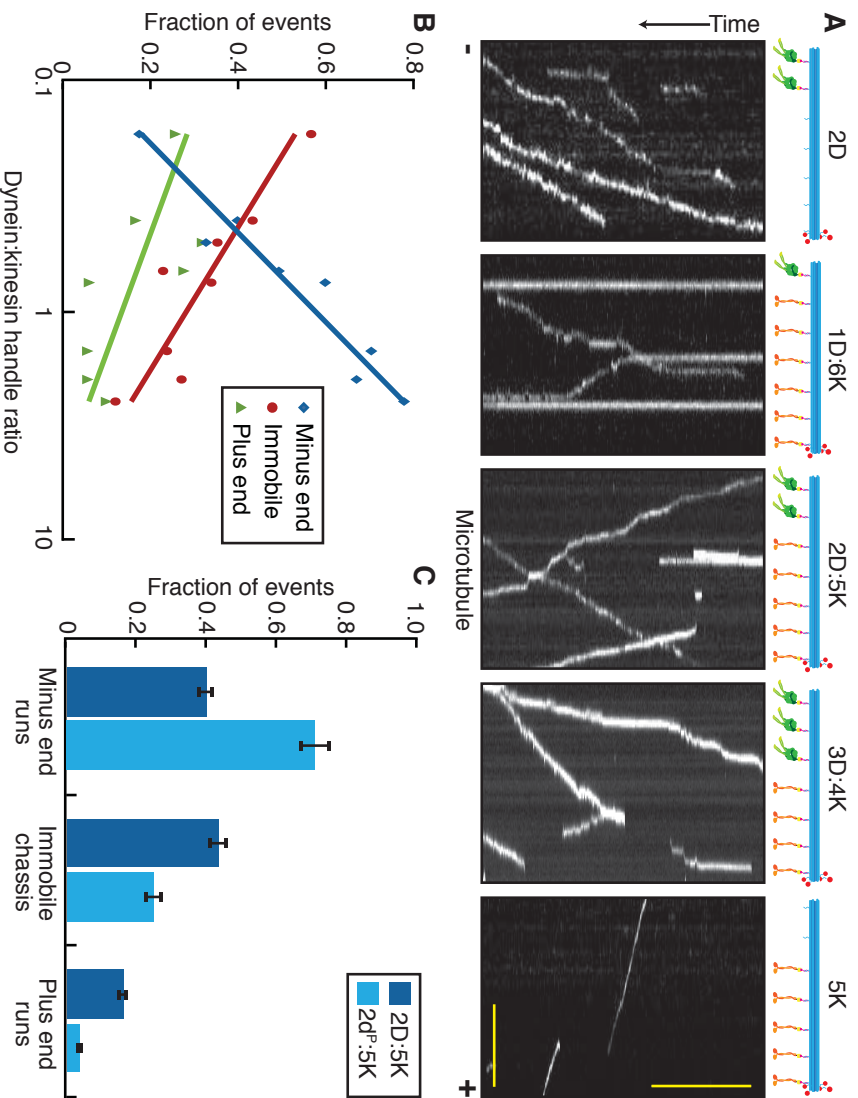


Figure 3.3. Chassis attached to dynein and kinesin frequently engage in a stalled tug of war. (A) Kymographs of TAMRA-labeled chassis attached to dynein only (left most panel), kinesin only (right most panel), or varying ratios of dynein and kinesin motors (middle panels). Plus (+) and minus (-) denote microtubule polarity. Scale bars: 1 min (x), 5 μ m (y). (B) Quantification of the fraction of events for each chassis observed as defined by their dynein to kinesin handle ratio. Chassis were immobile, moving toward the minus end, or moving toward the plus end (table A2.6, $N \geq 221$). X-axis of dynein to kinesin ratios is a logarithmic scale and linear-log fits highlight the trends observed. (C) Quantification of the fraction of events \pm SE observed to be immobile, moving toward the minus end, or moving toward the plus end for mixed ensembles containing 2 dyneins and 5 kinesins ($N \geq 352$). The dyneins were either wildtype (D) or a highly processive mutant (d^P).

parameters, such as microtubule affinity, detachment force, and velocity dependent on-rates could also be relevant (20-22, 28-31). Mixed-motor ensembles moved more slowly and for longer periods of time than equivalent single motor type ensembles (Fig. A2.8A and A2.8B), with the magnitude of this effect more pronounced in the plus end direction. Notably, mixed ensembles of dynein and kinesin were more likely to be immobile than identical-motor

ensembles, suggesting that opposite-polarity motors engage in a tug of war that prevents cargo movement (Fig. 3.3B).

Based on the longer run lengths and run times of yeast dynein as compared to human kinesin, we hypothesized that dynein runs dominated in mixed-motor ensembles due to dynein's higher microtubule affinity. To test this, we purified a mutant dynein with a higher processivity and affinity for microtubules (denoted d^P) (17) and paired it with kinesins. The 2d^P:5K ensemble was even more likely to move in the dynein direction and had fewer immobile chassis compared to the 2D:5K ensemble containing wildtype dynein (Fig. 3.3C). These results suggest that track affinity is a key motor property in governing opposite-polarity motor ensemble motility. Mixed ensembles containing the high affinity dynein mutant also produced slower plus end runs and longer run times in both directions compared to the equivalent wildtype system (Fig. A2.8C and A2.8D).

We wanted to determine if mixed-motor ensembles were non-motile due to a stalled tug of war. To regulate motor attachment to the chassis we introduced photocleavable linkers in selected handles such that illumination with a 405 nm laser released one motor type from the chassis (Fig. 3.4A). We designed two modified chassis: 2D:5K*, with photocleavable (*) kinesins, and 2D*:5K, with photocleavable dyneins. We monitored the motile properties of these chassis before and after laser-induced photocleavage (Fig. 3.4B). Cleavage was rapid (Fig. A2.9); within seconds of photocleaving motors of one type, immobile chassis moved in the direction of the remaining motors (Fig. 3.4B). We classified the state of each chassis before and after photocleavage (Fig. 3.4C) and found that the majority of stalled tug of war events were resolved into active motility (Fig. 3.4D), indicating that disengagement of one motor type can resolve tug

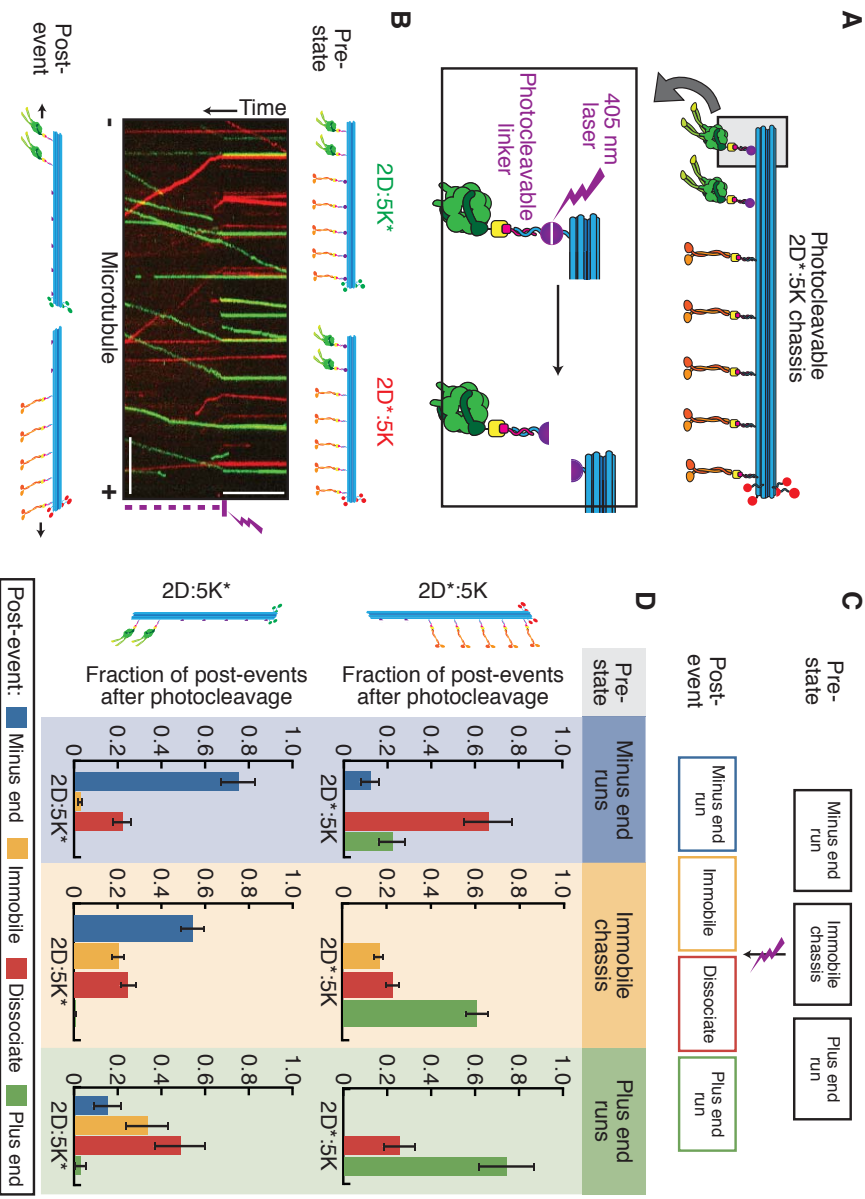


Figure 3.4. Disengagement of one motor species resolves stalled tug of war. (A) Schematic of a mixed-motor-chassis with dynein attached via photocleavable handles (purple circles). Photocleavage is induced by 405 nm laser pulses (inset). (B) Kymograph of 2D:5K*(green) and 2D*:5K (red) chassis. Purple lightning bolt indicates the start of laser pulses. Scale bars: 1 min (x), 10 μ m (y). (C) Chassis classification scheme for data presented in panel D. Before (pre-state) and after (post-event) laser photocleavage the chassis were characterized as immobile, minus-end-directed, or plus-end-directed. Possible post-events also included dissociation from the microtubule. (D) Quantification of the post-photo cleavage event motility of 2D*:5K (top) and 2D:5K* (bottom) chassis as a function of their pre-state ($N \geq 286$). Each individual post-event fraction was calculated relative to the number of events within that given pre-state.

of war events between dynein and kinesin. Although we also observed rare events where ensembles switched directions after photocleavage, more commonly we observed that moving chassis would dissociate when moving in the direction of the cleaved motor (Fig. A2.9).

Using DNA origami, we built a versatile, synthetic cargo system that allowed us to determine the motile behavior of microtubule-based motor ensembles. In ensembles of identical-polarity motors, motor number had minimal affect on directional velocity, while ensembles of

opposite-polarity motors engaged in a tug of war resolvable by disengaging one motor species.

Yeast dynein's high microtubule affinity allowed it to dominate in mixed ensembles while the ratio of dynein to kinesin dictated cargo directionality, supporting experiments performed *in vivo* or in cell-free lysates (32-34). The reduction in velocity reported here for opposite polarity motor ensembles also agrees with *in vivo* reports of dynein and kinesin tug of war (32, 35). The high probability with which mixed ensembles of active dynein and kinesin motors were immobile suggested that for this motor pair efficient bi-directional transport requires extrinsic regulation (36). Motors with comparable microtubule affinities and binding kinetics, such as those that coevolved in the same biological system, may produce bidirectional transport characteristics similar to those observed *in vivo* (6, 37, 38). The system we built provides a powerful platform to investigate the motile properties of any combination of identical- or opposite-polarity motors, and could also be used to investigate the role of motor regulation.

Methods

DNA origami twelve-helix bundle structure

The DNA origami twelve-helix bundle “chassis” was designed using caDNAno software (Fig. A2.1A, www.cadnano.org, (10)). The chassis structure contains two concentric rings, each with 6 DNA double helices (Fig. A2.1B). The chassis’ outer ring of helices is designated numbers 0, 3, 4, 7, 8, and 11 and each contain 15 “handle” locations indexed from 0 to 14. At each of these locations, an optional 21 bp single stranded DNA can be included on the 3’ end of the staple such that it projects outward from the structure to serve as an attachment site for a complementary single stranded DNA. Handle staples lacking this 21 bp projection are designated “negative handles,” while those including a handle sequence are designated “positive handles.” Helix 0 is used for motor handles or DNA PAINT handles at indices 1, 3, 5, 7, 9, 11, and 13. Motors attach to these locations via hybridization with anti-handles linked to the motors. Fluorophore-oligonucleotide anti-handles (IDT) are attached via hybridization at handle index 14 on helices 3, 4, 7, 9, and 11. For the DNA-PAINT chassis, biotinylated handles were used on helix 4, sites 5 and 13 and helix 7, sites 1 and 9.

To fold the chassis, 100 nM scaffold (10) was mixed with 600 nM core (table A2.1) and negative handle (table A2.2) staples, 3.6 μ M positive handle staples (table A2.3), and 9 μ M fluorophore-labeled anti-handles (table A2.4). Oligonucleotides were obtained from Bioneer, Invitrogen, or IDT. The folding reaction was carried out in DNA origami folding buffer (5 mM Tris [pH 8.0], 1 mM EDTA and 16 mM MgCl₂) by rapid heating to 80°C and cooling in single degree increments to 65°C over 75 min, followed by additional cooling in single degree increments to 30°C over 17.5 hr.

DNA chassis used to analyze the behavior of dynein ensembles or kinesin ensembles were purified by agarose gel electrophoresis. Structures were loaded into 2% agarose gels and run at 70 V for 3 hr in TBE buffer (45 mM Tris, 45 mM boric acid, 1 mM EDTA) supplemented with 11 mM MgCl₂. Bands corresponding to well folded monomeric chassis were excised, crushed and spun through a Freeze and Squeeze column (Bio-Rad) for 3 min at 13,000g at 4°C. Chassis were stored at 4°C.

DNA chassis used for mixed polarity motor ensemble experiments were purified by glycerol gradient sedimentation by centrifugation through a 10-45% glycerol gradient in TBE buffer supplemented with 11 mM MgCl₂ for 130 min at 242,704g in a SW50.1 (Beckman) rotor at 4°C and collected in fractions. Fractions containing well-folded monomeric chassis, assayed by 2% agarose gel electrophoresis, and were pooled and stored at 4°C.

Protein purification and oligonucleotide labeling

Amine modified DNA oligonucleotide (Bioneer) anti-handles were linked to the SNAP substrate benzylguanine (NEB) as previously described (12). Table A2.4 contains a list of anti-handle sequences used in this study. Dimeric GST-dimerized dynein (11) containing an N-terminal SNAP_f tag (NEB) was purified from *S. cerevisiae* and labeled with BG-oligonucleotides as previously described (12). Table A2.5 contains a list of yeast strains used in this study. A dimeric, truncated, human kinesin (K560 (13)) was modified to include a SNAP_f tag on the C-terminus and expressed in *E. coli* strain BL21-CodonPlus(DE3)-RIPL. Cells were grown to an optical density of 0.8-1.0 at 600 nm and were induced at 18°C for 16 hr with 0.2 mM isopropyl-β-D-thiogalactopyranoside. Cells were resuspended in kinesin lysis buffer (13) and lysed by 3

passes through a microfluidizer at 15,000 psi. Kinesin purification was then performed as previously described (*13*) with the following modification: protein labeling with BG-oligonucleotides or BG-TMR (NEB) was performed before the microtubule affinity step by labeling 2 μ M of kinesin with 60 μ M of BG-oligonucleotide at room temperature for 15 min.

Gel shift assays

Gel shift assays were performed at 22°C in TBE buffer supplemented with 11 mM MgCl₂ and 0.1% LDS and run for 4 hr at 70 V with one buffer exchange. Dynein occupancy was calculated using ImageJ by integrating the area under the line scan over the lane of a given sample for each of the detected bands. Occupancy fraction was calculated as the ratio of the signal from a given band (e.g. 4 motor band) over the sum of all signals detected for that sample.

Electron microscopy

Dynein chassis complexes were prepared and purified with Sephycryl S-500 HR as described below (see mixed motor ensemble motility assays). The mixture was then deposited on EM grids and stained as described (*15*). Images were acquired at 120 kV, under low-dose conditions, in a Tecnai T12 equipped with a LaB₆ filament and a 4k x 4k CCD camera. The nominal magnification was 41,000x, for a pixel size of 3.66 Å at the sample level.

DNA-PAINT sample preparation and imaging

Chassis with 7 handles were diluted in Buffer A (5 mM Tris-HCl [pH 8.0], 10 mM MgCl₂, 1 mM EDTA, 0.05% Tween-20) to ~50 pM and immobilized to a coverslip in a flow chamber via biotin streptavidin (12). Additionally, DNA origami based drift markers (39) were included (~5 pM). The chamber was washed with buffer A containing 5 nM anti-handle ATTO655-labeled oligonucleotide and sealed with vacuum grease.

DNA-PAINT super-resolution images (14) were acquired on an inverted Nikon Ti-E microscope (Nikon Instruments, Melville, NY) with the Perfect Focus System, applying an objective-type TIRF configuration using a Nikon TIRF illuminator with an oil-immersion objective (100× Plan Apo, NA 1.49, Oil, Nikon). A 647 nm laser (Agilent MLC400B, 80 mW at the objective) was used for TIRF excitation. The laser beam was filtered with a clean up filter (642/20 Chroma Technologies) and coupled into the microscope objective using a multi-band beamsplitter (z1405/488-491/561/638rpc, Chroma Technologies). Fluorescence was spectrally filtered with an emission filter (700/75 Chroma Technologies) and imaged on an EMCCD camera (Andor iXon 3, Andor Technologies, North Ireland). 10,000 frames were recorded at a frame rate of 10 Hz.

Super-resolution images were reconstructed using spot-finding and 2D Gaussian fitting algorithms programmed in LabVIEW (National Instruments Corporation) and available for download at www.e14.ph.tum.de. Images were drift corrected and the channels aligned using DNA-origami drift markers (39). The calculated image resolution (FWHM of 2D Gaussian fit to the reconstructed point spread function (PSF)) is ~18 nm.

Dynein and kinesin single motor motility assays

Dynein was labeled with Halo-TMR (Promega) via the C-terminal HaloTag (*II*) and an oligonucleotide via the SNAP_f tag (*I2*). Samples were diluted to ~0.1 nM and assayed as previously described (*II*). Kinesin was labeled with BG-TMR (NEB) via the C-terminal SNAP_f tag. Single molecule motility was imaged by TIRF microscopy as previously described (*I2*). Dynein was imaged using 100 ms exposures with 1.5 mW of 561 nm laser power every 2 s for 10 min, while kinesin was imaged under the same conditions every 0.5 s for 5 min. Run velocity and length were analyzed using custom ImageJ macros using kymographs generated from microtubules with a minimum length of 19 μ m. The average run velocity was calculated from segments with velocities greater than a threshold (60 nm/s for dynein and 160 nm/s for kinesin). Segments moving slower than these thresholds were considered paused and were not included in the final velocity calculations. Average run lengths and run times were determined by fitting a single exponential to the data's empirical cumulative distribution function. The resulting decay parameter is plotted with the standard error determined by bootstrapping (Fig. A2.4B, A2.4C, A2.5C, A2.5D, A2.6B, A2.6C) using MATLAB (MathWorks) software. Briefly, each run length or run time condition was resampled 200 times and the standard deviation of the resulting run length parameters represents the standard error. Run lengths were not corrected for photo-bleaching as this was measured and found to be negligible over the time scales used in this study.

Dynein or kinesin ensemble motility assays

Oligonucleotide-labeled dynein (600 nM) was mixed with chassis (~4 nM) in a 1:1 volumetric ratio for 30 min on ice (see table A2.6 for handle site locations and sequences). The

mixture was then diluted into dynein motility buffer (30 mM Hepes [pH 7.4], 50 mM KAcetate, 2 mM MgAcetate, 1 mM EGTA, 10% glycerol, 1 mM DTT, 1 mM MgATP, 2.5 mg/ml casein, and an oxygen scavenger system (40)) to achieve concentrations suitable for single molecule assays (typically 20-fold dilution). The dynein-chassis mixture was flowed into assay chambers containing surface-immobilized microtubules prepared as described (11). TAMRA-labeled chassis-dynein complexes were imaged every 2 s for 10 min. Oligonucleotide-labeled kinesin (600 nM) was mixed with chassis (~4 nM) and incubated on ice for 30 min. The mixture was diluted (typically 20-fold dilution) in kinesin motility buffer (12 mM PIPES [pH 6.8], 2 mM MgAcetate, 1 mM EGTA, 10 mM BME, 1 mM MgATP, and oxygen scavenger system (40)). Kinesin chassis were imaged every 0.5 s for 5 min. Kymographs were generated using ImageJ and analyzed by the same methods employed for the motor alone motility assays. For the 4 and 7 dynein-chassis experiments, only microtubules which were 65 μ m or greater were used for kymograph analysis.

Mixed motor ensemble motility assays

Mixed motor ensemble motility assays were performed in dynein motility buffer supplemented with an additional 50 mM KCl. Kinesin alone moved similarly in dynein and kinesin motility buffers, with a velocity of 542 ± 196 nm/s (SD) and run length of 2.21 ± 0.12 μ m (SE) in dynein motility buffer compared to a velocity of 608 ± 145 nm/s (SD) and run length of 2.39 ± 0.15 μ m (SE) in kinesin motility buffer.

Dynein (5 μ l of 300 nM dynein-oligo A), kinesin (5 μ l of 600 nM kinesin-oligo B), and chassis (5 μ l of 12 nM) were mixed and incubated on ice for 30 min (see table A2.6 for handle

site locations and sequences). The mixture was then diluted 3.3-fold in dynein motility buffer lacking casein and the oxygen scavenging system. The motor-chassis complexes were separated from free motors by centrifuging at 1000g over ~450 µl of packed Sephadryl S-500 HR resin (GE Healthcare) in a micro chromatography spin column (BioRad) for 10 s. The resulting mixture was diluted (typically ~5-fold) in dynein motility buffer containing a final concentration of 2.5 mg/ml casein and 1X oxygen scavenging system. TAMRA-labeled chassis complexes were imaged every 0.5 s for 10 min. A highly processive dynein mutant (E3107K, E3197K; termed d^P here) (17) was used to test the effects of microtubule affinity on ensemble behavior.

A different highly processive dynein mutant (E3197K) was used to determine microtubule polarity (17). Briefly, this mutant was labeled with Atto647N via a C-terminal HaloTag (*II*) and added at ~0.1 nM to all mixed ensemble motility assays. In each experiment, after imaging chassis motility, the same field of view was imaged every 2 s for 3 min in the 640 TIRF channel to observe E3197K dynein moving on the same microtubules, allowing the determination of microtubule polarity. Microtubules were labeled with HyLite-488 (Cytoskeleton Inc.) as described (<http://mitchison.med.harvard.edu/protocols.html>).

Kymographs were generated using ImageJ software and analyzed as described above. Run lengths and velocities were calculated as before using 10 nm/s as a lower limit for the velocity threshold for both plus- and minus-end-directed runs. To determine the fraction of events, the number of specific observations for a given event (e.g. the number of plus end runs) was tallied and normalized by the total number of observations. Error bars represent SE of the count determined by taking the square root of the number of observations for the specific event and normalizing by the total number of observations.

Photocleavage experiments

Motor-chassis complexes containing photocleavable handles (see table A2.6 for handle site locations and sequences) were prepared and imaged as described for the mixed motor ensembles with the following exceptions. TAMRA oligos were used to visualize 2D*:5K chassis, while Cy5 oligos were used for 2D:5K* chassis. The TAMRA and Cy5 channels were imaged for 100 ms every 1 s. After 1 min the 405 nm laser (0.5 mW) was pulsed on for 400 ms every 1 s, while Cy5 and TAMRA imaging continued every 1 s for another 4 min. Kymographs were used to determine if each chassis event was immobile, moving toward the microtubule plus end, moving toward the microtubule minus end, or dissociated (post laser cleavage only). The behavior of each chassis was determined both before and after photocleavage. The counts of the transitions between these pre- and post-states are presented in Figure 3.4D for each chassis type. Fractions were calculated by dividing the number of events observed for a particular behavior (minus-end-directed, immobile, dissociated, plus-end-directed) for each pre-state by the total number of observed events within that pre-state. Normalized error of the counts was calculated as the square root of the count divided the total number of events observed in that pre-state. Figures A2.9C and A2.9D present the same data as a fraction of all events observed regardless of their pre-state, allowing the relative frequency to be ascertained for all pre- and post-state pairs. To generate the kymograph in Figure 3.4B, the experiment was repeated under conditions where the extra 50 mM KCl was not added to increase the initial immobile fraction and highlight the resolution of the tug of war.

To determine if photocleavage was specific for chassis containing a photocleavable handle, 1D* (photocleavable handle) or 1D (standard handle) chassis were immobilized on

microtubules and imaged as described for the 2D:5K chassis. 405 nm laser illumination did not induce cleavage of the 1D chassis (Fig. A2.9A). A 2D:5K chassis with standard handles was also imaged using the above photocleavage imaging protocol and the 405nm laser pulses had no effect on motility.

To determine the kinetics of photocleavage, 1D* or 1D chassis were immobilized on a coverslip and imaged as described for the 2D:5K chassis. Chassis coupled to motors stuck non-specifically to coverslips, while chassis alone did not. The mean intensity for each frame was calculated in ImageJ for the image stack and exported to MATLAB (MathWorks) for analysis. After 405 nm laser illumination, the 1D* data was fit with a two phase exponential curve ($f(x)=a*EXP(b*x) + c*EXP(d*x)$) where a and b were parameters of the fast phase of the exponential, representing the loss of fluorescence due to photocleavage, and c and d were parameters representing the slow phase of photobleaching). After 405 nm laser illumination, the 1D data was fit with a single exponential curve ($f(x)=c*EXP(d*x)$). Photobleaching curves in both cases were negligible as the rate of bleaching was 4 orders of magnitude smaller than the rate of photocleavage. The imaging and fitting analysis was repeated at least 4 times for each condition, and the mean and SE of b is reported as the fast phase photocleavage constant while d is the slow phase, bleaching decay constant. An example trace of a single experiment is shown in figure A2.9B. For graphing purposes the 1D data was linearly offset by a constant such that the two data sets started at the same initial mean intensity.

Acknowledgements

We thank C. Lin for assistance with electron microscopy; F. Aguet for assistance with data analysis; J. Huang, W. Qiu, W.B. Redwine, and A. Roberts for helpful advice and critical reading of the manuscript; members of the Reck-Petersen and Shih labs for advice and helpful discussions; and J. Iwasa for illustrations. EM data were collected at the Center for Nanoscale Systems, Harvard University. DNA-PAINT data were collected at the Nikon Imaging Center, Harvard Medical School. R.J. is supported from the Alexander von Humboldt Foundation through a Feodor Lynen fellowship. S.L.R.-P. is funded by the Rita Allen Foundation, the Harvard Armenian Foundation, and a NIH New Innovator award (1 DP2 OD004268-1). W.M.S. is funded by NIH awards (1U54GM094608 and 1DP2OD004641) and ONR awards (N000014091118 and N000141010241).

References

1. N. Hirokawa, S. Niwa, Y. Tanaka, Molecular motors in neurons: transport mechanisms and roles in brain function, development, and disease, *Neuron* **68**, 610–638 (2010).
2. R. D. Vale, The molecular motor toolbox for intracellular transport, *Cell* **112**, 467–480 (2003).
3. R. B. Vallee, The cellular roles of the lissencephaly gene LIS1, and what they tell us about brain development, *Genes & Development* **20**, 1384–1393 (2006).
4. G. T. Banks, E. M. C. Fisher, Cytoplasmic dynein could be key to understanding neurodegeneration, *Genome Biol.* **9**, 214 (2008).
5. A. Desai, T. J. Mitchison, MICROTUBULE POLYMERIZATION DYNAMICS, <http://dx.doi.org/10.1146/annurev.cellbio.13.1.83> **13**, 83–117 (1997).
6. M. A. Welte, Bidirectional Transport along Microtubules, *Current Biology* **14**, R525–R537 (2004).
7. S. A. Bryantseva, O. N. Zhapparova, Bidirectional transport of organelles: unity and struggle of opposing motors, **36**, 1–6 (2011).
8. P. W. K. Rothemund, Folding DNA to create nanoscale shapes and patterns, *Nature* **440**, 297–302 (2006).
9. S. M. Douglas *et al.*, Self-assembly of DNA into nanoscale three-dimensional shapes, *Nature* **459**, 414–418 (2009).
10. S. M. Douglas *et al.*, Rapid prototyping of 3D DNA-origami shapes with caDNAno, *Nucleic Acids Research* **37**, 5001–5006 (2009).
11. S. L. Reck-Peterson *et al.*, Single-Molecule Analysis of Dynein Processivity and Stepping Behavior, *Cell* **126**, 335–348 (2006).
12. W. Qiu *et al.*, Dynein achieves processive motion using both stochastic and coordinated stepping, *Nat Struct Mol Biol* **19**, 193–200 (2012).
13. R. B. Case, D. W. Pierce, N. Hom-Booher, C. L. Hart, R. D. Vale, The directional preference of kinesin motors is specified by an element outside of the motor catalytic domain, *Cell* **90**, 959–966 (1997).
14. R. Jungmann *et al.*, Single-molecule kinetics and super-resolution microscopy by fluorescence imaging of transient binding on DNA origami, *Nano Lett.* **10**, 4756–4761 (2010).

15. Y. Ke, N. V. Voigt, K. V. Gothelf, W. M. Shih, Multilayer DNA Origami Packed on Hexagonal and Hybrid Lattices, *J. Am. Chem. Soc.* **134**, 1770–1774 (2012).
16. S. H. Ko, G. M. Gallatin, J. A. Liddle, Nanomanufacturing with DNA Origami: Factors Affecting the Kinetics and Yield of Quantum Dot Binding, *Adv. Funct. Mater.* **22**, 1015–1023 (2012).
17. W. B. Redwine *et al.*, Structural basis for microtubule binding and release by dynein, *Science (New York, N.Y.)* **337**, 1532–1536 (2012).
18. S. Klumpp, R. Lipowsky, Cooperative cargo transport by several molecular motors, *Proc. Natl. Acad. Sci. U.S.A.* **102**, 17284–17289 (2005).
19. C. Leduc, N. Pavin, F. Jülicher, S. Diez, Collective Behavior of Antagonistically Acting Kinesin-1 Motors, *Phys. Rev. Lett.* **105**, 128103 (2010).
20. A. R. Rogers, J. W. Driver, P. E. Constantinou, D. Kenneth Jamison, M. R. Diehl, Negative interference dominates collective transport of kinesin motors in the absence of load, *Phys. Chem. Chem. Phys.* **11**, 4882–4889 (2009).
21. H. Lu *et al.*, Collective Dynamics of Elastically Coupled Myosin V Motors, *Journal of Biological Chemistry* **287**, 27753–27761 (2012).
22. J. Xu, Z. Shu, S. J. King, S. P. Gross, Tuning Multiple Motor Travel via Single Motor Velocity, *Traffic* **13**, 1198–1205 (2012).
23. T. Kon, M. Nishiura, R. Ohkura, Y. Y. Toyoshima, K. Sutoh, Distinct Functions of Nucleotide-Binding/Hydrolysis Sites in the Four AAA Modules of Cytoplasmic Dynein †, *Biochemistry* **43**, 11266–11274 (2004).
24. D. K. Jamison, J. W. Driver, A. R. Rogers, P. E. Constantinou, M. R. Diehl, Two Kinesins Transport Cargo Primarily via the Action of One Motor: Implications for Intracellular Transport, *Biophysical Journal* **99**, 2967–2977 (2010).
25. A. Gennrich, A. P. Carter, S. L. Reck-Peterson, R. D. Vale, Force-Induced Bidirectional Stepping of Cyttoplasmic Dynein, *Cell* **131**, 952–965 (2007).
26. A. Yildiz, M. Tomishige, A. Gennrich, R. D. Vale, Intramolecular Strain Coordinates Kinesin Stepping Behavior along Microtubules, *Cell* **134**, 1030–1041 (2008).
27. P. E. Constantinou, M. R. Diehl, The mechanochemistry of integrated motor protein complexes, *Journal of Biomechanics* **43**, 31–37 (2010).
28. M. Y. Ali *et al.*, Myosin Va and myosin VI coordinate their steps while engaged in an in vitro tug of war during cargo transport, *108*, E535–41 (2011).

29. R. D. Vale, F. Malik, D. Brown, Directional instability of microtubule transport in the presence of kinesin and dynein, two opposite polarity motor proteins, **119**, 1589–1596 (1992).
30. A. Kunwar, M. Vershinin, J. Xu, S. P. Gross, Stepping, Strain Gating, and an Unexpected Force-Velocity Curve for Multiple-Motor-Based Transport, *Current Biology* **18**, 1173–1183 (2008).
31. D. K. Jamison, J. W. Driver, M. R. Diehl, Cooperative Responses of Multiple Kinesins to Variable and Constant Loads, *Journal of Biological Chemistry* **287**, 3357–3365 (2012).
32. V. Levi, A. S. Serpinskaya, E. Gratton, V. Gelfand, Organelle transport along microtubules in *Xenopus melanophores*: evidence for cooperation between multiple motors, *Biophysical Journal* **90**, 318–327 (2006).
33. M. Schuster, R. Lipowsky, M.-A. Assmann, P. Lenz, G. Steinberg, Transient binding of dynein controls bidirectional long-range motility of early endosomes, **108**, 3618–3623 (2011).
34. M. Amute-Nayak, S. L. Bullock, Single-molecule assays reveal that RNA localization signals regulate dynein–dynactin copy number on individual transcript cargoes, *Nature Cell Biology* **14**, 416–423 (2012).
35. V. Soppina, A. K. Rai, A. J. Ramaiya, P. Barak, R. Mallik, Tug-of-war between dissimilar teams of microtubule motors regulates transport and fission of endosomes, **106**, 19381–19386 (2009).
36. A. Kunwar *et al.*, Mechanical stochastic tug-of-war models cannot explain bidirectional lipid-droplet transport, **108**, 18960–18965 (2011).
37. S. E. Encalada, L. Szpankowski, C.-H. Xia, L. S. B. Goldstein, Stable Kinesin and Dynein Assemblies Drive the Axonal Transport of Mammalian Prion Protein Vesicles, *Cell* **144**, 551–565 (2011).
38. M. J. Egan, K. Tan, S. L. Reck-Peterson, Lis1 is an initiation factor for dynein-driven organelle transport, *J. Cell Biol.* **197**, 971–982 (2012).
39. C. Lin *et al.*, Sub-micrometer geometrically encoded fluorescent barcodes self-assembled from DNA, *Nature Chem.*, 1–21 (2012).
40. A. Yildiz, Myosin V Walks Hand-Over-Hand: Single Fluorophore Imaging with 1.5-nm Localization, *Science (New York, N.Y.)* **300**, 2061–2065 (2003).

Chapter 4

Conclusions

Nathan D. Derr

Concluding remarks

Structural DNA nanotechnology has proven to be a versatile tool for single molecule investigations of molecular motors. Several reports regarding the biophysical mechanisms of cytoskeletal motors elucidated with the aid of DNA nanotechnology have been published (1-8). From this body of work, the advantages of DNA construction techniques are clearly apparent. By offering control over the relative geometry and stoichiometry of motors and motor domains, these methods provide unique tools previously unavailable. Of the capabilities of these systems, perhaps the most advantageous and enabling is the ability to design and build tools at the same size scale as the proteins of interest. Importantly, these capabilities are not specific to motors, but can equally be applied towards investigations of many different biological processes and proteins. There have been separate exponential rises in recent years of publications of single molecule experiments (9) and citations of DNA nanotechnology systems (10). I believe it likely that applications of this nanotechnology to single molecule investigations will see a commensurate increase in interest and publications over the years ahead.

Our application of DNA-based nanoscale construction to the mechanisms of dynein coordination has created a robust experimental platform (6). From this work, a unique mechanism for dynein's processive motion was determined. We found that the motor exhibits two different modes of stepping: a stochastic mode when the two motor domains are close together, and a tension-based coordinated stepping that increasingly favors the lagging head to step as the distance between the two heads increases. Given the synthetic nature of this system, a clear and important consideration is any potential for altering dynein's mechanism through

dimerization by DNA. Our comparisons of the motor's activity to that of native dynein suggest that the DNA-based heterodimers are an excellent model system for the motor. Additionally, a near simultaneously published report (*II*), using rapamycin-mediated dynein heterodimers (*I2*), arrived at strikingly similar conclusions regarding the motor's stepping patterns in both the spatial and temporal domains. This independent confirmation of the motor's stochastic and coordinated stepping regimes provides further data indicating the utility of artificially dimerized motors and their ability to serve as model motor molecules.

Despite this work, our understanding of how dynein achieves processive motion is incomplete. The effects of many contributing interactions and parameters are undetermined, as is the structural basis of the tension-based coordination. In particular, the complex *in vivo* landscape in which dynein operates could affect the motor's mechanisms in significant ways. Future experiments will need to investigate the roles of dynein's many accessory factors (*I3*), as well as the effect of cargo load (*I4*), on how dynein steps. Experiments regarding dynein's myriad binding partners may best be executed using native dynein, as the tail domain is known to be the site of some protein-protein interactions with the motor (*I3*). However, our DNA-based heterodimers offer a sound experimental platform for investigating how load impacts dynein stepping. The ssDNA oligos that dimerize the two dynein protomers could also be used as a specific attachment site for the conjugation of these motors to beads (*I5*). Once bound to a bead, optical trapping assays could be conducted to determine how load affects the motor's processive stepping. As tension appears to play a role in how the motor moves, such load may be an important factor as it could supply a constant rearward force on the motor and thus diminish the

likelihood that the motor's leading head would step. Finally, a future experiment that reported upon the tension between the two dynein protomers would be enlightening. Such a system would require that the motor be dimerized via a tension-reporting nano-device of some kind.

By conjugating motors to short DNA oligonucleotides, we were able to use DNA origami to create well-defined motor assemblies, allowing us to investigate the interactions of homo- and hetero-meric ensembles (7). Over the past decade, models and hypotheses of motor interactions within ensembles have become increasingly complex and sophisticated, taking into account stochastic, energetic, biochemical, biophysical, and geometrical parameters (16-23). Yet, conceptually simple questions have remained unanswered experimentally. Our DNA origami-based system provides a direct means for addressing these models *in vitro*, and is a first step towards a more comprehensive understanding of the biophysical mechanism that lead to collective motor behavior.

Importantly, our experimental work highlighted the biophysical complexity of these ensembles. While a universal model of collective motor motility may one day be achieved, in the near term such a comprehensive model seems unlikely as there are significant biophysical variations in motors from different species and among motor isoforms. As ensemble motile behavior depends heavily on many factors (1, 5, 24-29), such as track affinity (7), each motor isoform or motor type from each species may need to be assayed separately. Ideally, a complete understanding of how individual motor parameters affect collective behavior will be achieved for cargo hauling homo- and hetero-meric motors that co-evolved together in one species. A model

based upon this understanding could then be used to make testable predictions about motors with differing parameters.

Future work observing the stepping of individual motors within ensembles will be technically challenging, but potentially enlightening. Such work could establish the extent to which motors synchronize, and how negative interference specifically manifests within the

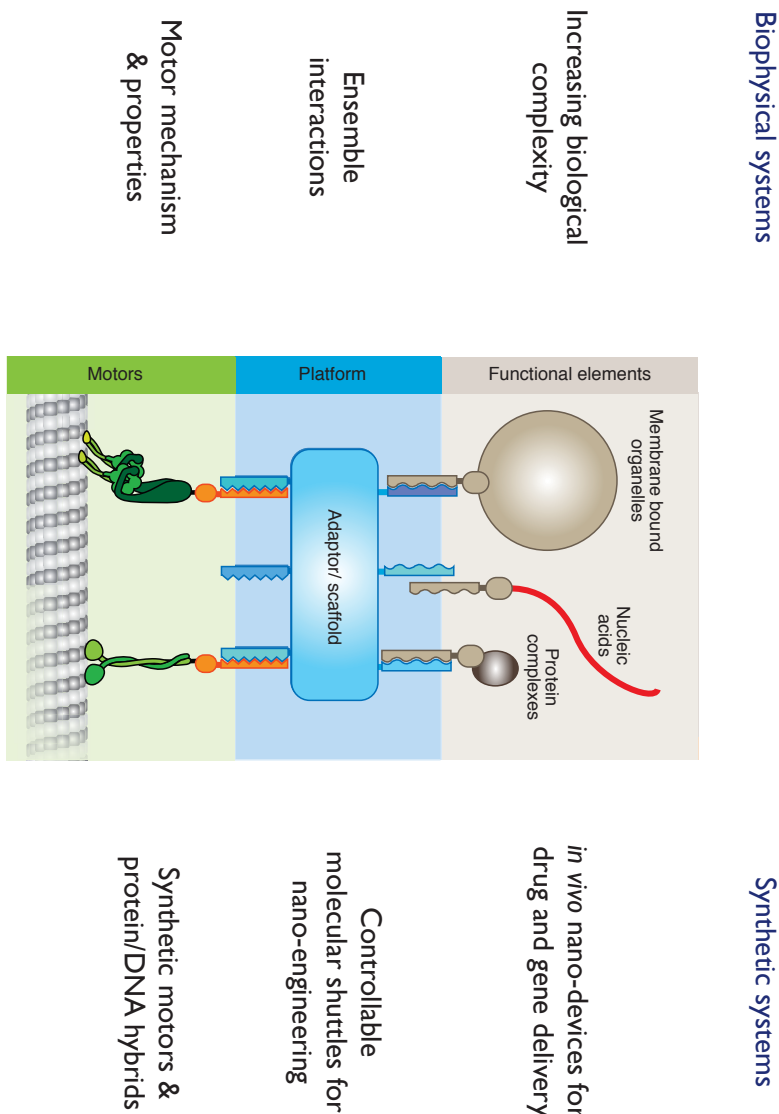


Figure 4.1 Synthetic motor assemblies for biophysics and nanoscale molecular shuttles. Conceptual diagram of applications resulting from treating motors and motor assemblies as interchangeable parts. Motors (green) drive the motility of a scaffold (blue) also linked to functional elements (beige). The system can be applied towards deciphering the biophysical mechanisms of motor systems crucial to the proper functioning of cells. It can also be engineered for synthetic purposes for nanotechnological and biomedical applications. Figure adapted from (35).

ensemble. Cargo shape also likely places a role in the emergent ensemble motility (18). DNA origami lends itself well to the construction of multiple shapes and thus will be useful in experiments focused on the role that shape plays in cargo motility. Finally, the collective force output of defined motor ensembles *in vitro* has only been characterized for homomeric teams of dyneins (3, 8). Similar observations with homomeric dynein and heteromeric ensembles are needed.

Finally, the experiments discussed in this dissertation were made possible by an approach that treated motors and motor domains as interchangeable mechanical parts. Through linkages to specific DNA sequences, these parts could be conjugated together and onto larger scaffolding structures in specified architectures. While the goal of this work was an elucidation of the biophysical mechanisms of these motors, an additional outcome has been the creation of engineered nanoscale transport devices. Combining re-engineered natural motors (30) on DNA origami scaffolds could provide well-defined platforms for molecular shuttles for nanotechnological and biomedical applications (Figure 4.1) (31-34).

References

1. A. R. Rogers, J. W. Driver, P. E. Constantinou, D. Kenneth Jamison, M. R. Diehl, Negative interference dominates collective transport of kinesin motors in the absence of load, *Phys. Chem. Chem. Phys.* **11**, 4882–4889 (2009).
2. D. K. Jamison, J. W. Driver, A. R. Rogers, P. E. Constantinou, M. R. Diehl, Two Kinesins Transport Cargo Primarily via the Action of One Motor: Implications for Intracellular Transport, *Biophysical Journal* **99**, 2967–2977 (2010).
3. D. K. Jamison, J. W. Driver, M. R. Diehl, Cooperative Responses of Multiple Kinesins to Variable and Constant Loads, *Journal of Biological Chemistry* **287**, 3357–3365 (2012).
4. Y. Miyazono, M. Hayashi, P. Karagiannis, Y. Harada, H. Tadakuma, Strain through the neck linker ensures processive runs: a DNA-kinesin hybrid nanomachine study, *EMBO J.* **29**, 93–106 (2010).
5. H. Lu *et al.*, Collective Dynamics of Elastically Coupled Myosin V Motors, *Journal of Biological Chemistry* **287**, 27753–27761 (2012).
6. W. Qiu *et al.*, Dynein achieves processive motion using both stochastic and coordinated stepping, *Nat Struct Mol Biol* **19**, 193–200 (2012).
7. N. D. Derr *et al.*, Tug-of-war in motor protein ensembles revealed with a programmable DNA origami scaffold, *Science (New York, N.Y.)* **338**, 662–665 (2012).
8. K. Furuta *et al.*, Measuring collective transport by defined numbers of processive and nonprocessive kinesin motors, *Proc. Natl. Acad. Sci. U.S.A.* **110**, 501–506 (2013).
9. C. Joo, H. Balci, Y. Ishitsuka, C. Buranachai, T. Ha, Advances in single-molecule fluorescence methods for molecular biology, *Annu. Rev. Biochem.* **77**, 51–76 (2008).
10. V. Linko, H. Dietz, The enabled state of DNA nanotechnology, *Curr. Opin. Biotechnol.* (2013), doi:10.1016/j.copbio.2013.02.001.
11. M. A. DeWitt, A. Y. Chang, P. A. Combs, A. Yildiz, Cytoplasmic dynein moves through uncoordinated stepping of the AAA+ ring domains, *Science (New York, N.Y.)* **335**, 221–225 (2012).
12. S. L. Reck-Peterson *et al.*, Single-Molecule Analysis of Dynein Processivity and Stepping Behavior, *Cell* **126**, 335–348 (2006).
13. J. R. Kardon, R. D. Vale, Regulators of the cytoplasmic dynein motor, *Nat Rev Mol Cell Biol* **10**, 854–865 (2009).

14. A. Gemnerich, A. P. Carter, S. L. Reck-Peterson, R. D. Vale, Force-Induced Bidirectional Stepping of Cytoplasmic Dynein, *Cell* **131**, 952–965 (2007).
15. N. R. Guydosh, S. M. Block, Direct observation of the binding state of the kinesin head to the microtubule, *Nature* **461**, 125–128 (2009).
16. S. Klumpp, R. Lipowsky, Cooperative cargo transport by several molecular motors, *Proc. Natl. Acad. Sci. U.S.A.* **102**, 17284–17289 (2005).
17. M. J. I. Müller, S. Klumpp, R. Lipowsky, Bidirectional Transport by Molecular Motors: Enhanced Processivity and Response to External Forces, *Biophysical Journal* **98**, 2610–2618 (2010).
18. R. P. Erickson, Z. Jia, S. P. Gross, C. C. Yu, How molecular motors are arranged on a cargo is important for vesicular transport, *PLoS Comput. Biol.* **7**, e1002032 (2011).
19. S. A. McKinley, A. Athreya, J. Fricks, P. R. Kramer, Asymptotic analysis of microtubule-based transport by multiple identical molecular motors, *J. Theor. Biol.* **305**, 54–69 (2012).
20. J. E. Martinez, M. D. Vershinin, G. T. Shubeita, S. P. Gross, On the use of in vivo cargo velocity as a biophysical marker, *Biochem. Biophys. Res. Commun.* **353**, 835–840 (2007).
21. J. W. Driver *et al.*, Coupling between motor proteins determines dynamic behaviors of motor protein assemblies, *Phys. Chem. Chem. Phys.* **12**, 10398 (2010).
22. J. W. Driver *et al.*, Productive Cooperation among Processive Motors Depends Inversely on Their Mechanochemical Efficiency, *Biophysical Journal* **101**, 386–395 (2011).
23. K. Uppulury *et al.*, How the Interplay between Mechanical and Nonmechanical Interactions Affects Multiple Kinesin Dynamics, *J. Phys. Chem. B* **116**, 8846–8855 (2012).
24. J. Xu, Z. Shu, S. J. King, S. P. Gross, Tuning Multiple Motor Travel via Single Motor Velocity, *Traffic* **13**, 1198–1205 (2012).
25. R. D. Vale, F. Malik, D. Brown, Directional instability of microtubule transport in the presence of kinesin and dynein, two opposite polarity motor proteins, **119**, 1589–1596 (1992).
26. C. Leduc, N. Pavin, F. Jülicher, S. Diez, Collective Behavior of Antagonistically Acting Kinesin-1 Motors, *Phys. Rev. Lett.* **105**, 128103 (2010).
27. M. Y. Ali *et al.*, Myosin Va and myosin VI coordinate their steps while engaged in an in vitro tug of war during cargo transport, **108**, E535–41 (2011).
28. A. Kunwar *et al.*, Mechanical stochastic tug-of-war models cannot explain bidirectional lipid-droplet transport, **108**, 18960–18965 (2011).

29. A. Kunwar, M. Vershin, J. Xu, S. P. Gross, Stepping, Strain Gating, and an Unexpected Force-Velocity Curve for Multiple-Motor-Based Transport, *Current Biology* **18**, 1173–1183 (2008).

30. L. Chen, M. Nakamura, T. D. Schindler, D. Parker, Z. Bryant, Engineering controllable bidirectional molecular motors based on myosin, *Nature Nanotech* **7**, 252–256 (2012).

31. H. Hess, Engineering applications of biomolecular motors, *Annu Rev Biomed Eng* **13**, 429–450 (2011).

32. A. Goel, V. Vogel, Harnessing biological motors to engineer systems for nanoscale transport and assembly, *Nature Nanotech* **3**, 465–475 (2008).

33. M. G. L. van den Heuvel, C. Dekker, Motor proteins at work for nanotechnology, *Science (New York, N.Y.)* **317**, 333–336 (2007).

34. T. Korten, A. Måansson, S. Diez, Towards the application of cytoskeletal motor proteins in molecular detection and diagnostic devices, *Curr. Opin. Biotechnol.* **21**, 477–488 (2010).

35. B. S. Goodman, N. D. Derr, S. L. Reck-Peterson, Engineered, harnessed, and hijacked: synthetic uses for cytoskeletal systems, *Trends Cell Biol.* **22**, 644–652 (2012).

Appendix 1

Supplemental Figures and Tables for:

Dynein achieves processive motion

using both stochastic and coordinated stepping

Weihong Qiu, Nathan D. Derr, Brian S. Goodman, Elizabeth Villa,
David Wu, William M. Shih and Samara L. Reck-Peterson

Contributions

Nathan Derr and Weihong Qiu contributed equally. Nathan Derr and Weihong Qiu initiated the project. Nathan Derr designed the DNA-based heterodimerization method. Weihong Qiu developed the 2D tracking methods. Weihong Qiu, Nathan Derr and Brian Goodman conducted the experiments and analyzed the data. Elizabeth Villa and David Wu wrote the 2D tracking software. Samara Reck-Peterson and William Shih provided mentorship. This work was published in: Dynein achieves processive motion using both stochastic and coordinated stepping, *Nature Structural Molecular Biology* **19**, 193–200 (2012).

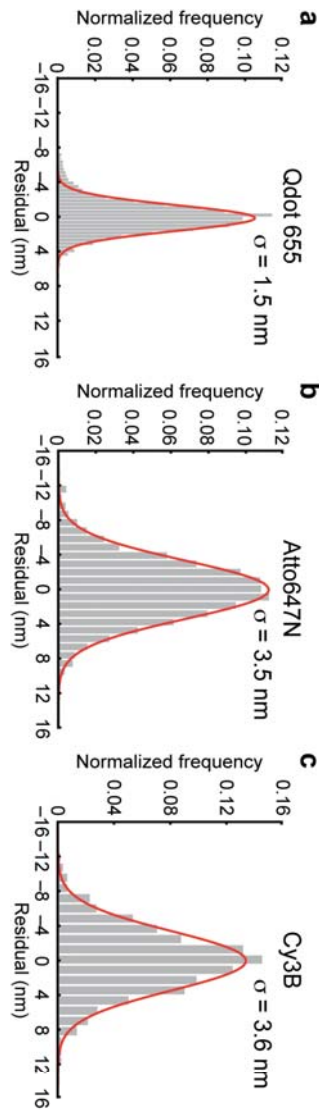


Figure A1.1 Single molecule localization precision. (a-c) To determine the precision of our single molecule measurements, we immobilized fluorophores separately on a coverslip and used a piezo nanostage to drive a staircase pattern of precise increments (6 nm for Qdot 655, 16 nm for both Atto647N and Cy3B). After each increment, at least 10 images were taken using the same exposure time and laser power as the experimental conditions used for tracking dynein. The point-spread function of individual fluorophores was fit with a 2-D Gaussian to determine their centroid position and a step-finding program was used to determine the average position after each increment. Histograms show the distribution of the difference between the raw centroid positions and the average positions between stage movements along one axis. The sigma value (the s.d. of the Gaussian fit) reports the localization precision of each fluorophore. (a) Qdot 655 ($\sigma = 1.5$ nm, $N = 4041$), (b) Atto647N ($\sigma = 3.5$ nm, $N = 2378$), (c) Cy3B ($\sigma = 3.6$ nm, $N = 1632$).

Figure A1.2

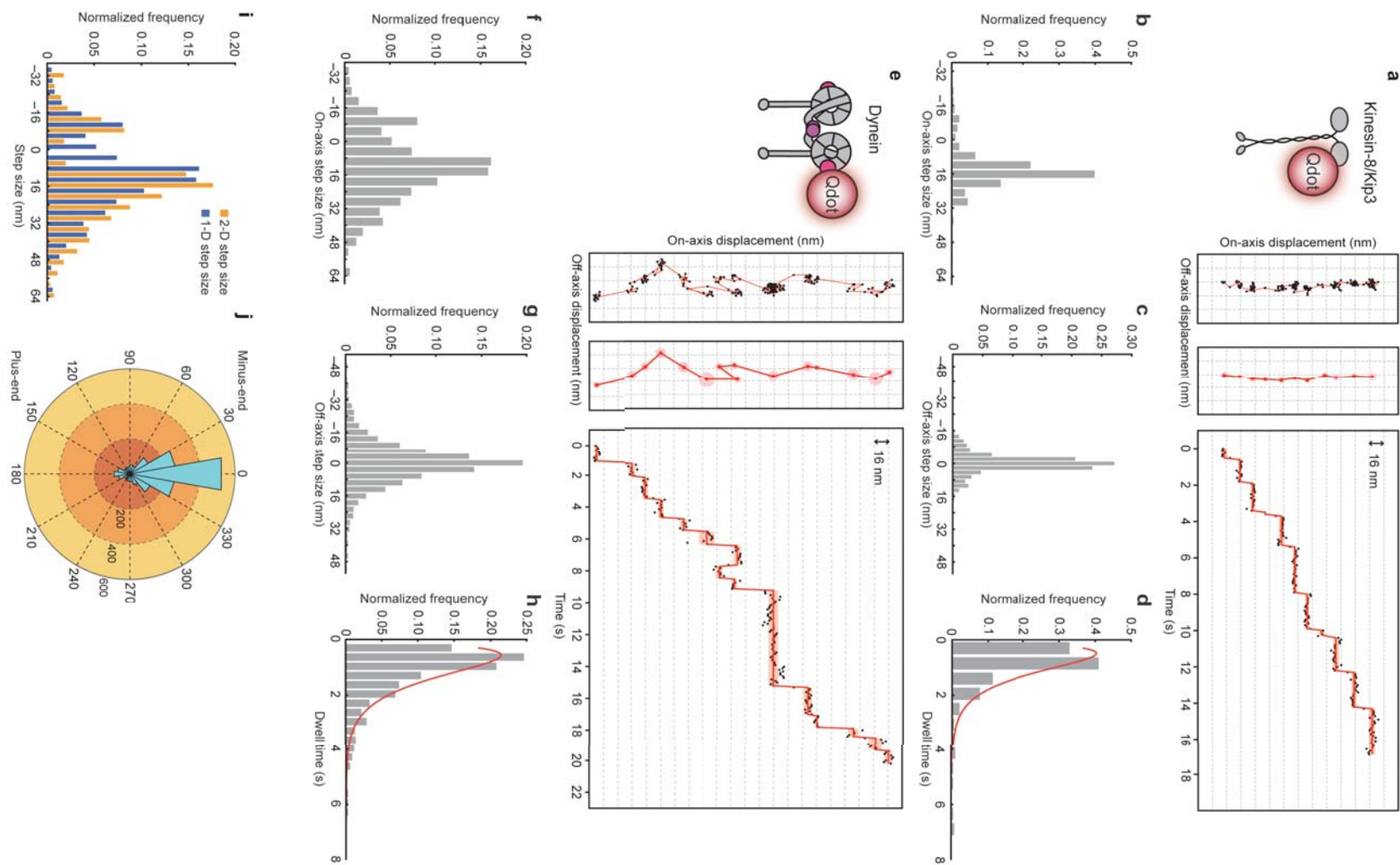


Figure A1.2 (continued).

Figure A1.2 Stepping behavior of motor domain labeled kinesin-8/Kip3 and dynein. (a) Representative one-color trace of kinesin-8/Kip3 labeled with a Qdot 655 attached to a single motor domain via a N-terminal HaloTag. Panel 1 shows the raw 2-D stepping data (black dots linked with red lines). Panel 2 shows the step positions as determined by a 2-D step finding algorithm (dark red circles and lines; lighter colored red circles represent the s.d.). All grid lines have 16 nm spacing. Panel 3 shows the 1-D on-axis projection of the 2-D steps. Black dots are the raw data, red lines are the steps determined by the 2-D step finding algorithm, and the light red bars indicate the s.d. of individual steps along the projection axis. (b) Histogram of the on-axis step size for motor domain labeled kinesin-8/Kip3. $N = 384$ for panels b-d. (c) Histogram of the off-axis step size for motor domain labeled kinesin-8/Kip3. 22%, 16%, and 11% of steps are greater than 4, 6, and 8 nm, respectively. (d) Histogram of dwell times for motor domain labeled kinesin-8/Kip3 fit to a convolution of two exponential functions with equal decay constants, with a rate of $k = 2.06 + 0.31 \text{ s}^{-1}$. Stepping data was acquired at 500 μM ATP every 100 ms. (e) Representative one-color traces of GST-dynein homodimers labeled with a Qdot 655 attached to a single motor domain via a C-terminal HaloTag. Panel 1 shows the raw 2-D stepping data (black dots linked with red lines). Panel 2 shows the step positions as determined by a 2-D step finding algorithm (dark red circles and lines; lighter colored red circles represent the s.d.). All grid lines have 16 nm spacing. Panel 3 shows the 1-D on-axis projection of the 2-D steps. Black dots are the raw data, red lines are the steps determined by the 2-D step finding algorithm, and the light red bars indicate the s.d. of individual steps along the projection axis. (f) Histogram of the on-axis step size for motor domain labeled GST-dynein. $N = 1939$ for panels f-h. (g) Histogram of the off-axis step size for motor domain labeled GST-dynein. 59%, 45%, and 36% of steps are greater than 4, 6, and 8 nm, respectively. (h) Histogram of dwell times for motor domain labeled GST-dynein fit to a convolution of two exponential functions with equal decay constants, with a rate of $k = 1.78 + 0.13 \text{ s}^{-1}$. Stepping data was acquired at 4 μM ATP every 100 ms. (i) Histograms of the 1-D and 2-D step sizes for motor domain-labeled dynein. The 2-D step size histogram reveals a peak at $\sim 14\text{--}16 \text{ nm}$, while the 1-D step size histogram has a peak that is slightly smaller. 78% of the steps are forward steps. $N = 2391$ steps. (j) An angle histogram of the step angles. The step angle is defined as the angle between the step vector and the direction of on-axis movement. Steps to the left or right of the direction of motion are between 0° and 180° , or 180° and 360° , respectively. Steps between 90° and 270° are backwards steps. $N = 2391$ steps.

Figure A1.3

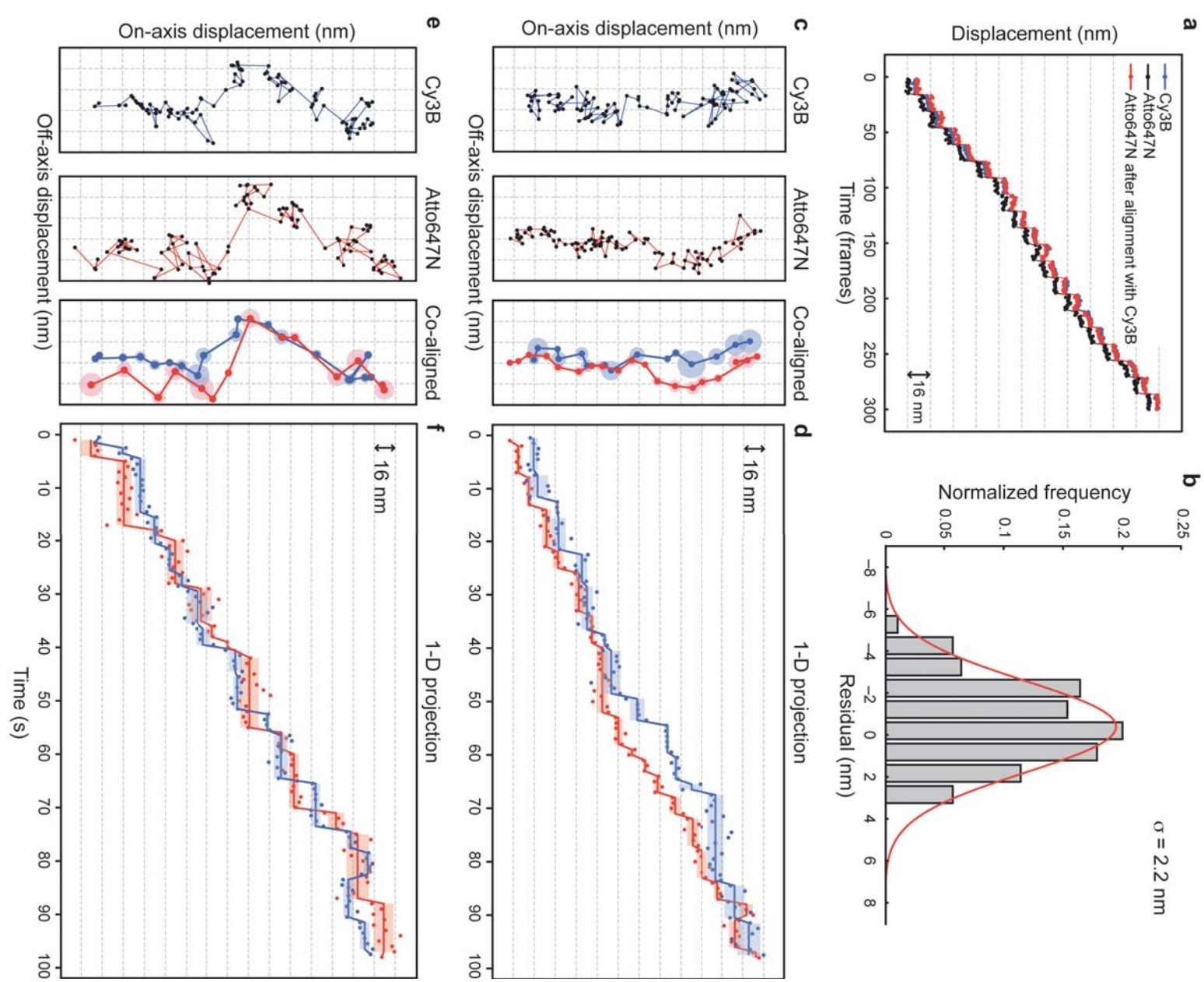


Figure A1.3 (continued).

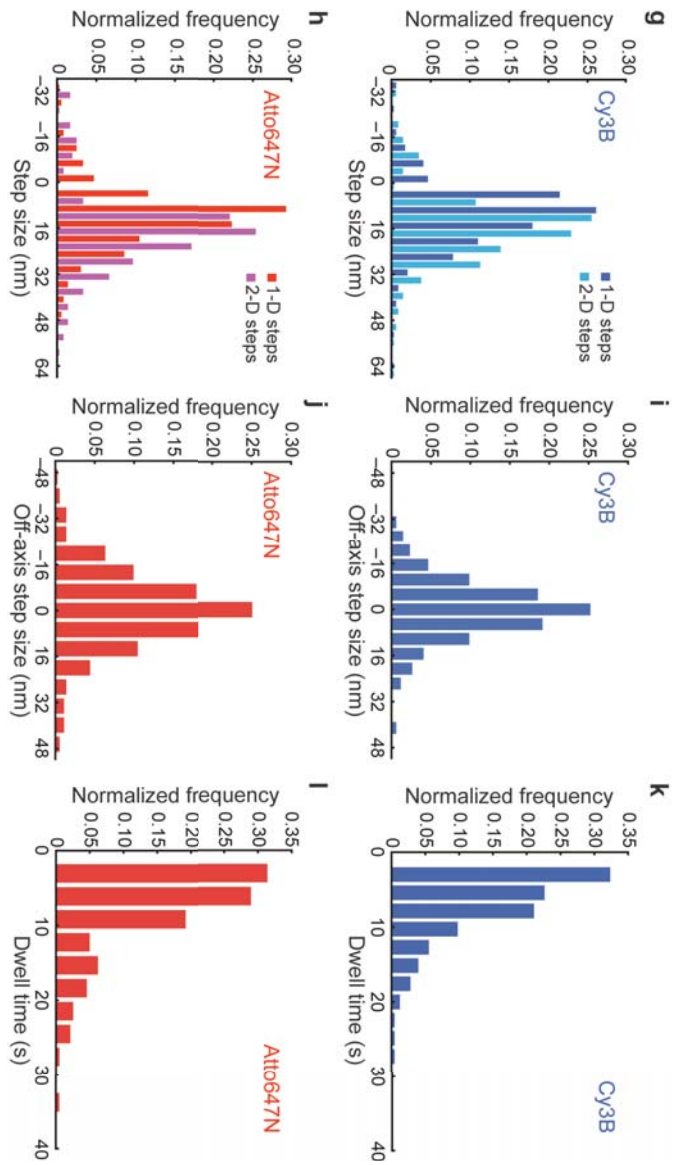


Figure A1.3 Two color, high-precision, single molecule co-localization of dual labeled dynein heterodimers. (a) Validation of the single-molecule, high-resolution, co-localization method. Three stepping traces of a tetraspeck bead (Invitrogen, 0.2 mm) attached to the coverslip and driven in a 8 nm staircase pattern via a piezo nanostage (MadCity Labs) are shown. Cy3B channel (blue) and the Atto647N channel before alignment (black) and after alignment (red). (b) Histogram of the mapping accuracy for the alignment in (a). The mapping error for this alignment is ~ 2 nm as estimated by the s.d. of the difference between the stepping traces from Cy3B and Atto647N after alignment using a 2 μm X 2 μm alignment grid (see **Methods**). (c-f) High-precision, two-color tracking of dynein stepping. (c,e) Representative two-color stepping traces of a DNA-dynein heterodimer. The raw 2-D positions (black dots in left and center panels) from a DNA-dynein heterodimer labeled with Cy3B (left panel, blue line) and Atto647N (center panel, red line). Co-alignment of the motor domain traces from each channel is shown in the right panel, with darker solid blue (Cy3B) and red (Atto647N) dots representing steps determined by a 2-D step finding algorithm, and larger, lighter-colored blue and red circles representing the s.d. of individual steps. (d,f) 1-D on-axis projection of the 2-D data from (c and e), with lighter blue and red bars representing the s.d. of individual steps along the projection axis. (g-l) Stepping statistics of the Cy3B- and Atto647N-labeled heads from the two-color experiments. 27 traces were analyzed for both channels. (g,h) Histograms of 1-D and 2-step size distributions. $N = 345$ steps (Cy3B); $N = 363$ steps (Atto647N). (i,j) Histograms of off-axis step size. $N = 213$ (Cy3B); $N = 254$ (Atto647N). (k,l) Histograms of dwell time distribution. Both distributions lacked a strong resemblance to a convolution of two exponential functions, possibly due to the fact that dynein's two motor domains do not always step alternately and/or because short dwells were under-sampled due to the time resolution of our method. $N = 257$ (Cy3B); $N = 247$ (Atto647N).

Figure A1.4

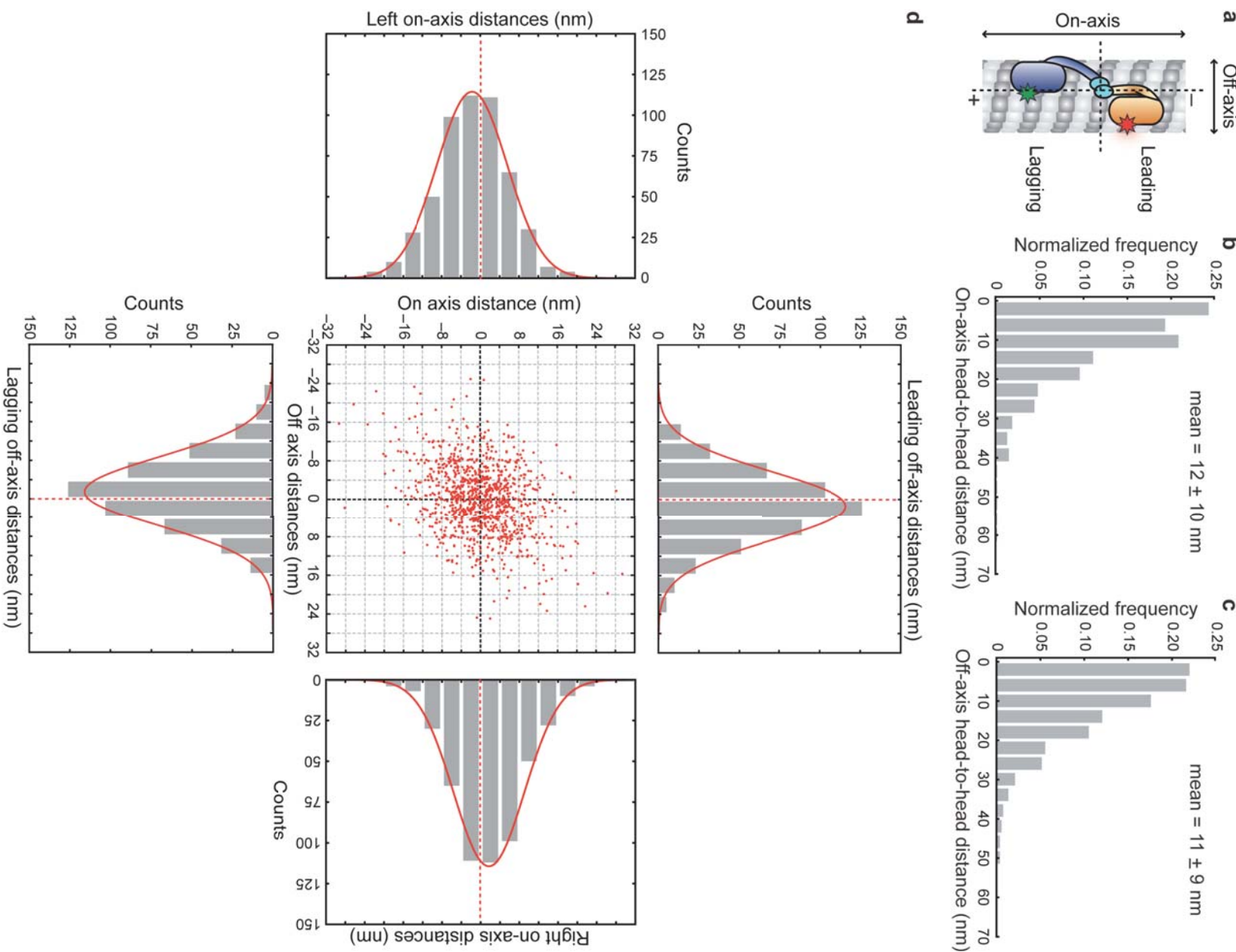


Figure A1.4 (continued).

Figure A1.4 Distance between motor domains in the on- and off-axis directions. (a) Schematic showing leading and lagging head positions and the on- and off-axis microtubule directions. (b) Histogram of the on-axis component of the head-to-head distance. $N = 523$. (c) Histogram of the off-axis component of the head-to-head distance. $N = 523$. (d) A scatter plot of the relative positions of dynein's two motor domains during the two-head-bound state. This plot is similar to Figure 5c, however here all data ($N = 523$ dimers vs. 256 dimers in Figure 5c), including data that did not pass the t-test for left /right or leading/ lagging position determination, are included. As in Figure 5c, the centroid position of each motor is fixed at the origin. Each head position is then plotted (red dot) relative to this centroid. The leading and lagging head off-axis positions are shown in the histograms above and below the scatter plot. These off-axis distributions are significantly different from one another (one-tailed t-test, alpha level of 0.05, $P = 6.7e^{-11}$). The distributions of left and right on-axis locations for all data points are shown in the histograms to the left or right of the scatter plot, respectively. The positions of the right and left head are significantly different from one another (one-tailed t-test, alpha level of 0.05, $P = 4.3e^{-14}$). Gaussian fits of the histograms are shown in red.

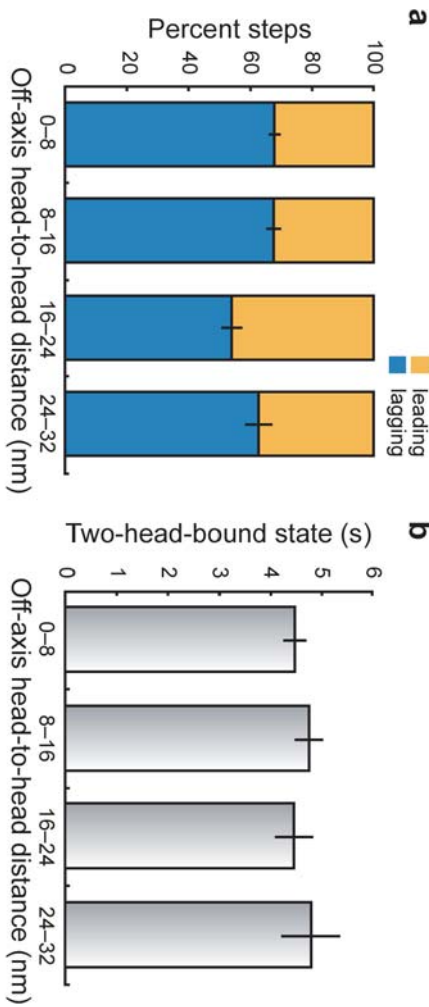


Figure A1.5 Effects of tension are not observed in the off-axis direction. (a) Relative stepping probability of the leading and lagging heads as a function of the off-axis head-to-head distance. Error bars represent the s.e.m. generated by bootstrapping each bin 200 times. No trend between head-to-head distance and the probability of a leading or lagging head stepping was observed. $N = 523$. (b) The duration of the two-head-bound state as a function of the off-axis head-to-head distance. Mean durations are plotted with the error bars representing the s.e.m. There is no statistically significant trend between the duration of the two-head-bound state and the off-axis head-to-head distance (two-tailed KS-test, alpha level 0.05). $N = 523$.

Table A1.1 Yeast strains used in this study

Yeast Strain ID	Genotype	Source
VY208	MATa <i>his3-11,5 ura3-52 leu2-3,112 ade2-1 trp-1 pep4::HIS3 prb1Δ pGAL-ZZ-TEV-EGFP-3XHA-GST-dyn1₃₃₁-Gly-Ser-DHA^a-KanR</i>	1
RPY897	MATa <i>his3-11,5 ura3-52 leu2-3,112 ade2-1 trp-1 pep4::HIS3 prb1Δ PAC11-13Myc::TRP pGAL-ZZ-TEV-DHA-dyn1₃₃₁</i>	This study
RPY1132	MATa <i>his3-11,5 ura3-52 leu2-3,112 ade2-1 trp-1 pep4::HIS3 prb1Δ pGAL-ZZ-TEV-EGFP-3XHA-SNAP^b-Gly-Ser-dyn1₃₃₁-gs-DHA-KanR</i>	This study
PY6431	MATa <i>pGAL1-6His-HALO-K1P3-LEU2(2μ) prb1-122 pep4-3 reg1-501 gal1 ura3-52</i>	2

^aDHA is the gene encoding the HaloTag (Promega). ^bSNAP and SNAPf are the genes encoding the SNAP-Tag (New England Biolabs).

Table A1.2 Oligonucleotides used in this study

Oligo ID	Modified oligonucleotide sequence
Oligo A-NH2	Amine - GGT AGA GTG GTA AGT AGT GAA
Oligo A*-NH2	TTC ACT ACT TAC CAC TCT ACC - Amine
Oligo A-NH2-biotin	Amine - GGT AGA GTG GTA AGT AGT GAA - Biotin
Oligo A*	TTC ACT ACT TAC CAC TCT ACC

Table A1.3 Dimeric dynein motors used in this study

Yeast strain and oligo	Labels	Experiment
VY208	Halo-TMR	Run length and velocity assays, one-color high precision stepping assays
RPY897-Oligo A-NH ₂ & RPY897-Oligo A*-NH ₂	Halo-Atto647N Halo-TMR	Run length and velocity assays
VY268	Halo-biotin	One-color high precision stepping assays
RPY897-Oligo A-NH ₂ - biotin & RPY897-Oligo A*-NH ₂	Biotin (on oligo)	One-color high precision stepping assays
RPY1132-Oligo A-NH ₂ & RPY1132- Oligo A*-NH ₂	Halo-Atto647N Halo-Cy3B	Two-color high precision stepping assays

References

1. S. L. Reck-Peterson *et al.*, Single-Molecule Analysis of Dynein Processivity and Stepping Behavior, *Cell* **126**, 335–348 (2006).
2. X. Su *et al.*, Mechanisms underlying the dual-mode regulation of microtubule dynamics by Kip3/kinesin8, *Mol Cell* **43**, 751–763 (2011).

Appendix 2

Supplemental Figures and Tables for:

Tug of War in Motor Protein Ensembles Revealed with a Programmable DNA Origami Scaffold

Nathan D. Derr, Brian S. Goodman, Ralf Jungmann,

Andres E. Leschziner, William M. Shih, and Samara L. Reck-Peterson

Contributions

Nathan Derr and Brian Goodman contributed equally. Nathan Derr initiated the project. Nathan Derr and Brian Goodman designed the experiments and performed all biochemistry, sample preparation, DNA origami folding, and single molecule motility experiments. Ralf Jungmann performed the DNA-PAINT experiment. Andres Leschziner performed the TEM experiment. William Shih designed the DNA origami chassis. William Shih and Samara Reck-Peterson provided mentorship. This work was published in: Tug-of-war in motor protein ensembles revealed with a programmable DNA origami scaffold, *Science (New York, N.Y.)* **338**, 662–665 (2012).

A

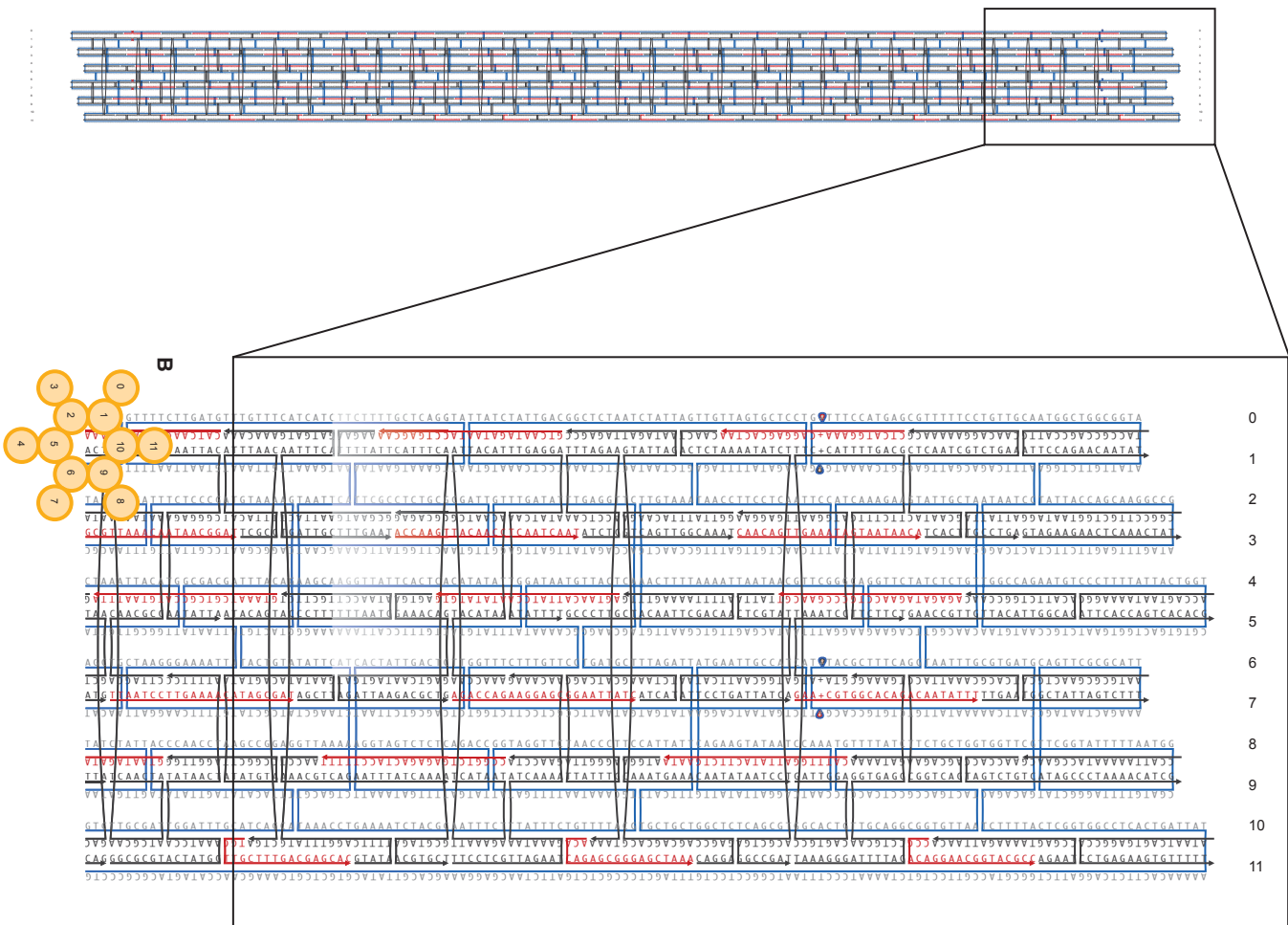


Figure A2.1 Twelve-helix bundle DNA origami chassis design. (A) Scheme of the chassis produced by the three-dimensional DNA origami design software, caDNAno ((*I*), www.caDNAno.org). The scaffold routing is shown in blue with gray sequence text. The core staples are shown in black with black text and the handle locations are shown in red with red text. Numbers refer to the helix designation and arrowheads indicate the 3' end of sequences. Boxed inset shows magnification of the chassis scheme. Because each handle sequence can be unique or redundant, the number and location of binding sites for similar and disparate motieties is controlled. Selective inclusion of handles in the folding process gives control over motor and fluorophore type, location, and stoichiometry on each chassis. (B) Cross-section of the chassis structure showing helix designation.

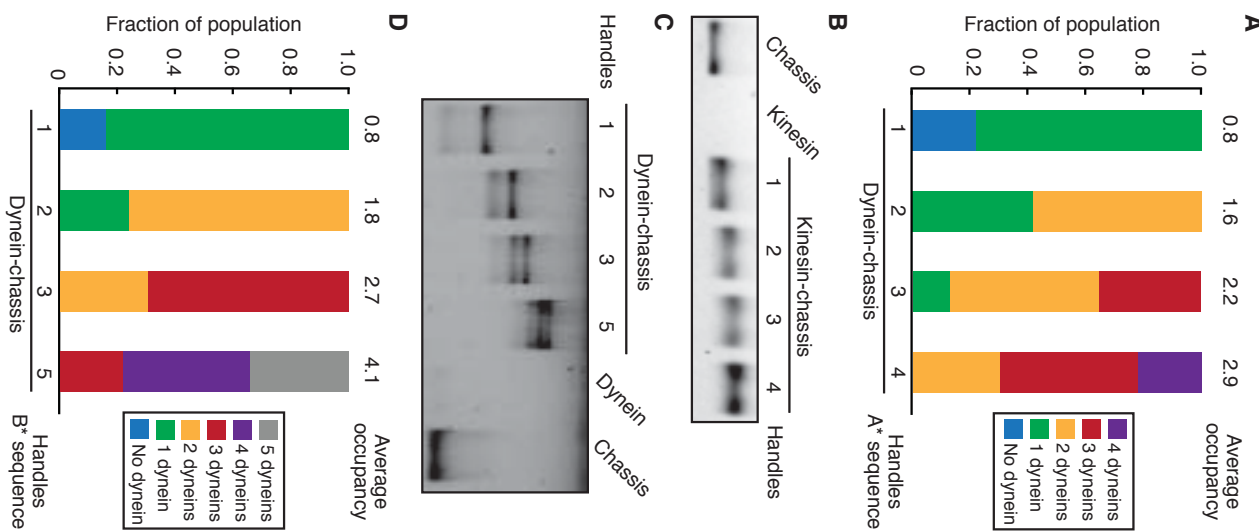


Figure A2.2 Characterization of motor-chassis complex formation. (A) Quantification of dynein-chassis complex formation from Fig.1C using the A^{*} handle sequence (table 3.4). The average number of dynein molecules per chassis is listed above the bar graph. (B) Agarose gel shift assay of TAMRA-labeled chassis containing 1–4 handles in the presence (right lanes) of kinesin labeled with an anti-handle oligonucleotide. Chassis alone is also shown (left lane). Chassis are visualized by TAMRA fluorescence. (C) Agarose gel shift assay of TAMRA-labeled chassis containing 1, 2, 3, or 5 handles in the presence (left lanes) of dynein labeled with the standard kinesin anti-handle sequence (B^{*}, table 3.4). Chassis alone is also shown (right lane). Chassis are visualized by TAMRA fluorescence. (D) Quantification of dynein-chassis complex formation from panel S2C. The average number of dynein molecules per chassis is listed above the bar graph.

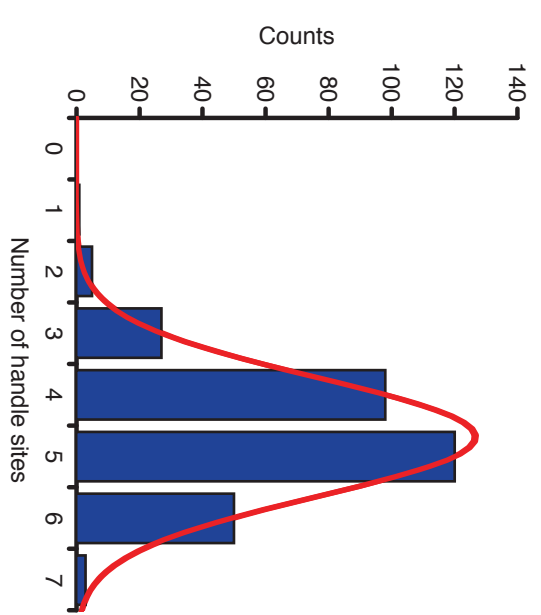
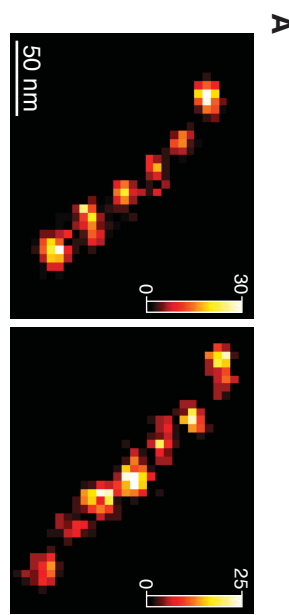


Figure A2.3 DNA-PAINT analysis of handle incorporation in the chassis structure. (A) Superresolved DNA-PAINT image of the 7 handle chassis showing 6 (left) or 7 (right) visible handle sites. The distance between adjacent sites was measured as 29 ± 2 nm (mean \pm SD, $N = 30$), as compared to the theoretical distance of 28.6 nm. (B) Distribution of handle site occupancy for a 7 handle chassis. The average number of handles was 5 ± 1 (mean \pm SD) and the incorporation efficiency of any given handle was measured as 72% ($N = 304$).

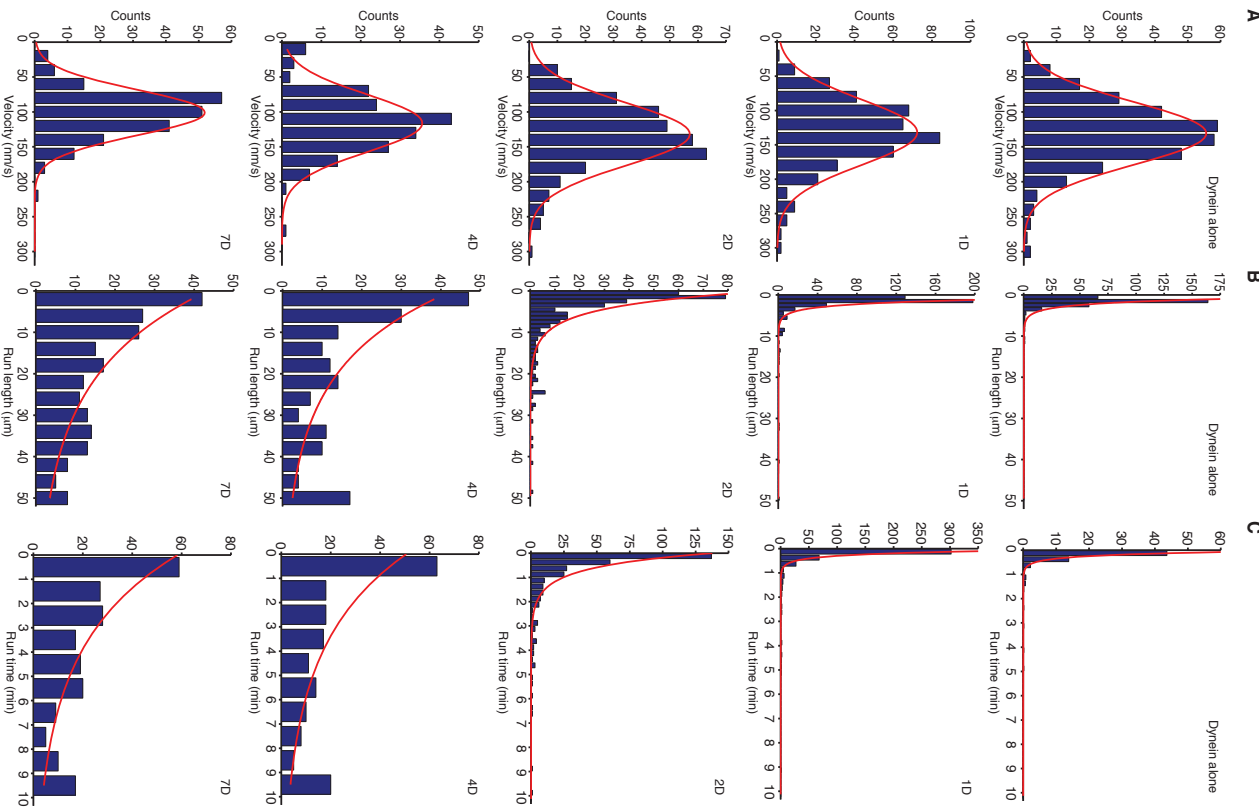


Figure A2.4 Velocity, run length, and run time distributions of dynein-chassis complexes. (A) Histograms of velocity for dynein alone and dynein-chassis complexes. Red line, Gaussian fit. The 4D and 7D ensembles moved significantly slower than dynein alone, or the 1D or 2D ensembles (one-tailed t-test, $P < 0.001$; $N \geq 211$). (B) Histograms of run lengths for dynein alone and dynein-chassis complexes. Red line, single exponential fit. All pair-wise run length data were significantly different (two-tailed KS-test, $P < 0.01$; $N \geq 208$) except the 4D and 7D standard ion concentration run lengths (two-tailed KS-test, $P > 0.05$). (C) Histograms of run times for dynein alone and dynein-chassis complexes. Red line, single exponential fit. All pair-wise run times were significantly different (two-tailed KS-test, $P < 0.001$; $N \geq 208$) except the 4D and 7D standard ion concentration run times (two-tailed KS-test, $P > 0.05$).

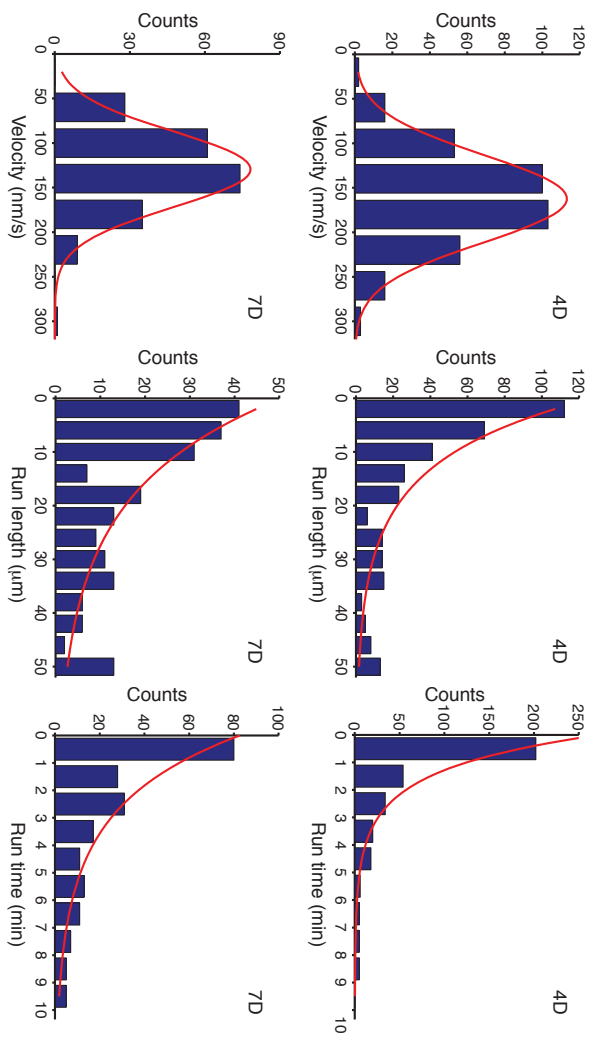
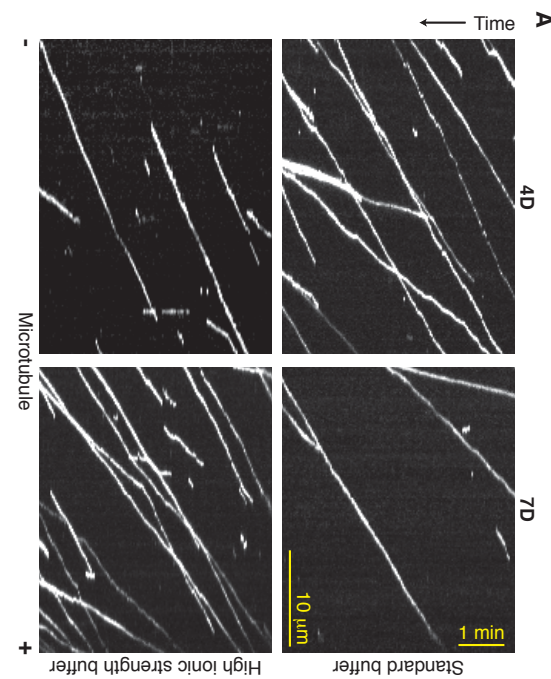


Figure A2.5 Single-molecule motile properties of 4D and 7D chassis as a function of ion concentration. (A) TAMRA-labeled chassis with 4 (left) or 7 (right) dynein attachment sites were analyzed in buffers containing 50 mM potassium acetate (standard buffer, top) or 50 mM potassium acetate + 100 mM KCl (high ion concentration, bottom). (B) Histograms of velocity for dynein-chassis complexes in higher ion concentration. Red line, Gaussian fit. In higher ion concentration (\uparrow 208), the 4D and 7D ensemble velocities were significantly different (one-tailed t-test, $P < 0.001$; $N \geq 208$). (C) Histograms of run lengths for dynein-chassis complexes in higher ion concentration. Red line, single exponential fit. (D) Histograms of run times for dynein-chassis complexes in higher ion concentration. Red line, single exponential fit.

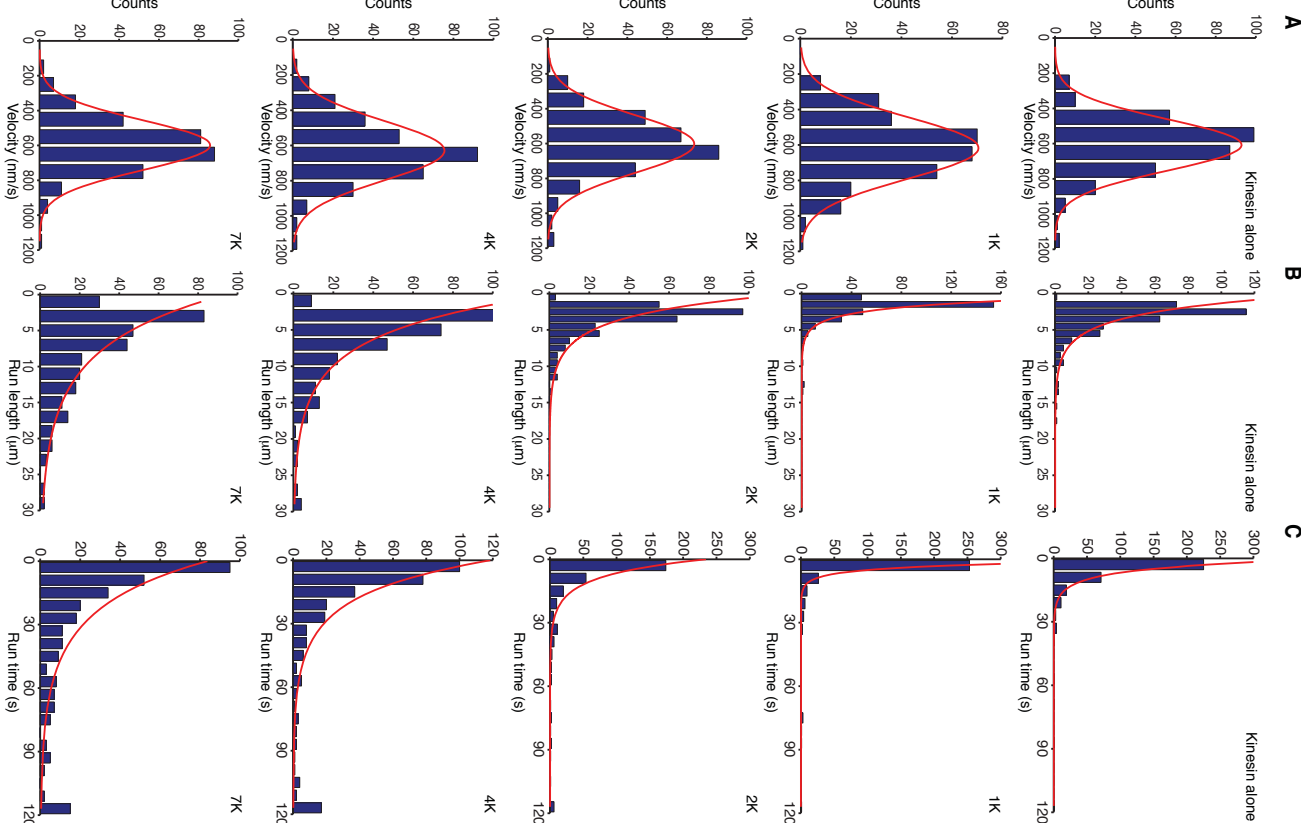


Figure A2.6 Velocity, run length, and run time distributions of kinesin-chassis complexes. (A) Histograms of velocity for kinesin alone and kinesin-chassis complexes. Red line, Gaussian fit. Comparison of velocities yielded no statistical differences (ANOVA test, $P > 0.05$; $N \geq 301$). (B) Histograms of run lengths for kinesin alone and kinesin-chassis complexes. Red line, single exponential fit. All pair-wise run lengths were significantly different (two-tailed KS-test, $P < 0.05$; $N \geq 301$). (C) Histograms of run times for kinesin alone and kinesin-chassis complexes. Red line, single exponential fit. All pair-wise run times were significantly different (two-tailed KS-test, $P < 0.05$; $N \geq 301$) except the 4K and 7K chassis (two-tailed KS-test, $P > 0.05$).

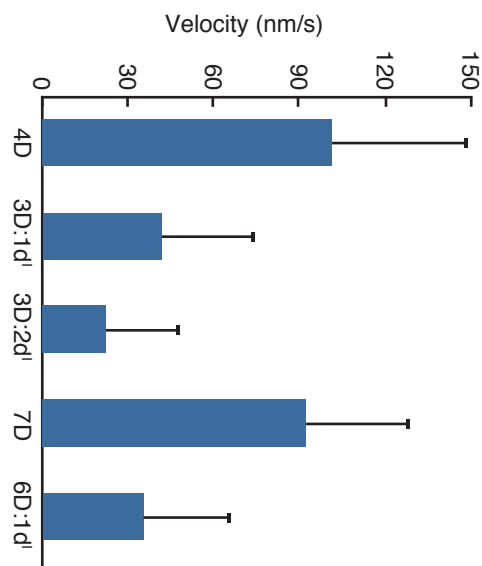


Figure A2.7 Inactive motors decrease dynein-driven chassis velocity. Quantification of the average velocities \pm SD of 4D, 5D, and 7D ensembles with (3D:1d^l, 3D:2d^l, and 6D:1d^l) or without (4D and 7D) a dynein mutant present on the chassis ($N \geq 207$). The 3D:1d^l, 3D:2d^l, and 6D:1d^l ensembles move significantly slower than the 4D and 7D ensembles (one-tailed t-test, $P < 0.001$). The 3D:2d^l is significantly slower than 3D:1d^l ensemble (one-tailed t-test, $P < 0.001$).

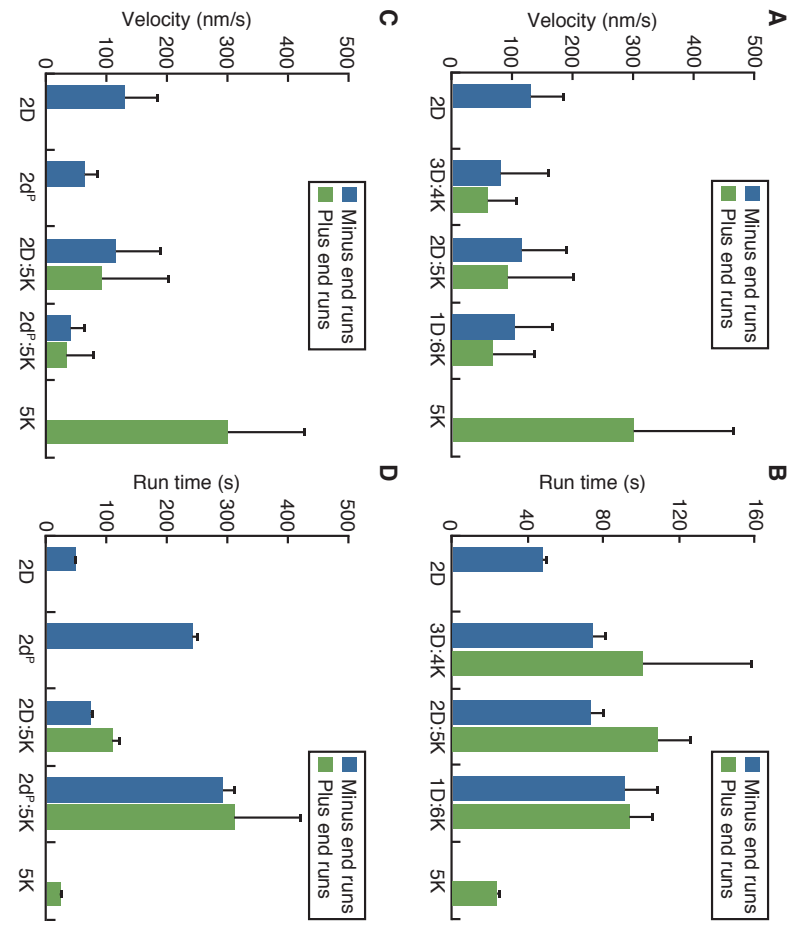


Figure A2.8 Velocity and run times of mixed motor ensembles. (A) Average velocities \pm SD of chassis moving towards microtubule minus ends (blue) or plus ends (green). All mixed motor chassis runs are significantly slower than the dynein- or kinesin-chassis controls (2D and 5K, respectively; two-tailed KS-test, $P < 0.001$; $N \geq 253$). (B) Run time \pm SE of chassis moving toward the minus ends (blue) or plus ends (green) of microtubules. Run times in both directions of a 2D5K chassis are significantly longer than either of the single motor run lengths (2D and 5K, respectively; two-tailed KS-test, $P < 0.05$; $N \geq 253$). (C) Average velocities \pm SD of chassis containing the dynein mutant with high processivity (d^P) compared to wildtype dynein mixed chassis. The mutant dynein ($2d^P$) mixed chassis is significantly slower in the both directions than the wildtype containing chassis (two-tailed KS-test, $P < 0.01$; $N \geq 253$). (D) Run times \pm SE of the chassis containing the highly processive mutant dynein (d^P) compared to wildtype dynein mixed chassis. The mutant chassis remains bound to the microtubule significantly longer compared to the wildtype chassis (two-tailed KS-test, $P < 0.01$; $N \geq 253$).

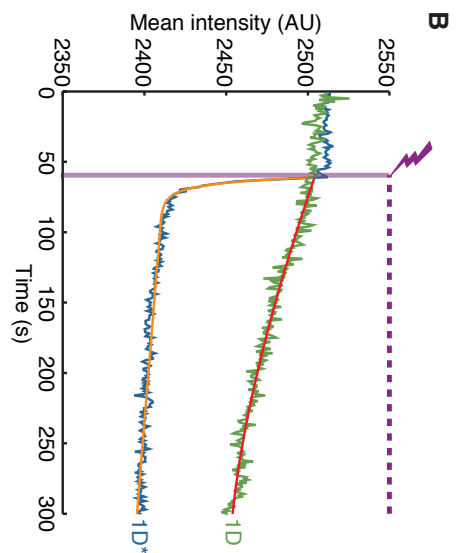
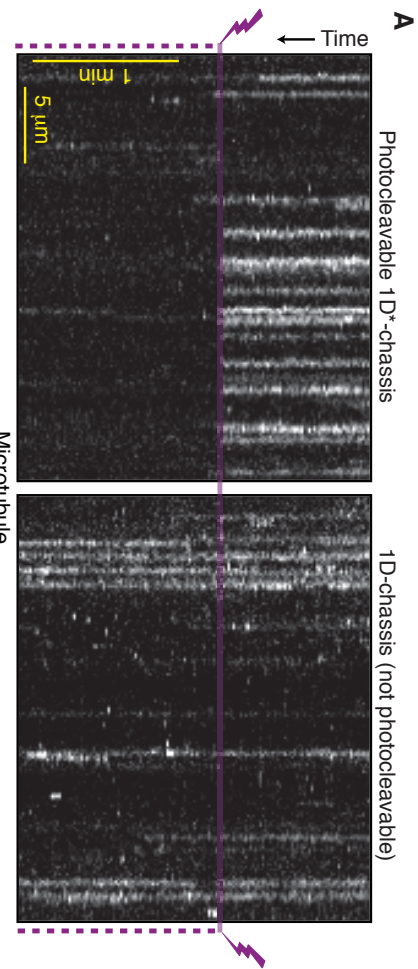


Figure A2.9 Photocleavable handles can be used to detach motors from chassis. (A) Chassis bearing 1 photocleavable dynein handle (1D*; left) or a non-photocleavable dynein handle (1D; right) were immobilized on microtubules in the absence of ATP. After 1 min, laser pulses began (purple lightning bolt and lines). (B) 1D (green) and 1D* (blue) chassis were non-specifically immobilized on a coverslip and imaged as in panel A. In the absence of attached dyneins, negligible sticking of chassis to the coverslip was observed. The mean fluorescence intensity vs. time is plotted. Purple lightning bolt, time of photocleavage. Red line, single-phase exponential fit with a decay constant $6.0 \times 10^{-5} \pm 0.7 \times 10^{-5} \text{ s}^{-1}$. Orange line, 2 phase exponential fit with decay constants of $0.21 \pm 0.02 \text{ s}^{-1}$ and $1.6 \times 10^{-5} \pm 0.5 \times 10^{-5} \text{ s}^{-1}$.

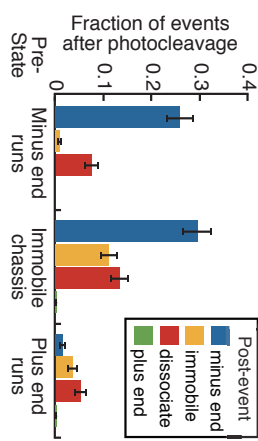
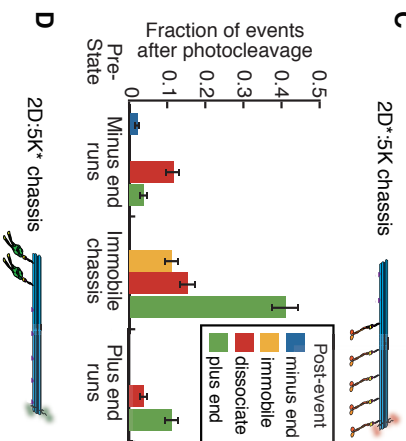
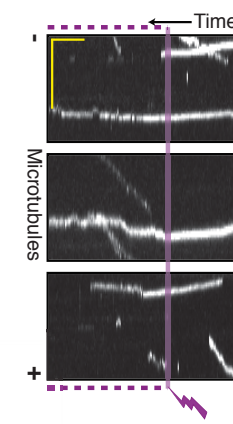
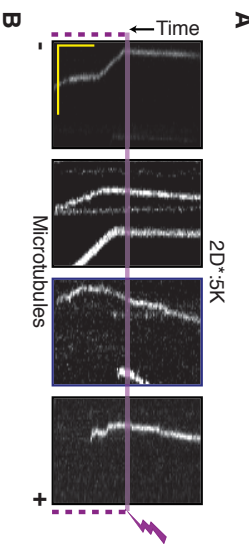


Figure A2.10 In rare cases, photocleavage induces chassis to switch directions. (A) Examples of 2D*.5K chassis switching from minus- to plus-end-directed motility. Purple lightning bolt indicates start time of photocleavage. Scale bars, 5 μ m and 0.5 s. (B) Examples of 2D:5K* chassis switching from plus- to minus-end-directed motility. Purple lightning bolt indicates start time of photocleavage. Scale bars, 5 μ m and 0.5 s. (C) Quantification of the motile properties of 2D*.5K chassis after photocleavage as a function of their pre-state ($N = 286$). Fractions are calculated as the number of events observed as a fraction of all possible events regardless of pre-state. (D) Quantification of the motile properties of 2D:5K* chassis after photocleavage ($N = 304$). Fractions are calculated as the number of events observed as a fraction of all possible events regardless of pre-state.

Table A2.1

Core staples to build the twelve-helix bundle. These staples were used in every structure.

GTAATGTTAGGACATTTG
CGGCCGCCAGTCTGGGCCTGGA
GCTGACCATCAATAGCATTGACAA
AAATAATATAAACCTGTAAT
ATAGTACATAACCTGGATAAGAG
TGCTCTGATAAAGACCTCAACA
GTTGAAGGAATACAAACAAACACT
AAACACTGCCTAGAATAGGTTTC
AGAATGATAGCACACCACCTGTA
CTATCGAGCAAGACTCCCTTAGA
GTTAGGAACAAGCTTAATCAAGT
ATACCCCTCTGAAACGCTCAATC
TCGCCTTACATATTAAACCTGA
ATCTGACCTCAATTAGAATAAA
AGAATCCGAGTAAAAGATAACA
CTTCATAAATCGTAGCTTAACCTCAC
GGGTCTTCTGCTCTCGCACTCAATC
GTGAGCTGTAGATCGAAACGTACAG
TAATGGGGGTAGTCGGCTCTGGCC
TCAACTTTGCGGTATGACCTGTA
AAGCGGATTAGGAACGAAAGACTTCA
CGTTGACCAAAGTAATGCGATTAA
GCACCAAAAGCGGAGTCATTAAACGG
ATCTAGAAACAGTGGTAGCATTCCAC
GTTCCCGGAAGGCCGTAAAGCCAGAA
AGGTGGACCACAAAGGGAGGGGAAGGT
GAAGCAAGGTAAATAGCAGCCTT
AAAAAAACTTTCCGGCCTGTTA
AACCTAACGTCAGAATTATCAAAA
ATGGACAAATGAAACAAATATAATCCT
TCTGTTGAGCCTTACAGACGATCCAGCG
GTTAACGGAACGGGAAAGCCGCACAGG
TTCTGTTACGCCACTTCAGGAAGATGGCA
CTACATGTACCCCCATAAATGCGCG
TAACATTTCATGCAACTAAAGTAC
GATAAACTGCGGATAAGAGCAACACTAT
ATAAGAATCTGCCCATGTTACTTAGCC
TGTATACGCATAAAAATCTCCAAAAAA

Table A2.1 (continued).

TAGGGTACTCACCTGAAAGTATTAAGA
TCGGCTCCCTCATCCAAGTTGCCCTTA
GAACATAIGTTAAATTACCGAAGCCCTT
GAAGGTGCTTAITAGAACATTACCGCGC
CGGAGCTTAATATGACCGTGTGATAAA
GCGAATGAATTACTTGATGCTTGAAT
GGTTATTACAAGAGTCAGTTGCATAAT
TCCCAGTCGGTACATGGCCTGTGCAC
GTGCCACAGCGTGACATGAAGGGTAA
GCATTCCGGCTGCAATTTCGGCACCGC
TAGCCCCCAAACCTTTGAGAGAT
TTACCTGGGTGGCAGGTTCATCCATA
ACGAGATTGAATCCGATTACCGAC
GAACGTTACCCAAATAGACCGCTTAAT
CCCAATTGAGGCTTACGGAGCAGAC
GACAGAACCTCAGAACAGAGAAGGA
AATAGCACGCCACCGAACAGCGGTTTCA
AGCCAATACATAAATTAGCAGATAGCC
AAAAGACTATCCTGTTAAATCAGATATA
CTTAGCACACAACCAATAAGAATAAAC
AAACCAATACATAAACAAATCGCGCAGAG
GTTTTATGGGATAGACGTTAGCAAG
GTAAGATGTAATCCATGGAATTGAGGA
GGCCGGGGTGTGCGGCTTACACTGGCCAG
ACCGGAACGATGCTGATTAGGGATGCTGATT
TCGCATGTGCCGAAACCATGGGATAGCGGTC
GTCTGTAAGGCTATCAGGTAGGGTATGGT
TAGATTAGTTGATTCCAACTTGAAGAATAG
CAAAATAAACCAAATAGAACGATTCCAAGAGT
GAGGAGTGGAACCGGAACCTGGATTAGCGAAAA
GGCGGCCATTAGCGGGGTCGGGTCACTAAT
GCGTTCCATTTCGGTCATTAGCACCACGGGA
ACGCAAGAAGTACCAAGAACATAATAGCGAAA
GGCGTGTCTTACCGGTATCCTTATCCACGCTG
TTAGTGGATCATTAATTACTGACAAAGGCTACAG
AAGAATTATTCTATTCACTGAGGCTACAG
CAACTACTCTAAATATCTACGCTGAGGCCAT
CGGTGGCTGCCGGACTTGTGCAACCGCAAGAAT
AACGTGCATGCTGGCGAACGGGCCAGGTTTCC
TGGTCAAATCGGGTGTAAATCGCAAATTTAAAT
AAAATTGCTTGGGGCGCGAGGTTAGCATTAAACATC

Table A2.1 (continued).

AAAATGCAGAACCGTCATAAAGTCAGAAACGA
GAATCATCGACAAGAACCGGACTTCAGTGAAT
AGAACAACTACCGATATTCCCTTTGGGGATCG
GGTAATGCCGAGGTTAGTAGCCACCTCAGAGC
CGAACACCAGAGCCCACCCAGAGGCCACCCAG
TCAATAATGCAAACGTAGAAAAACGCCAAAGACAC
ACCTCATCGTGCACCCAGCTGGCGTCTTCCAG
AATAATTCTGAGAACATGCCAAGGCATTTCGAGC
ATACAGTACCTTTTAATGATAACCTTGCTCT
GAAACCGTTGTTACATTGCAGACATTCTGGCCAAC
GGTGGTTTCTTGTCATAAGTAATGGGGTGCA
GCCCTTCACCGCCTAGAGACGGTGAAGGACGCCA
CACCGCTGGTTGCCGCGGATTGTCGGATAAAATC
GGTCCCGAAATCGGATGCCCTGAGAACCCCAAGAA
CCCGAGATAGGGTTACCTTACTCCAACCAGGTCT
CCACTATTAAAGAATTACAATAAACACCGAGA
ACCGTCTATCAGGGTTGACCAAAGAACCATCG
CGGAACCCCTAACGGTAATAACTTTGACAGCATT
AAGCCGGCGAACGTAGCAAACCTTGAGGCCACAATC
GGAGGGGGCGCTAGAGGGTAAACTGAAATAAAC
CGCGTAACCAACCAATCGGCTACGGAGCTACCGAC
GGCGCGTACTATGGAATCCATATAACTTTCC
TTCTCGTTAGAATAATCAAAAAACAAAG
TAAGGGATTAGCCTGCAAGGTGAGGTGAAAGC
GTAATGGATCCCGCTAATGAGTTAAGTGTAAAGCCTG
GAATTCCCGGTTATCAGCAACAACTATCACCCAAATCAA
TCACTGCAATAACCTCAATCGTCTGAACACAGGAAACG
CAGCAAGAACGTTGCAGGCCCTATCAGCATCAGGGG
GGTAAGGGATGTGGAACAAACATCAGGGGAACGGATAACCT
TATAAAGAAAAGATCAAACATATAAACCATAAGGAA
TAGTACTGAAATACCAAAACATATAAACCATAAGCTAACCG
TAAACTATTCATTAAGAGGAAGCCTAGGGATTGCATCAA
AGCTGTATTCTGTAATTACCTCAATTCAACTTTAAT
GGCGGGGTGCGCTCATGAGGAAGTTGGAGGACTAAAGACT
GAACCCCGCCACACTACAAACGCCCTCCGTTCGTCACCA
CCCTCTCAGAACATAATCCTCAGACCTTGATATTCA
AAAAGAACATCAACCGATTGAAAAAGACAAAGGGCG
CTAACACAAATTGTCAAAATGAAAAACGATTTCGTT
GGCAGTATTAGCTAACGAAACAAATAACACATG

Table A2.1 (continued).

AGTGAGAACAGGAGTCAATAGTAGATTAAAGACCGCTG
TATTACTCGTATATGGCAATTCTGATTATCA
GGTGTTCGCCGCCAGCAGTGTAAAGGACTGTGCCCTGCG
CCACGGCGCATCGTAACCGGATAGCTAGATAGACTTTCTC
ATTTAGGCCGAGACATTCTCCGTGTGAGCGAGTAACA
AGAGCGGCTTAGAGCTGGTCATATAGCAAGGATAAAAT
AAAGCCCACATCAACTATAGTCAGAAGAACCGGAAG
GTTAACGGAGATTGTAACGAACTAGGAAGAAAATCTA
GCTTTAGAATAGAAAGGACATACACTAACCTAAACGAAA
ACTGACGTATAAACAGTGAAGTAATAAGTTTGTGCT
ATTGGAACGTCACCAATGCTGATAACAAGTAAGCGTCATAC
CGCCATGTAGTTAAGCCGTCAATTGGAATTATCACCGTC
TAAGACCAAGTACCGCAAACACCCCTGGCATTAGACGGGAG
GACGAATATATTAGTAGATGTAGATAATATCCCATCCT
AGCTGAAATACAGTATAATATGTACCGGCTTAGGTTG
ATCATTCTAAAGCATCAGGTTATTGAGGGTTAGAACCTA
TGAAATCACGCAAATTACCGGTCAAGAGCAGAAGATAAA
CAACACAAACTTAATTCTCATGTCCGTTTCG
CAGCAAGGTACCGTGGCACTCGCTCATCAGGCTGGC
CTGTTAAAGATTCAAAGATCAATCAGAGCAAACAAGAGA
TCAAATAAGAGGTCAATTAGCTATTAGTTGACCATT
TGGAATCAGTGTGAGATTGCGCCAGAAGTTTGCCAGA
AAAGGCCAAGCGCGAAAGGATCAAGACAGATGAACCGGTGT
GAACCTTCAACAGTTCAACCACATCGCTCTAACACAGCTG
AAAGCAGTGCCTTGAGTTGATCAATAAGTGCCGTGA
GCTTGATTACCATAGCAGGGAACCGTGCATTTCAT
AAGAACAGAGATAACATATTACGCATAATAACGGAAATA
GCGGTATTCCAAGAACGCAAAGATTATTAGCGAACCTCC
GCGCCAACCGGAGAAACCAACAGTAATCATATGCGTTAT
GTATATTTCAGGTTATGAATTTCAGATGTGAACAA
CAGGAGAGCCAGCACGGTATTAGAATAGATTAGAGCC
ATTAATGACATCCCCAAGCCTCCGGCCACATCGACCGACCGT
CGCCCGTGCAGAACGGGGCGATCGGGTGGGGTTGTAA
CGCCACCGACCGTAAGTAATCGTAAACTATGATAGGTATT
TTCCTTGTAAATGCTCAAATGGTCAATGCTGTAGAACAGGC
ATACTAAATTGCTCTAAATGTTAGAGCCAAATCATCAA
ATATTTAGGTAGACGCATAGGCTGGCTTGTGCCCCGACGA
GAACTGGCCCCAGCACGCCGACAATGGGAATAATGCGAA
GTAAACCTTGCTATTAGTAGCCGTTCGGGAGGCTTCA
AGACAGGGTTAATTGGAAACCAAGAGCGCACCGTACAGCCG
TGGAAGATCACCAAGGGCATGATAAGAAACAACTTATT

Table A2.1 (continued).

AAATATTTGAGGGGGTTTGAAGCCAAGCCGTGGCAGTT
TACAGTTGTCTTCCAGTATAAGCCCCATAATAAATAT
TCAACTAATCGCAAAGAAAATTACCGGGAGAAATATA
TCATAATAGAAATTACATTGAGGAATATCAAAATATT
GATTGGACAGTGCTTCTACATTGACGTTCTTGTCT
ACCAGCACGCCAGCGGTGA
ACCGGTGCCCTGCATCCTGCAGCTGTCTATCGGCCAACGCA
GTCATAGCTGTTCTGTGAA
AAATTGTTGGGGTCACAGTTGACATG
ACACACAAACATAAGCCCGGA
AGCATAAACGGCATCAGATATTGCATTACAGTCGGAACCTGTA
ACCTCCAGCCCTCACAAATTCA
TCAGCGATCGCGTCTTCACCGTCATACGGGGTTCTGA
AGCGGGAGAGGCCGTTGCGTATTGGGTGTGT
ATACCGCCAGCCATTGATCCAGAACATA
ACGGCCCTGCTGTAATAGGATTATATGCCTGA
GTAGAAGAACTCAAACATATA
AACCAAGTAATAAAAGGGATTACCCAGTCACACGA
AAATGGCGCGAACTGCATGGCTATTAGTCTTA
AACCACCTAGTGTCATAGCCTAAACATCGA
ACCATTAAAATACCGAACG
AATAATCAGTGAGGCCACCTGAGAAAGTCTTAA

Table A2.2

Negative handle staples used to build the twelve-helix bundle. Any of the following staples can be made into a handle by appending a handle sequence onto the 3' end of the staple. Every handle staple site in the chassis must be occupied by either a negative handle or a positive handle.

Handle site helix0, #0	CTCGTTCGCTGGCGAATGCCGC
Handle site helix0, #1	AACTGTGGAACCGTCCGGCAA
Handle site helix0, #2	ATCGATGAACGGCAAAGGCCA
Handle site helix0, #3	AGATACATTGGATTGCCGTGAGA
Handle site helix0, #4	GGGGTAATAGTCTGGAACGAG
Handle site helix0, #5	ACAGACCAGGCGAGAGGCTTTG
Handle site helix0, #6	ATACCGATAGTCAACTTTGAAA
Handle site helix0, #7	GAGGGTGATAATGCTTCGAGGT
Handle site helix0, #8	AATCAAATCACGCTCAGTACCA
Handle site helix0, #9	CCCAAAAGAACCCCCCTATTA
Handle site helix0, #10	CGACTTGGGGAAACCGAGGGA
Handle site helix0, #11	ACAAATTCTACTAAGAACGGGA
Handle site helix0, #12	CATCAAGAAAACAAAAAGCCTGT
Handle site helix0, #13	GTCAATAGATAATACCTGAGCAA
Handle site helix0, #14	CTCATGGAAATACAGGAGCACTAA
Handle site helix3, #0	CAGTGTCACTGCAAAAAATCCC
Handle site helix3, #1	CGGCCTTAGTGGACGACAGTAT
Handle site helix3, #2	CTCCAGCCAGCTCAACCGTTCTA
Handle site helix3, #3	AGAGGGTAGCTACAACCATGTT
Handle site helix3, #4	GGTGTCTGGAAGAATTACGAGGC
Handle site helix3, #5	CATAACCCCTCGTAATCCGGGACC
Handle site helix3, #6	GGAACGGGGCGCAATTTCAC
Handle site helix3, #7	AAGGCTCCAAAACTATTCTG
Handle site helix3, #8	GGCTGAGACTCCTCAGTAGCGAC
Handle site helix3, #9	GCGTCAGACTGTAATAGCAATAG
Handle site helix3, #10	TTAAGAAAAGTTATTCATC
Handle site helix3, #11	CCAATAGCAAGCAATGGTTGAA
Handle site helix3, #12	TAAGGCGTTAACAAACGGAT
Handle site helix3, #13	ACCAAGTTACAAACCTCAATCAAT
Handle site helix3, #14	CAACAGTTGAAATAGTAATAACA
Handle site helix4, #0	GCCAAACGGCAGGCAGCTCGAATTG
Handle site helix4, #1	CAGTCACGACGCTGCTGGTCTGGT
Handle site helix4, #2	TGTAACGTTAACGATTAAGTGTG
Handle site helix4, #3	CAATAATCATACAGGAAGATG

Table A2.2 (continued).

Handle site helix4, #4	GAATGACCATAAAATTCTACTAA
Handle site helix4, #5	AAGGCCTGCCCTCTCAAATGCTT
Handle site helix4, #6	TCACCCCTCAGCACAAACGTAACAA
Handle site helix4, #7	CACCACCTCATAGGGAGTTAAA
Handle site helix4, #8	AACCAACCAGGCCACCTCA
Handle site helix4, #9	CACGGAAATAAGTCAGAGGCCACCA
Handle site helix4, #10	AGCCTAATTGCTGCCAACATAT
Handle site helix4, #11	CAGTAATAAGAGTCTTACCAACG
Handle site helix4, #12	GTAATCGTCGCCATGTAATTAA
Handle site helix4, #13	AGTAACATTCCAATATAATGTG
Handle site helix4, #14	AGAGATAGAACCTGCCGAACGT
Handle site helix7, #0	GGCGCAACCGCTTACGGCTGGA
Handle site helix7, #1	GTAAGCTTTCAGAGGGAGCCG
Handle site helix7, #2	CAAATTTGTTAACATCAGCTC
Handle site helix7, #3	CGAAATAAGCAATAAAGCCTC
Handle site helix7, #4	GTCCTGACTATIATAGTCAGAACG
Handle site helix7, #5	AGTAGTAAATTGGCTTGAGATG
Handle site helix7, #6	CAAGGGTAGCAACGGCTACAGAG
Handle site helix7, #7	TTAGGAACCCATGTACCGTAAC
Handle site helix7, #8	ACGAGGTTGAGGCAGGGTACAGACG
Handle site helix7, #9	AAAAAATTCATATGGTTACCAAG
Handle site helix7, #10	ACTATTATTATCCCACCAAA
Handle site helix7, #11	TAGTAAAGTAATTCTGTCCAGAC
Handle site helix7, #12	TTAACCTTGAAACATAGCGAT
Handle site helix7, #13	AGACCCAGAAGGAGCGGAATTAC
Handle site helix7, #14	GAATACGTGGCACAGACAATT
Handle site helix8, #0	GCTTGGCGTTGGCTCACTGCCG
Handle site helix8, #1	CGGGCGCGGTGCGGTATGAGCC
Handle site helix8, #2	ACTGTTTACCACTCCCCGAATT
Handle site helix8, #3	ITGTAGGCCAGCTTCAACAT
Handle site helix8, #4	CATTTGGGGAGAAGCCTTATT
Handle site helix8, #5	CGCGCGTTTAAATTGGCTTC
Handle site helix8, #6	GAGGCTCATTACCAAGTCAGGA
Handle site helix8, #7	TTATACGTAATGCCACTACGAAG
Handle site helix8, #8	ATGCCCTCATAGTTAGCGTAACG
Handle site helix8, #9	CCAGGGCAGTCTGAATTAC
Handle site helix8, #10	AATTGACGGAAATTATTCATTAA
Handle site helix8, #11	AAAGAGAATAACATAAAACAGG
Handle site helix8, #12	GTAATAGATAAGTCCTGAAACAAG
Handle site helix8, #13	CCGGTCTGAGAGACTACCTTT
Handle site helix8, #14	CATTGGATTACTTCTGAATA

Table A2.2 (continued).

Handle site helix11, #0	CTCTCACCCAGTGAGACGGG
Handle site helix11, #1	AAAGGCCCTGAGAGAGTTG
Handle site helix11, #2	ACGCCAGCAGGCAGAAATC
Handle site helix11, #3	GCACAAATCCCTTATAAA
Handle site helix11, #4	AGTGAGTGTGTTCCAGTT
Handle site helix11, #5	ACACCGTGGACTCCAACGTC
Handle site helix11, #6	CATCGATGGCCCACTACGT
Handle site helix11, #7	TGTGGGGTCTGAGGTGCCGT
Handle site helix11, #8	CTGGAGCCCCCGATTAGA
Handle site helix11, #9	GCGGGCGAGAAAGGAAGGG
Handle site helix11, #10	CAGGGCGCTGGCAAGTGTAA
Handle site helix11, #11	AATACCCGCCGCCCTTAAT
Handle site helix11, #12	TGCTTGCTTGTACGGAGCAC
Handle site helix11, #13	ACACAGAGCGGGAGCTAAA
Handle site helix11, #14	CCGACACAGGAACGGTACGCC

Table A2.3

Positive handle staples used to build the twelve-helix bundle. Sequences in italics indicate handle portion of the staple. PC, photocleavable linker. PAINT, handle staples used for DNA-PAINT.

Handle site helix0, #1-A	<i>AACTGTTGGAACCGTCCGGCAA</i> <i>TTC ACT ACT TAC CAC</i> <i>TCT ACC</i>
Handle site helix0, #3-A	<i>AGATACATTTCGATTGCCTGAGA</i> <i>ATC ACT ACT TAC CAC</i> <i>TCT ACC</i>
Handle site helix0, #5-A	<i>ACAGACCAGGCCAGAGGC</i> <i>TTTG TTC ACT ACT TAC</i> <i>CAC TCT ACC</i>
Handle site helix0, #7-A	<i>GAGGGTTGATATGCTT</i> <i>CGAGGT TTC ACT ACT TAC CAC</i> <i>TCT ACC</i>
Handle site helix0, #9-A	<i>CCCCAAAAGAAC</i> <i>TCCCCTATTATTC ACT ACT TAC CAC</i> <i>TCT ACC</i>
Handle site helix0, #11-A	<i>ACAAATTCTTA</i> <i>AGAACGCGA TTC ACT ACT TAC CAC</i> <i>TCT ACC</i>
Handle site helix0, #13-A	<i>GTCAATAGATA</i> <i>ATACCTGAGCAA TTC ACT ACT TAC CAC</i> <i>TCT ACC</i>
Handle site helix0, #1-B	<i>AACTGTTGGAACCGTCCGGCAA</i> <i>TTC CTC TAC CAC</i> <i>CTA CAT CAC</i>
Handle site helix0, #3-B	<i>AGATACATTTCGATTGCCTGAGA</i> <i>TTC CTC TAC CAC CTA</i> <i>CAT CAC</i>
Handle site helix0, #5-B	<i>ACAGACCAGGCCAGAGGC</i> <i>TTTG TTC CTC TAC CAC CTA</i> <i>CTA CAT CAC</i>
Handle site helix0, #7-B	<i>GAGGGTTGATATGCTT</i> <i>CGAGGT TTC CTC CTC TAC CAC CTA</i> <i>CAT CAC</i>
Handle site helix0, #9-B	<i>CCCCAAAAGAAC</i> <i>TCCCCTATTATTC CTC CTC TAC CAC CTA</i> <i>CTA CAT CAC</i>
Handle site helix0, #11-B	<i>ACAAATTCTTA</i> <i>AGAACGCGA TTC CTC CTC TAC CAC CTA</i> <i>CTA CAT CAC</i>
Handle site helix0, #13-B	<i>GTCAATAGATA</i> <i>ATACCTGAGCAA TTC CTC CTC TAC CAC CTA</i> <i>CTA CAT CAC</i>
Handle site helix3, #14-C	<i>CAACAGTTGAAATAGTA</i> <i>AACA CTC CTA TCT CCA ATC</i> <i>ACT CCT</i>
Handle site helix4, #14-C	<i>AGAGATAGAACCTGCCGA</i> <i>ACGT CTC CTA TCT CCA</i> <i>ATC ACT CCT</i>
Handle site helix7, #14-C	<i>GAATACGTTGGCACAGACA</i> <i>ATATT CTC CTA TCT CCA</i> <i>ATC ACT CCT</i>
Handle site helix8, #14-C	<i>CATTTGGATTATACTT</i> <i>CTGAATA CTC CTA TCT CCA ATC</i> <i>ACT CCT</i>

Table A2.3 (continued).

Handle site helix11, #14-C	CCGACAGGAACGGTACGCC CTC CTA TCT CCA ATC ACT CCT
Handle site helix0, #1-A-PC	AACTGTTGGAACGTTCCGGCAA / PC / TTC ACT ACT TAC CACT CCT ACC
Handle site helix0, #3-A-PC	AGATACATTGATTGCCTGAGA / PC / TTC ACT ACT TAC CAC TCT ACC
Handle site helix0, #5-B-PC	ACAGACCAGGCAGAGGCCCTTG / PC / TTC CTC TAC CAC CTA CAT CAC
Handle site helix0, #7-B-PC	GAGGGTTGATATGCTTCGAGGT / PC / TTC CTC TAC CAC CTA CAT CAC
Handle site helix0, #9-B-PC	CCC AAA AGAACTCCCCCTTATTA / PC / TTC CTC TAC CAC CTA CAT CAC
Handle site helix0, #11-B-PC	ACAAATTCTTAAGAACCGCGA / PC / TTC CTC TAC CAC CTA CAT CAC
Handle site helix0, #13-B-PC	GTCAATAGATAATACTGAGCAA / PC / TTC CTC TAC CAC CTA CAT CAC
Handle site helix0, #11-D PAINT	AACTGTTGGAACGTTCCGGCAA TTATACATCTAG
Handle site helix0, #3-D PAINT	AGATACATTGCTGAGA TTATACATCTAG
Handle site helix0, #5-D PAINT	ACAGACCAGGCAGAGGCCCTTG TTATACATCTAG
Handle site helix0, #7-D PAINT	GAGGGTTGATATGCTTCGAGGT TTATACATCTAG
Handle site helix0, #9-D PAINT	CCC AAA AGAACTCCCCCTTATTA TTATACATCTAG
Handle site helix0, #11-D PAINT	ACAAATTCTTAAGAACCGCGA TTATACATCTAG
Handle site helix0, #13-D PAINT	GTCAATAGATAATACTGAGCAA TTATACATCTAG
Handle site helix7, #1-E-biotin PAINT	GTAAGCTTCAGAGGTGGAGCCG TTTTTT-biotin
Handle site helix4, #5-E-biotin PAINT	AAGGCTTGCCTCTCAAATGCTT TTTTTT-biotin
Handle site helix7, #9-E-biotin PAINT	AAAAAAATTCATATGGTTTACCAAG TTTTTT-biotin
Handle site helix4, #13-E-biotin PAINT	AGTAACATTATCCAATATATGTG TTTTTT-biotin

Table A2.4

Anti-handle oligonucleotide sequences.

Oligo	Sequence
A*	NH2-GGTAGAGTGGTAAGTAGTGAA
B*	NH2-GTGATGTTAGGTGGTAGAGGAA
C*-TAMRA	TAMRA-AGGAGTGGAGATAGGAG
C*-Cy5	CY5-AGGAAGTGATTGGAGATAGGAG
D*-Atto655	CTAGATGTAT-ATTO655

Table A2.5

Yeast strains used in this study. All strains were made in the W303a background (*MAT_a* *his3-11,15 ura3-1 leu2-3,12 ade2-1 trp-1*) with both the Pep4 and Prb1 proteases deleted. DHA and SNAP refer to the HaloTag (Promega) and SNAP_r-tag (NEB), respectively. TEV indicates a Tev protease cleavage site. *P_{GAL1}* denotes the galactose promoter, which was used to induce dynein expression. Amino acid spacers are indicated by *gs* (glycine-serine). GST-DYN_I*331kDa* as described (2).

Strain	Genotype	Use	Source
RPY1084	<i>P_{GAL1}-ZZ-TEV-GFP-3XHA-fSNAP_{gs}-GST-DYN_I_{331kDa}-gsDHA-Kan^R</i>	Model dimeric dynein	This study
RPY1165	<i>P_{GAL1}-ZZ-TEV-GFP-3XHA-fSNAP_{gs}-GST-DYN_I_{K1802A}_{331kDa}-gsDHA-Kan^R</i>	Inactive dynein (d ^I)	This study
RPY1235	<i>P_{GAL1}-ZZ-TEV-GFP-3XHA-GST-DYN_I_{E3197K}_{331kDa}-gsDHA-Kan^R</i>	Polarity marker	3
RPY1292	<i>P_{GAL1}-ZZ-TEV-GFP-3XHA-fSNAP_{gs}-GST-DYN_I_{E3197K}_{331kDa}-gsDHA-Kan^R</i>	dynein	This study

Table A2.6

Specifications for all chassis used in this study.

Chassis	D:K ratio	Fig	Dynein sequence	Kinesin sequence	Dynein site #s	Kinesin site #s	
1D and 1K	N/A	2	A*	A*	1	1	
2D and 2K	N/A	2	A*	A*	1,13	1,13	
4D and 4K	N/A	1, 2	A*	A*	1,5,9,13	1,5,9,13	
7D and 7K	N/A	2	A*	A*	1,3,5,7,9,11,13	1,3,5,7,9,11,13	
2D	N/A	3	A*	N/A	1,3	N/A	
2d ^P	N/A	3	A*	N/A	1,3	N/A	
5K	N/A	3	N/A	B*	N/A	5,7,9,11,13	
1D:6K	0.17	3	A*	B*	1	3,5,7,9,11,13	
2D:5K	0.40	3	A*	B*	1,3	5,7,9,11,13	
1D:2K	0.50	3	A*	B*	1	11,13	
2D:3K	0.67	3	A*	B*	1,3	9,11,13	
3D:4K	0.75	3	A*	B*	1,3,5	7,9,11,13	
3D:2K	1.50	3	A*	B*	1,3,5	11,13	
2D:1K	2.00	3	A*	B*	1,3,	13	
5D:2K	2.50	3	A*	B*	1,3,5,7,9	11,13	
2d ^P :5K	0.40	3	A*	B*	1,3	5,7,9,11,13	
2D*.5K	0.40	4	A*	B*	1,3	5,7,9,11,13	
2D:5K*	0.40	4	A*	B*	1,3	5,7,9,11,13	
D:d^I Ratio		Mutant dynein sequence		Mutant dynein site #s		Mutant dynein site #s	
Chassis		Fig.		Dynein sequence		Dynein site #s	
3D:1d ^I	3	S7	B*	A*	9,11,13	1	
3D:2d ^I	1.5	S7	B*	A*	9,11,13	1,3	
6D:1d ^I	6	S7	B*	A*	3,4,7,9,11,13	1	

Scaffold sequence:

GGCGGGGTGGGTTACGGCAGCGTGACCGCTACACTGCCAGGCCCTAGGCC
CGCTCCTTCGCTTCTCCCTTCTCGCCACGGTCGCCCTCGACCC
CAAAAACCTGATTGGGTGATGGTCACTAGGGCCATGCCCTGATAGACGGTT
TTTCGCCCTTGACGTTGGAGTCCACGTTTAATAGTGGACTCTGTCCAACCTG
GAACAACACTCAACCTATCTGGCTATTCTTGATTATAAGGGATTGGCATT
TCGGAACCACCATCAAACAGGATTGCCCTGCTGGGCAAAACCGAGCGACT
TGCTGCACACTCTCAGGGCCAGGGTGAAGGGCAACTAGCTGTGCCGTCTCAC
TGGCCGATTCAITAATGCAGCTGGCACAGGTTCCGACTGGAAAGGGCGACT
GAGCGAACGCAAATTATGTGAGTTAGCTCACTATTGGCACCCCCAGGCTTACACT
TTATGCTTCCGGCTCGTATGTGTGGATTGTGAGGGATAACAATTTCACACAGG
AACAGCTATGACCATGATTACCGAATTGAGCTCGTACCGGTACCCGGATCCTCAACTGTG
AGGAGGCTCACGGACGGGAAGAACAGGCACGGTGCTGGCAGAAACCCCGGTATG
ACCGTGAACACGGCCGCCGCATTCTGGCCGACGACAGAGTGCACAGGCC
CACTGACACTGGCTCGTCTGATGCAGGGCACCGGACCGCTGGCTGGCAG
GTAACCCGGCATCTGATGCCGTTAACGATTGCTGAACACACAGGTGTAAGGGATGTT
TATGACGGCAAAGAAACCTTACCCATTACCGCCAGGGCAACAGTGACCCGGC
TCATACGCCAACCGCCGGGGATTGAGTGGGAAGCGCCTGCAATGACCCGGCT
GATGCTGGACACCTCCAGCGTAAGCTGGTGGGATGGCTGCTGCTGGCAGCG
TCCCGTGGCATCTGCGGTGCTGCTGACCAGCAGGACCCACCGACCGACGGTGC
AAGTCCGGCACGGTCCAGGTATGAGGATGGCTGCTGGCAGCGACGGAG
ACGAAAAAACGGACCGCGTTGCCGGAACGGCAATCAGCATGTTAACTTACCC
TCATCACTAAAGGCCGCTGTGGGCTTTTACGGGATTTTTATGTCGATGTA
CAACCGCCAACCTGCGGCAAATGAGCAGAAATTAAAGTGTACCCCTGTTCT
GGCTCTTTCCGTGAGAGCTATCCCTCACCAACGGAGAAAGTCTATCTCACCAA
ATTCCGGACTGGTAACATGGCGTGTACGTTGCCGATTGTTCCGGTGAGGTT
TCCGGTCCGGTGGCGTCCACCTCTGAAAGCTTGGCACTGGCGTCGTTACAAC
GTCGTGACTGGGAAACCGCTGGCGTTACCCAACTTACGCCCTGCACTCCCC
CTTTCGCCAGCTGGCGTAATAGCGAAGAGGCCGACCGATGCCCTCCAAACAGT
TCCGCAGCCTGGAATGGCGAATGGCGCTTGCCTGGTTCCGGCACAGAAGCGGTC
CGGAAGACTGGCTGGAGTGCATCTCTGAGGCCGATACTGTCGTCGTCCTCAA
ACTGGCAGATGCACTGGTACGATGCCCATCACACCAACGTGACCTATCCCATTAC
GGTCAATCCGGTTGTTCCCACGGAGAATCCGACGGGTGTACTCGCTCACATT
AATGTTGATGAAAGCTGGCTACAGGAAGGCCAGACGCCAATTATGCGAATTAA
CTATTGGTTAACAAATTGCTTACAACTTCCCTGTTGGGCTTGTGATGGCGTC
TAACGTTACAATTAAATTGCTTACAACTTCAACTTCAACTTCAACTTCAACTT
TATCAACCGGGTACATGATGCTAGTAGTTACGATTACCGTTCATCGATCTC
TTGTTGCTCCAGACTCTCAGGCAATGACCTGATGCCTTGTAGATCTCAAAAT

AGCTACCCCTCCGGCATTAAATTATCAGCTAGAACCGGTGAATATCATATTGATGGT
ATTGACTGTCTCCGGCCTTCTCACCCCTTGAATCTTACCTACACATACTCAGGC
ATTGCATTAAATATGAGGGTCTAAAATTCTTGCGTTGAATAAGGC
TTCTCCCGCAAAGTATTACAGGGTCATAATGTTGGTACAACCGATTAGCTTAT
GCTCTGAGGCTTATTGCTTAATTGCTAATTCTTGCGCTTGCGTGTATGATTATTGG
ATGTTAATGCTACTACTATTAGTAGAATTGATGCCACCTTCAAGCTCGGCCCAAT
GAAAATATAGCTAACACAGGTATTGACCATTGCGAATGTATCTAATGGTCAAACTAA
ATCTACTCGTCGAGAATTGGGAATCACTGTATATGGAATGAAACTTCCAGACAC
CGTACTTAGTGCATATTAAACATGACCTCTATCAAAGGCAATTAAAGGTACTCT
CTCTAAAGCCATCCGCAAAGAATGACCTCTATCAAAGGCAATTAAAGGTACTCT
AATCCTGACCTGGAGTTGGCTCCGGTCTGGTCAAGCTCGAATTCAAGCAATTAA
CGCGATATTGAAGTCTGGCTCCGGTCTGGTCAAGCTCGAAGCTCGAATTAA
CTGACTATAATAGTCAGGGTAAGACCTGATTGATTCGTCATTCTCGTTCTG
AACTGTTAACGATTGAGGGGATCAATGAATATTGACGATTCCGCAGTATTG
GACGCTATCCAGTCTAACATTTACTATTACCCCTCTGGCAAACACTCTTGC
AGCCTCTCGCTATTGGTTTATCGTCTGGTAACAGGAGGTATGATAGTGTG
CTCTTACTATGCCTCGTAATTCCCTTGGCGTTAATGATTCGCAATTAGTGAATGTGGT
TCCTCTAAATCTCAACTGATGAATTCTTACCTGTAATAATGTTCCGGTTAGTTCGTT
TTATAACGTTAGATTCTTCCCACCGCTGACTGGTATAATGAGCCAGTTCTAA
ATCGCATAAGGTAATTACAATGATTAAGTGAATTAAACCATCTCAAGCCCAATT
AACTACTCGTTGGTCTCGTCAGGGCAAGCCTTACTGAATGAGCAGCATT
GTTACGTTGATTGGGTAATGAATAATCCGGTCTGTCAAGATTACTCTGATGAGG
CAGCCAGCCTATGCCCTGGTCTGTACACCGTTCACTGTCCTCTCAAGTTGGC
AGTTCGGTTCCCTTATGATTGACCGCTGGCTCGTCCGGCTAAGTACATGGAGC
AGGTCGGGATTTCGACACAATTATCAGGGATGATAACAATCTCCGGTGTACTTGT
TTCGGGCTTGGTATAATCGCTGGGTCAAAGATGAGTGTATTGTTAGTGTATTCTTGG
TCTTCGTTAGGTGGTGCCTCGTAGTGGCATTACGTTTACCCGTTAATGGA
AACTTCCTCATGAAAAGTCTTAGTCCTCAAGCCTCTGTAGCCGTGCTACCCCTG
TTCGGATGCTGTTGCTGAGGGTGACGATCCGGAAAAGGGCTTAACTC
CCTGCAAGCCTCAGCGACCGAATATATCGGTTATGCGTGGCGATGGTTGTGTCATT
GTCGGGCCAACTATCGGTATCAAGCTGTTAAGAAATTCACCTCGAAAGCAAGCTGAT
AAACCGATAACAATTAAAGGCTCCTTGGAGCCTTTGGAGATTCAACAGTGA
AAAAATTATTTCGCAATTCCCTTAGTTGTCCTTCTACTCCGCTGAAACTG
TTGAAAGTTAGCAAAATCCCATACAGAAATTCAACGCTCTGGAAAGA
CGACAAAACCTTAGTCGTAACATGAGGGCTGTCGTGGAATGCTACAGGC
GTTGTTAGTTGACTGGTGACGAAACTCAGTGTACGGTACATGGTTCTTCA
TTGCTATCCCTGAAAATGAGGGCTGGCTCTGAGGGTGGCGGTTCTGAGGGGG
GTTCTGAGGGTGGCGGACTAAACCTCCTGAGTACGGTACACCTATCCGGCTA
TACTTATCAACCCCTCGACCGCACTATCCGCTGGTACTGGCAGGCAAACCCCGCT
AATCCTAATCCTCTGAGGGAGTCTGAGGACTCTTAATACTTCACTGTTCA
TAGGTICCGAAATAGGCAGGGGCATAACTGTTATACGGGCACTGTTACTCAAGGC
ACTGACCCCGTTAAACTTACCACTGAGACTGCGCTTCCATTCTGCTTAATGAGGAT
CGCTTACTGGAACGGTAATTCAAGAGACTGCGCTTCCATTCTGCTTAATGAGGAT

TATTGTTGTGAATATCAAGCCAATCGTCTGACCTGCCAACCTCCGTCAATGC
TGGGGGGCTCTGGTGGTCTGGGGCTCTGAGGGTGGTCTGGGGCTCTGAGGG
CGGTGATTGAAAGATGGCAAACGCTAATAAGGGCTATGACCGAAAT
GCCGATGAAACGCGCTACAGTCTGACGCTAACGGCAACTGATTCTCGCTACT
GATTACGGTGTGCTATCGATGGTTCATGGTACGTTCCGGCCTGCTAATGGTAA
TGGTGCCTACTGGTGAATTGCTGGCTCTAATTCCAATGGCTCAAGTCGGTACCGT
GATAATTACCTTAATGAATAATTCCGTCATATTACCTCCCTCCCTCAATCGGTT
GAATGTCGCCCTTGCTTGGCTTAACAGCTGGTAATAAGGAGTCTTATGTA
TGTATTCTACGTTGCTAACATACTGCGTAATAAGGAGTCTTATGCTTATGTA
TGGGTATTCCGTTATTGGCTTCCGTTGGTACTTCTGGTAACTTGTGGTATCTCT
CTGCTTACTTTCTAAAGGCTCGTAAGATAGCTATTGCTATTCTCATGGTCTT
GCTCTTATTGGTAACTCAATTCTGTGTTAGCGCTGCTATTGACGTTAACAAAAT
TTTATGTTACTCTCTGTAAGGCTGCTATTGACGTTAACAAAAT
CGTTCTTAAAGGCTCGTAAGATAGCTATTGCTTAAAGGCTTGTAACTGGCAAAATT
GCTCTGGAAAGACGCTGTTAGCGCTGTAAGGATTGAGATAAAACGGCTGCTTCG
GCAAATAGCAACTAATCTGATTAAAGGCTCAAACCTCCGCAAGTCGGAGGT
TCGCTAAACGCTCGCGTTAGAATACCGGTTCTAGAATACCGGATAAGCCTGCTT
GCTATTGGCGGTAATGATTCTACGGATAAAACGGCTGCTGGTCTCG
ATGAGTGGGGTACTTGGTTAACACCGGTTCTGGAATGATAAGGAAGACAGCCGAT
TATGATTGGTTCTACAGCTGTAATTAGGATGGATAATTGCTTCTGAGGA
CTTATCTATTGTTGATAAACAGGGCGTCTGCATTAGCTGAACATGTTATGTC
GTCGTCGGACAGAATTACTTACCTTGTCGGTACTTATATTCTCTTATTACTGGCT
CGAAATGGCTCTGCTTAATTACATGTTGGCTTAAATATGGGATTCTCAATT
AGCCCTACTGTTGAGCGTTACTGGTAAGAATTGTTATAACGCATATGATAC
TAACAGGGTTCTAGTAATTATGATTCCGGTTATTCTTAAACGCCTTATT
TCACACGGTCGGTATTCAACCTAACCTAAATTAGGTCAAGAAGATGAAATTAA
TATATTGAAAAGTTCTCGGGTTCTGCTGGATTGCTACAGCATTAA
CATATAGTTAACCCAACCTAACGGGAGGTAAAGGTTAGTCTCAGACCTAT
GATTGATAATTCAACTATTGACTCTTCAGCGCTTAATCTAGCTATCGCTATGTT
TTCAGGATTCTAAGGGAAATTAAATTAGCGACGATTACAGAAGCAAGGTTATT
CACTCACATATTGATTATGACTGTTCCATTAAAAGGTTAGTCTCAGACCTAT
TTAATGTAATTCAATTGTTCTGATGTTCTGCTGGATTGCTACAGCATTAA
ATTGAATGAAATAATTGTTCTGCTGGATTGCTACAGGTTAGTCTCAGGTT
CGAATCCGGTATTGTTCTCCGATTACAGGTTAGTCTCAGGTT
TAACACCTGAAATTCTACGCAATTCTTACGTTACGTCATTGCTCAAGGTT
ATTGAATGAAATTCTACGCAATTCTTACGTTACGTCATTGCTCAAGGTT
GGTAGGTCTAACCCCTCCATTACAGGTTAGTCTCAGGTT
ATGAATTGCCATCTGATAATTGTTAGTCTCAGGTTAGTCTCAGGTT
TCTTGTCTCGCAAATGATAATTGTTACTCAAACTTTAAATAACGTCGGGCA
AAGGATTAATACGAGTTGTCGAATTGTTGTAAGTCTAATAACGTCGGGCA
TGTATTATCTATTGACGGCTTAACCTATTAGTGTAGTCTCCTAAAGATTTAGAT

AACCTTCTCAATTCCCTCAACTGTGATTGCCAAGTGCAGGATTTGAGGG
TTGATATTGAGGTTCAGCAAGGTGATGCTTAGATTTCATTGCTGCTGGCTCTC
AGCGTGGCACTGTCAGGCCGGTTAACTGACCCCTCACCTCTGTTATCTC
TGCTGGTGTGTCGGTATTTTAATGGCGATGTTAGGCTATCAGTTCGCGCAT
TAAGACTAATGCCATTCAAAAATATGTCGTGCCACGTTACGCTTCAGGT
CAGAAGGGTTCTATCTCTGTTGCCAGAATGTCCTTTTATTACTGGTGTGACTG
GTGAATCTGCCAATGTAATAATCCATTCAAGACGATTGAGCGTCAAATGTTAGGATT
TCCATGAGCGTTTCCTGTGCAATGGCTGGCGTAATTGTCGTGGATATTACAG
CAAGGCCGATAGTTGAGTTCTACTCAGGCCAAGTGTATTACTAATCAAAGA
AGTATTGCTACAACGGTTAACCGTGTGGACAGACTCTTACTCGGTGGCCTCA
CTGATTATAAAACACTTCTCAGGATTCTGGCGTACCGTTCTGCTAAATCCCTTA
ATGGCCCTCCTGTTAGCTCCCTGATTCTAACGAGGAAGCACGGTATACTGTC
TCGTCAAAGCAACCATACTACGCCCTGTAGGGCGCA

References

1. S. M. Douglas *et al.*, Rapid prototyping of 3D DNA-origami shapes with caDNAno, *Nucleic Acids Research* **37**, 5001–5006 (2009).
2. S. L. Reck-Peterson *et al.*, Single-Molecule Analysis of Dynein Processivity and Stepping Behavior, *Cell* **126**, 335–348 (2006).
3. W. B. Redwine *et al.*, Structural basis for microtubule binding and release by dynein, *Science (New York, N.Y.)* **337**, 1532–1536 (2012).